EFFECTS OF SURFACE AND CHEMICAL COMPOSITION ON THE CHARGE CARRIERS OF ALLOYED QUANTUM DOTS

By

Joseph Daniel Keene

Dissertation

Submitted to the Faculty of the
Graduate School of Vanderbilt University
in partial fulfillment of the requirements
for the degree of
DOCTOR OF PHILOSOPHY
in
Chemistry

May, 2015

Nashville, TN

Approved:

Sandra J. Rosenthal, Ph.D.

David E. Cliffel, Ph.D.

John A. McLean, Ph.D.

Richard F. Haglund, Ph.D.

Dedicated to

my wife, Ashley Golden Keene

and

my daughter, Hope Mackenzie Keene

ACKNOWLEDGEMENTS

I would like to acknowledge and thank the many people whose help and support made this work possible. To my advisor, Dr. Sandra J. Rosenthal, thank you for taking me into your group as a spectroscopist and for letting me scratch my synthetic itch, so to speak, upstairs in the wet lab whenever I needed to get out of the dark. Thank you for the freedom to pursue my own interests and learn from my mistakes. Your mentorship has allowed me to mature as a scientist and, importantly, as a person. Thank you for the opportunity to study under your mentorship.

Drs. David E. Cliffel, John A. McLean, and Richard F. Haglund: your service on my Ph.D. committee is much appreciated. Your thoughtful suggestions bettered me as a scientist and improved the quality of this work.

Thank you Dr. James R. McBride for all of the advice, ideas, skepticism, and guidance in the lab. Importantly, thank you for all of your time and effort you spent at the electron microscope on my behalf, and for the many hours of HR-TEM, EDS, STEM, and STEM-EDS imaging that strengthened my work and enhanced its relevance. You helped me learn which questions to ask, and how to take an idea and develop it into a feasible and scientifically relevant project.

I would be remiss without acknowledging Mr. Elton Caviness for introducing me to the world of chemistry. Your enthusiasm for the subject was contagious and was my first step on the path that has led me here. Dr. Bradley T. Jones, thank you for my first opportunity to conduct chemistry research and for making it a pleasurable experience that left me seeking more.

Dr. Albert D. Dukes, III, thank you for the introduction to nanocrystals, our laser, and ultrafast spectroscopy. Your training on the ultrafast laser system was invaluable. You helped me learn the importance of a good set of troubleshooting skills and of always keeping a trick up my sleeve. Your non-stop wit ensured there was never a dull moment in the first months I spent learning in the lab. Dr. Melissa A. Harrison, your development of the graded alloy CdSSe nanocrystal synthesis piqued my interest and provided me with an intriguing question to pursue, which ended up being the main thrust of this dissertation.

Noah J. Orfield, many hours have we spent together in the laser lab. Our almost-daily sessions of bouncing ideas off each other about our work helped me tremendously. J. Scott Niezgoda, thanks for the many ideas and insights into my work you provided as we shared our desk space. Also, thank you for allowing me to contribute to your own $Cu_xIn_yS_2$ project; I enjoyed the challenge. To Kemar Reid and Nathaniel Freymeyer, good luck with your studies in the laser lab; I hope you find them as fulfilling as I have. To the many other Rosenthal lab members past and present, I cannot thank you enough for your support and the many baked goods you provided over these past years. To thank you all individually for your many contributions would increase my printing costs beyond my budget. You know who you are; know that you have my thanks.

Dr. Donald Stec, your help with the NMR instrumentation was vital to my research. Many of our efforts didn’t quite provide the right data to make it into this dissertation, but I learned a lot and always know who to turn to if ever I lose my way and need to find my protons.

Drs. S. Michael Kilbey, II, Deanna L. Pickel, and W. Michael Kochemba: I enjoyed our collaboration. Thank you for your synthetic expertise and for providing me with the various functionalized P3HT polymers with which to experiment.

I want to acknowledge Vanderbilt University and the National Science Foundation (CHE-1213758 and EPS-1004083) for financial support during my tenure as a graduate student. Without said funding none of this would have been possible.

To my family, especially my parents Jimmy and Pam Keene, thank you for supporting me as I pursued my dreams. You made me who I am today. Know that wherever life may take me, I will never forget where I came from.

Ashley, my wife, you are the most amazing, supportive, strong, intelligent, and beautiful woman I know. I am eternally grateful to have you by my side. Thank you for your unwavering love, support and understanding these last 6 years together. There are not enough words to express my gratitude for all that you do for me day in and day out. You are my rock. I love you.

To my brand new daughter Hope, your impending arrival was a unique and urgent motivation to keep me on a timeline and finish this dissertation. All save this portion of this dissertation was written as your mother and I eagerly anticipated your arrival, and these final thoughts I leave with you are the only words that were written after you miraculously entered our lives: I cannot express how wonderful, beautiful, amazing, and perfect you are. I am so proud to be your father. My hopes and dreams for you are without borders. In all your days, above all else, remember these things: love God, love your family, and relentlessly pursue your dreams, wherever they may take you in life. Your mother and I love you beyond measure. I pray that you find joy and happiness to equal that which you have brought us in these few short days since your arrival.

TABLE OF CONTENTS

Page

Chapter

LIST OF FIGURES

Figure Page

CHAPTER I

INTRODUCTION

1.1 Semiconductor Nanocrystals

Ever since the seminal work by L. Brus in 1984 in which the concept of quantum confinement in nanostructured semiconductor materials was first introduced,[1] the scientific community has been fascinated with the unique properties that arise from materials with dimensions at the nanoscale. These many foundational studies have revealed a plethora of information about the fundamental behavior of semiconductor nanocrystals, particularly with regards to the behavior of the excited state. Methods have since been developed by which we can exhibit control over the excited state of nanocrystals and even now much effort is devoted to specifically engineer their structure to yield desired properties. Given these successes, nanocrystals have been implemented in a wide array of applications. Many of the applications in which they have been utilized are geared towards sources of alternative energy, such as photovoltaics and solar concentrators, or enhancing efficiencies in existing technologies, such as light emitting diodes and solid state lighting. Semiconductor nanocrystals are not just being studied for their own end as a product, but they are also being utilized as a tool in other fields. In fact, they have found particular success in areas of biomedical research as fluorescent biological probes for drug screening displacement assays and are uniquely suited for single-particle tracking. There are many advantages to using quantum dots over the oft-utilized organic dyes or phosphors that are typically employed in all of the aforementioned applications: they are inorganic particles which makes them more structurally robust and less amenable to photobleaching, they are very strong absorbers of light due to remarkably large extinction coefficients, and they have tunable optical and electronic properties arising from quantum confinement.

1.1.1 Quantum Confinement

The unique size-dependent optical and electronic properties of nanocrystals are a direct result of quantum confinement. Before a clear explanation of quantum confinement can be understood, however, it is important to first understand the excited state in bulk semiconductor materials. The band gap (E_g) of a bulk semiconductor material is defined as the energy necessary to create an electron and a hole at rest with respect to the lattice and far enough apart such that their Coulomb attraction is negligible.[1] In this case, the electron and hole are known as free charge carriers and have no interaction with one another. However, in a special case an exciton may form. An exciton, or a bound electron-hole pair in bulk semiconductor material, is described as a neutral excitation particle bound by the electron-hole Coulomb interaction, with the distance between the electron and hole known as the Bohr exciton radius (a_B).[2] The energy of the exciton configuration (E_x) is actually slightly below the band gap, being lowered by the exciton binding energy (E_b), which is the magnitude of the attraction between the electron and hole. This is illustrated in Figure 1.1.

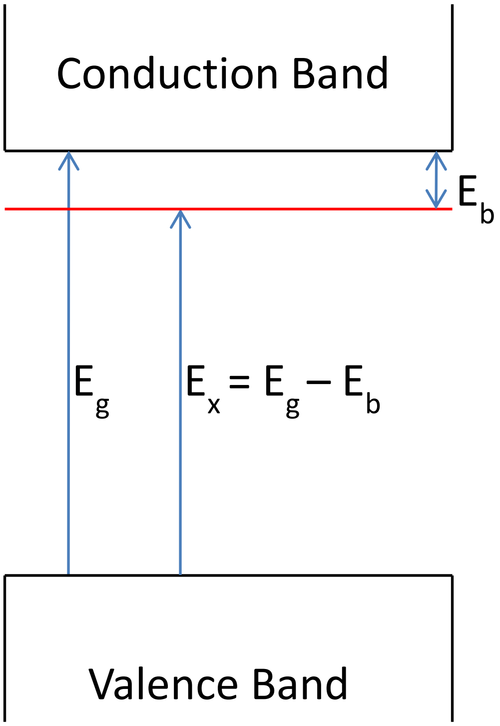

Figure 1.1. Conduction band and valence band are separated by band gap energy (E_g) in bulk semiconductor material. The exciton energy (E_x) is lower than the band gap by the binding energy (E_b) of the electron and hole.[2]

In nanocrystals, however, when the diameter of the crystal is on the order of or smaller than the Bohr exciton diameter, the electron and hole cannot achieve the equilibrium separation distance. In this case, the exciton is dictated not by the electron-hole Coulomb interaction, but by the physical dimensions of the material.[2] When the electron and hole cannot achieve their desired separation distance as defined by the bulk Bohr exciton radius, their wavefunctions are forced to overlap. This is energetically unfavorable and more energy must be added into the system in order to stabilize this interaction. This becomes more pronounced for smaller nanocrystals as the electron and hole wavefunctions are forced to overlap more strongly, thus requiring more energy to stabilize the system. Herein lies the observed blue-shift in the band gap (E_g) as nanocrystal size decreases, and as a result the band gap can be tuned according to nanocrystal size.[3]

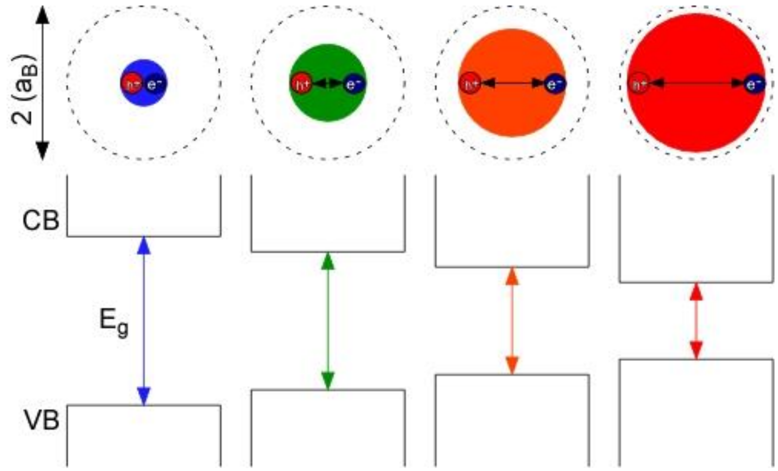

Figure 1.2. Illustration of quantum confinement in semiconductor nanocrystals. As the size of the nanocrystal decreases, the charge carriers are forced to overlap more strongly which increases the band gap energy.

Quantum confinement in semiconductor nanocrystals is a real-world example of the infamous particle-in-a-box, in which the difference between energy levels is inversely related to the square of the radius of the nanocrystal. This shift of the lowest excited state with respect to the bulk band gap (E_{ex}) was modeled by L. Brus for semiconductor nanocrystals according to:[1]

$$E_{ex} = \frac{\hbar^2\pi^2}{2R^2}\left(\frac{1}{m_e}+\frac{1}{m_h}\right) - \frac{1.8e^2}{\varepsilon_2 R} + \frac{e^2}{R}\overline{\sum_{n=1}^{\infty}\alpha_n\left(\frac{S}{R}\right)^{2n}} \qquad (1.1)$$

in which $\hbar$ is the reduced Planck's constant, R is the nanocrystal radius, m_e and m_h are the effective masses of the electron and hole, respectively, e is the absolute charge of an electron, ε_2 is the dielectric constant of the semiconductor material, α_k is a constant that relates the dielectric constants of the semiconductor material and the surrounding medium,[1] and S is the wavefunction that describes the position of the electron and hole in the *1S* exciton. The first term in equation 1.1 defines the quantum energy of localization, the second term is the Coulombic attraction of the oppositely charged carriers, and the third term is the solvation energy loss the charge carriers experience in the dielectric medium. As the size of the nanocrystal decreases, the first term dominates and the increase in band gap becomes more exaggerated.

Figure 1.3. CdSe nanocrystals fluorescing under UV excitation ranging in sizes from ultrasmall <2 nm (left) up to 7 nm (right), illustrating the size-dependent effects of quantum confinement.

1.1.2 Importance of Nanocrystal Surface on Charge Carrier Behavior

Due to the extremely small size of nanocrystals, they are made up of only tens to thousands of total atoms and therefore have inherently large surface-to-volume ratios. In fact, for CdSe nanocrystals with 8.5 nm diameter, 20% of the atoms that make up the crystal are actually located on the surface of the nanocrystal. This percentage of total atoms that are the surface atoms increases to 88% as the diameter decreases to 1.2 nm.[4] These large surface-to-volume ratios coupled with the strong geometric confinement of the exciton in nanocrystals lead to significant interaction of excited charge carriers with the surface. Ultrasmall CdSe nanocrystals with diameters <2 nm were discovered in 2005 to be completely dominated by surface-state emission and thus, instead of the size-tunable colored emission, emit the full white-light spectrum at the single-nanoparticle level.[5-7] As later described in detail in section 1.2.1, these surface interactions typically occur within the first ten picoseconds after excitation and play a pivotal role in determining the ultimate fate of the excited state. Many different methods of surface modification, such as choice of organic ligands or other semiconductor capping materials, have been shown to influence the behavior of the excited state.[8-11] Traditionally, the nanocrystal surface has been envisioned as a faceted crystalline interface that, as it relates to the relaxation mechanisms of the exciton, contains an ensemble of trap states that can localize excited charge carriers and provide relaxation pathways for non-radiative recombination, thereby reducing the efficiencies with which nanocrystals fluoresce. In this sense, much of the work to enhance the radiative recombination and suppress non-radiative recombination pathways in order to increase the fluorescence from semiconductor nanocrystals has been focused on finding different means to passivate the surface and eliminate the surface charge carrier trap state sites.

Recent work performed by Pennycook *et al.*, however, challenges this notion of a static crystalline surface in nanocrystal structures.[12] Aberration-corrected atomic number contrast scanning transmission electron microscopy (Z-STEM) videos of CdSe nanocrystals of varying sizes, ranging from ultrasmall <2 nm up to 7 nm, showed surface atoms in a state of flux under the electron beam. Density functional theory simulations supported that, at least for the smaller nanocrystals, the energy imparted by the electron beam under the experimental conditions was similar to absorption of an ultraviolet photon by the nanocrystal structure. This work was the first direct evidence of a fluxional nanocrystal surface wherein, instead of a static crystalline surface, the atoms within ~1 nm of the surface are actually physically in motion whenever the nanocrystal is under excitation. McBride *et al.* later expounded on this idea and many of the potential implications this poses to the various fields that involve nanocrystalline structures.[13] As it relates to the excited state of the nanocrystal, a potentially fluxional nanocrystal surface implies that the trap states that traditionally are thought of as unpassivated atoms on the surface of the nanocrystal may actually extend down in to the nanocrystal structure ~1 nm from the surface, as the fluxional atoms at any given point in time can be under-coordinated and act as a charge carrier trap site. The main implication this poses for charge carrier trapping is that, in order to inhibit the charge carrier trapping that leads to non-radiative relaxation pathways, instead of simply passivating the nanocrystal surface, one must either strengthen and stabilize the surface atoms to prevent their movement or manipulate the nanocrystal in such a way as to prevent charge carriers from overlapping the surface or near-surface region of flux of the nanocrystal altogether.

1.2 Ultrafast Spectroscopy

Ultrafast spectroscopy techniques monitor the behavior of excited charge carriers on the femtosecond and picosecond time scales. In this time frame in semiconductor nanocrystals, the charge carriers are first excited and begin to interact with the surface of the nanocrystals. As discussed in depth above in section 1.1.2, the surface of the nanocrystal plays an integral role in the excited state of the charge carriers; therefore, the kinetics of the surface interaction of the charge carriers yield a rich bounty of information on how different surface treatments affect the nanocrystal surface. Modifying the surface of the nanocrystal can result in differing structural or stoichiometric defects, vacancies, dangling bonds, and impurities, all of which contribute to the availability of radiative and non-radiative relaxation pathways for the excited charge carriers.

The presence and distribution of competing relaxation pathways will have a profound impact on the relaxation dynamics of the excited charge carriers; therefore, ultrafast spectroscopy is an ideal technique to investigate the surface chemistry of semiconductor nanocrystals.

1.2.1 The History of Ultrafast Spectroscopy and CdSe Nanocrystals

Many studies on the ultrafast carrier dynamics of CdSe nanocrystals have been reported in the literature and have employed various time-resolved spectroscopic techniques including transient absorption, fluorescence upconversion, photon echo, and transient grating spectroscopies, among others. These foundational studies performed by the likes of C. Burda, M. El-Sayed, V. Klimov, P. Guyot-Sionnest, M. Bawendi, S. Rosenthal, and many others demonstrated that the size and surface chemistry of semiconductor nanocrystals strongly influence the relaxation dynamics of the electron-hole pair.[6,8-11,14-17] A generalized picture of the surface trapping and relaxation decay pathways is as follows, as presented by Underwood *et al.*[11] Typically, the surfaces of CdSe nanocrystals are on average comprised of 30% selenium atoms with the remaining 70% comprised of cadmium atoms that are passivated by a coordinating ligand.[18] The bare selenium atoms on the surface of the nanocrystal are in the form of dangling selenide bonds, which are calculated to be mid-gap states.[19,20] In the example of Underwood *et al.*, the CdSe nanocrystals were synthesized with tri-n-octylphosphonic oxide (TOPO) as the coordinating solvent to passivate the cadmium atoms.[11] Nanocrystals synthesized with this solvent system exhibited two radiative decay pathways; radiative emission was observed for band edge recombination and also for the mid-gap deep-trap state found at the nanocrystal surface. Each pathway was probed separately *via* ultrafast fluorescence upconversion and it was found that each relaxation pathway consists of two decay processes, a short-lived (τ_1) component and a long-lived (τ_2) component. The short-lived component for band edge recombination, realized experimentally as a depletion of the radiative recombination, was attributed to selenium dangling bond electrons annihilating the hole left in the valence band upon photo-excitation of the nanocrystal. The short-lived decay was found to be ~2-6 ps, varying with nanocrystal size. Smaller nanocrystals have enhanced electron-hole wavefunction overlap with the surface of the nanocrystal and thus the surface trap states are more rapidly populated. As a result, smaller nanocrystals have a shorter τ_1 as this corresponds to more rapid depopulation of the band edge radiative state. The long-lived component of the band edge emission is due to the "dark exciton" effect, wherein the excited electrons relax from the singlet excited state to a triplet excited state.[3,21,22] Subsequent triplet state relaxation is an optically forbidden transition on the order of a few nanoseconds and therefore its decay constant is beyond the experimental capabilities of the mechanical delay stage utilized in the fluorescence upconversion experimental setup.[3] Also, it could not be resolved separately from the singlet state in the experiment since it is very close in energy to the singlet state, only ~12 meV lower in energy.[3]

The deep trap emission was also observed experimentally and was found to have short- and long-lived components. The short-lived component was attributed to immediate relaxation of a surface selenium dangling bond electron to the valence band where it radiatively recombines with the initial photo-generated hole. It presents itself as a rise time of ~2 ps, indicating the deep-trap state takes time to become populated. This population of the trap state directly correlated to the depopulation of the band edge radiative state, meaning these two processes are coupled. The long-lived time component of the deep trap emission results from the primary photo-generated electron combining with a surface hole, or *vice versa*. The long-lived time component is once again a product of the 'dark exciton' triplet state relaxation.

Other foundational ultrafast charge carrier dynamics studies on CdSe nanocrystals that utilized fluorescence upconversion spectroscopy highlighted the importance of surface ligands and inorganic capping materials. Kippeny *et al.* and Garrett *et al.* investigated the effects of different synthetic precursors, co-coordinating solvents, and shelling with different inorganic semiconductor materials.[8,10] Hexadecylamine (HDA) was incorporated into the synthesis of CdSe nanocrystals because it resulted in narrowed size distribution and reduced the number of shape abnormalities; additionally, it was observed that the broad deep trap emission disappeared and only band edge recombination was observed radiatively with addition of HDA.[8,10,23] Addition of HDA also increased the short-lived time component of the band edge emission as a result of the interaction of the alpha hydrogen atoms on the carbon chain of HDA with the dangling selenium bonds on the surface which reduced the number of trap sites available.[8,10] Upon addition of a consistent shell thickness of 4-5 monolayers of ZnSe on differing sizes of CdSe cores, it was found that larger nanocrystal cores exhibited an increase in hole trapping efficiency.[10] This is due to the band gap alignment of the core and shell materials in which the electron becomes confined to the core due to conduction band offset while the hole may occupy either the core or the shell material due to alignment of the valence band for larger core diameters. This enhanced charge separation inhibited radiative recombination and resulted in increased hole trapping efficiency.[10]

Subsequent studies have provided complimentary verification of these interpretations and have yielded alternative explanations that challenge or extend this relaxation scheme in which a vast heterogeneity of the relaxation dynamics in the field was apparent. Weiss and coworkers have utilized transient absorption spectroscopy in the near-infrared to probe the non-radiative electron and hole relaxations separately, in addition to the band edge relaxation observed in the visible and long-time photoluminescence spectroscopy.[24] Global analysis of their data required six exponentials. Their interpretation of the results presented a model for carrier relaxation in CdSe nanocrystals that consisted of three different sub-populations of excited nanocrystals in which each had a distinct kinetic scheme with four rate constants resulting from four states. Marcus and Scholes have presented an alternative explanation for exciton decay in attempting to describe temperature-dependent charge carrier trapping in core/shell semiconductor nanocrystals as a Marcus Electron Transfer (ET) process.[25,26] Utilizing this approach in their analyses, they were able to calculate the number of trap state distributions, the depth of the traps, as well as the size distribution of the trap states present in the nanocrystals. Kern *et al.* utilized multiple population-period transient spectroscopy, termed MUPPETS, to study the carrier dynamics of CdSe nanocrystals and argued that the multi-exponential decays often reported for the relaxation dynamics of semiconductor nanocrystals is a result of sample heterogeneity, and at the single-nanoparticle level CdSe nanocrystals exhibit single-exponential decay.[27] Califano, Lian, Gómex-Campos, and coworkers have proposed a model of Auger-assisted transfer as the single mechanism responsible for carrier trapping and argued that it provides a more complete and accurate representation of carrier trapping than Marcus ET based explanantions.[28,29]

As is apparent from these various reports in the literature, the field of carrier dynamics in semiconductor nanocrystal structures has significantly advanced with the numerous contributions over the last few decades. However, there remains an ongoing attempt to develop a complete and universal understanding of excited charge carrier behavior in semiconductor nanocrystals. One can hypothesize that the great variability from study to study is rooted in the sensitivity of the excited charge carriers to the surface of the nanocrystal, which was highlighted in section 1.1.2 and will be further explored in this dissertation.

1.2.2 The History of Ultrafast Spectroscopy and CdS_xSe_{1-x} Nanocrystals

Early ultrafast spectroscopy reports in the literature on alloyed CdS_xSe_{1-x} samples were performed on bulk samples by Gadd and Hane.[30-32] It was found that bulk lifetimes in homogeneous samples were dependent on composition with lifetimes on the order of several hundred ps. Graded alloys, interestingly, were found to not only have composition-dependent dynamics, but even within a single sample there was a strong dependence of lifetime on emission wavelength. For CdSe-based samples alloyed with sulfur, longer lifetimes were found for longer wavelengths in the range of 500-620nm emission whereas shorter lifetimes were found for longer wavelengths in the range of 620-720nm. Opposite trends were found for CdS-based samples alloyed with selenium.

The extent to which CdS_xSe_{1-x} alloy nanocrystals has been studied has mainly been limited to homogeneous alloys either embedded within a glass matrix until more recent studies on a colloidal suspension. Zhang *et al.* found that CdS_xSe_{1-x} nanocrystal doped glasses had a decreasing decay time constant with an increase in pump power, which was attributed to Auger recombination and exciton-exciton annihilation.[33] Additionally, excited carriers have been found to have a 2 ps relaxation into a dangling bond state for CdS_xSe_{1-x} nanocrystal doped glasses.[34] In another study by Shen *et al.*, three decay time constants were required to fit the ultrafast charge carrier dynamics data, corresponding to direct recombination, excited state trapping, and trapping processes at the nanocrystal-glass interface.[35] The results were also size dependent with increased radiative decay rates for decreased nanocrystal sizes. Additionally, Toyoda and Shen found that $CdS_{0.26}Se_{0.74}$ nanocrystals in glass exhibited three exponential decay processes attributed to direct recombination with possible trapping, radiative recombination, and non-radiative recombination processes.[36]

Garrett *et al.* studied homogeneously alloyed CdS_xSe_{1-x} nanocrystals as a colloidal solution and demonstrated that the nanocrystal composition had a strong influence on the charge carrier dynamics.[9] The ultrafast carrier dynamics of CdS_xSe_{1-x} alloys were compared to CdSe and CdS and it was found that increasing sulfur content yielded a reduction in the magnitude of band edge recombination (τ_1) and a decrease in the long-lived recombination (τ_2). This was attributed to the introduction of surface trap states by sulfur. As sulfur content and consequently the number of trap states increase they begin to dominate the decay processes and diminish radiative recombination.[9]

1.3 Overview

The aim of this dissertation is to detail the characterization of the surface chemistry of nanocrystals of different semiconductor materials, demonstrate the importance of surface chemistry on the behavior of charge carriers in semiconductor nanocrystals, and provide an example in which the surface overlap of the excited hole in graded alloy semiconductor nanocrystals was eliminated. Chapter I provides an overview of semiconductor nanocrystals, highlights the importance of the surface in nanocrystalline structures, and details previous investigations of the charge carrier dynamics of cadmium chalcogenide and cadmium chalcogenide-based alloy nanocrystals to provide perspective and lay the foundation for this work. Chapter II details the experimental procedures utilized in the syntheses, post-synthetic surface modifications, and the many characterization techniques utilized in this dissertation. Chapter III demonstrates CdSe nanocrystal surface ligand modification with the semiconductor polymer poly(3-hexylthiophene) and characterization of the polymer ligation to the nanocrystals. Chapter IV continues the theme of characterization of nanocrystal surface chemistry with an investigation of the bound ligands of $Cu_xIn_yS_2$ nanocrystals to enable determination of the cause of the plasmonic modes that these nanocrystals possess is due to the stoichiometry of the nanocrystals and is not a product of the surface chemistry. Chapter V details the structural characterization and femtosecond fluorescence upconversion spectroscopy of graded alloy CdS_xSe_{1-x} nanocrystals and provides analysis of the ultrafast carrier dynamics. It was found that a heterogeneous chemical composition alters the band structure within the nanocrystals to prevent excited charge carrier overlap with the surface of the nanocrystals, in this case the excited hole. This elimination of the excited hole-surface overlap inhibited hole trapping at the surface and resulted in enhanced optical properties of the quantum dots. Chapter VI concludes the work presented in this dissertation and offers some perspective on potential future work inspired by the results and conclusions of these studies.

CHAPTER II

EXPERIMENTAL METHODS

2.1 Synthesis of CdSe and Graded Alloy CdS_xSe_{1-x} Nanocrystals

2.1.1 Synthesis Considerations

There are different approaches to synthesizing chemically inhomogeneous nanocrystal hetero-structures that have been successful in the literature. One method, known as successive ion layer adsorption and reaction (SILAR), involves multiple precursor injection steps wherein the core material is formed *via* nucleation and growth of the initial cation and anion species in the reaction vessel.[37] Then, the shell material is dictated by the delayed addition of shell precursors to the reaction mixture. A more recent approach involves prior synthesis of nanocrystal cores and post-synthetic modification of the chemical composition near the surface of the quantum dot *via* ion exchange.[38] These techniques, however, typically result in a hard interface between the core and shell materials. In order to investigate the effects of a graded interface between core and shell materials, the method that was the employed in this work is founded on differing precursor reactivities.[39] By choosing cation and anion precursors of varied reactivity, the more reactive species nucleates first and forms the nanocrystal core. The less reactive species is slower to incorporate into the nanocrystal structure and makes up the chemical composition of the shell material. This technique is a one-pot, single-injection colloidal synthesis and is attractive for many reasons including it eliminates the added complexity of multiple steps, reduces synthesis time, and minimizes the amount of solvents consumed and chemical waste generated, resulting in a more “green” synthesis.

The differing reactivity technique employed herein is based on work first presented by Swafford *et al.* and further explored by Harrison *et al.* in the synthesis of both homogeneous and heterogeneous alloyed cadmium sulfoselenide (CdS_xSe_{1-x}) nanocrystals.[39,40] It was found that sulfur bound by excess tributylphosphine (TBP) exhibited a different reactivity with cadmium than elemental (unbound) sulfur dissolved in 1-octadecene (ODE). The ratio of rates of addition of sulfur and selenium is proportional to the ratio of sulfur and selenium concentrations:

$$\frac{\frac{d[AS-S]}{dt}}{\frac{d[AS-Se]}{dt}} = \frac{k_1[AS][S]}{k_2[AS][Se]} = \frac{k_1[S]}{k_2[Se]} \qquad (2.1)$$

where *AS* is an available anion binding site and k_1 and k_2 are rate constants. When $k_1 \neq k_2$, as is the case when both sulfur and selenium are bound to excess TBP, the less reactive species (sulfur) is delayed in being incorporated into the nanocrystal structure. Additionally, different concentrations of sulfur and selenium were explored in this work, *i.e.* $[S] \neq [Se]$, further influencing the rate of addition of sulfur and selenium in the nanocrystal structure.

2.1.2 CdSe Oleic Acid Synthesis

Oleic acid ligated CdSe (OA-CdSe) nanocrystals were synthesized by a colloidal solvothermal high-temperature injection method. The reaction vessel was prepared by combining 10 mL of 0.2 M (2 mmol) Cd:oleate in 1-octadecene (ODE), 1.3 mmol of trioctylphosphine oxide (TOPO), 5.5 mmol of octadecylamine (ODA), and 5 mL ODE wherein the ODE served as the solvent. This mixture was heated to 280°C with stirring while purging with argon through a

12-gauge needle, which was removed at 150°C wherein water and oxygen were considered to be removed from the system. Once the solution was clear and colorless, 1 mL of 1.5 M (1.5 mmol) selenium:tributylphosphine (Se:TBP) was diluted to 6 mL with ODE followed by swift injection, after which the temperature was reduced to 260°C to grow for 1 hour. At 10 minute intervals, 2 mL each of 0.2 M (0.4 mmol) Cd:oleate and 0.2 M (0.4 mmol) Se:TBP were added to serve as growth solutions. Nanocrystal growth was monitored by UV-visible absorption spectroscopy of aliquots pulled from the reaction vessel. Once the desired size was achieved, the reaction vessel was cooled to 90°C with compressed air and the nanocrystals were isolated by precipitation with butanol/ethanol and centrifugation. The nanocrystals were further purified by dissolving in a minimum amount of toluene and then adding ethanol until flocculation, followed by precipitation *via* centrifugation; repeating as necessary. The purified nanocrystals were solvated in toluene.

2.1.3 Graded Alloy CdS_xSe_{1-x} Synthesis

Compositionally graded alloy CdS_xSe_{1-x} nanocrystals were synthesized according to the procedure developed by Harrison *et al.*[39] The anion precursor solutions were prepared by diluting 2 M X:TBP (X = S, Se) with ODE to 0.75 M X:TBP/ODE. To load the reaction vessel, 0.2576 g (2 mmol) CdO, 2.52 mL (4 mmol) oleic acid and 40 mL ODE were placed into a 250 mL 3-neck round bottom flask and heated to 220°C under UHP Ar. Once the reaction solution was clear and colorless, indicating that precursors CdO and oleic acid had converted to Cd-oleate, a mixed solution of 0.8x mL of 0.75 M Se:TBP/ODE and 0.8(1-x) mL of 0.75 M S:TBP/ODE was injected to the flask. The nanocrystals were grown for 2 hours and sample aliquots of 2 mL were pulled from the reaction vessel at 2, 10, 30, 60, 90, and 120 minutes for S:Se anion injection ratios of 1:9, 3:7, 1:1, 7:3, and 9:1. The aliquots of 2 mL were divided into 2 eppendorf tubes and quenched with 1 mL of a 3:2 mixture of butanol:ethanol and precipitated *via* centrifugation for 4 minutes at 15,500 rpm. Further cleaning was carried out by solvating in toluene and subsequent precipitation with ethanol *via* centrifugation; the cleaning step was repeated once. The nanocrystals were suspended in deoxygenated anhydrous toluene for ultrafast fluorescence upconversion spectroscopy measurements. Nanocrystals were characterized by UV-vis absorption and fluorescence spectroscopy, HR-TEM, EDS, STEM-EDS, and femtosecond fluorescence upconversion spectroscopy.

2.2 Post-Synthesis Ligand Modification of CdSe

2.2.1 Pyridine Exchange on Oleic Acid CdSe

In order to successfully ligate P3HT to CdSe nanocrystals, it was found that the native oleic acid ligands on the surface of the CdSe nanocrystals first had to be exchanged for pyridine. The pyridine exchange procedure was adapted from Lokteva *et al.*[41] and was accomplished by precipitating OA-CdSe with ethanol by adding ethanol to a solution of OA-CdSe nanocrystals until flocculation was observed, followed by centrifugation. The supernatant was discarded and after drying, the pellet of nanocrystals was dissolved in neat pyridine. The nanocrystals were stirred for three days at 90°C. After three days, pyridine ligated CdSe (pyr-CdSe) were purified via precipitation with acetone and centrifugation at 15,000 rpm for 2 – 4 minutes. The cleaning step was repeated once. The ligand exchange was characterized *via* absorption and fluorescence spectroscopy and ^{1}H NMR spectroscopy performed on a 400 MHz Bruker AV400 NMR spectrometer.

2.2.2 Pyridine-functionalized Poly(3-hexylthiophene) Exchange on Pyridine CdSe

Successive ligand exchange of the pyr-CdSe nanocrystals for 2- and 3-pyridyl-poly(3-hexylthiophene) (P3HT) was accomplished by placing 0.5 mL of ~20 µM pyridyl-CdSe in a 2 mL Eppendorf tube and filling with hexanes (1.5 mL), followed by centrifugation. After the supernatant was discarded and the nanocrystal pellet dried, the nanocrystals were dissolved in a 6 mg/mL solution of the 2- or 3-pyridyl-P3HT in chloroform, stirring overnight at room temperature. The ligand exchange was characterized *via* absorption and fluorescence spectroscopy and ^{1}H NMR spectroscopy performed on a 400 MHz Bruker AV400 NMR spectrometer.

2.3 Characterization of Nanocrystals

2.3.1 Static Optical Absorption and Fluorescence Spectroscopy

Static optical absorption and fluorescence spectroscopy are commonly employed to evaluate nanocrystal size and dispersity based on the wavelength of the first excitonic absorption peak and the full-width at half-maximum (FWHM) of the fluorescence peak, respectively.[42] Absorption spectra were obtained using a Varian Cary 50 UV-Vis spectrophotometer and photoluminescence spectra were obtained with an ISS PC1 Photon Counting Spectrofluorimeter or a Photon Technology International QuantaMaster 40.

2.3.2 Photoluminescence Quantum Yield

The photoluminescence quantum yield ($PLQY$) measurement is an experimental technique by which one can quantify the 'brightness' of emissive samples. The value itself is a measure of how many photons the sample emits in relation to how many it absorbed:

$$PLQY = \frac{\#\, photons\ emitted}{\#photons\ absorbed} \times 100\% \tag{2.2}$$

Photoluminescence quantum yields of graded alloy CdS_xSe_{1-x} nanocrystals dispersed in toluene were obtained using the single-point method.[43] This is a comparative method that enables determination of the sample's photoluminescence quantum yield by comparing absorption and photoluminescence of the sample with that of an organic dye of known quantum yield. Photoluminescence quantum yields were determined according to:

$$PLQY = Q_R \frac{I}{I_R} \frac{OD_R}{OD} \frac{n^2}{n_R^2} \tag{2.3}$$

where I is the integrated fluorescence intensity, OD is the optical density or absorbance of the sample at excitation wavelength, and n is the refractive index of the solvent; subscript R denotes values for the reference organic dye of known quantum yield. Optical densities of the nanocrystals and organic dyes were maintained between 0.09 and 0.1 over a 10 mm path length. Laser dyes with optical absorption and fluorescence spectra that overlap those of the nanocrystal samples were, depending on the sample, Coumarin 153 in ethanol (Q=0.38)[44], Rhodamine 6G in methanol (Q=0.94),[45] or Sulforhodamine B in ethanol (Q=0.69)[46]. Absorption spectra were obtained using a Varian Cary 50 UV-Vis spectrophotometer and photoluminescence spectra were obtained with a Photon Technology International QuantaMaster 40 for photoluminescence quantum yield determination.

2.3.3 Transmission Electron Microscopy and Energy Dispersive X-ray Spectroscopy

High-resolution transmission electron microscopy (HR-TEM), energy dispersive x-ray spectroscopy (EDS), and scanning-TEM-EDS (STEM-EDS) were obtained using a FEI Tecnai Osiris^{TM} S/TEM electron microscope equipped with ChemiSTEM^{TM} technology. Samples were prepared by drop-casting a single droplet of dilute (faintly colored to the naked eye) nanocrystal solution onto an ultrathin carbon on holey carbon TEM grid (01824 - Ted Pella, Inc.). The excess solvent was then wicked away with a Kimwipe and the grid was allowed to dry. HR-TEM images were analyzed using ImageJ software for manual determination of nanocrystal size distributions. EDS spectra were analyzed using FEI TIA offline image analysis software for chemical composition determination.

2.3.4 Nuclear Magnetic Resonance Spectroscopy

^{1}H and ^{31}P NMR spectroscopy were performed on a 400 MHz Bruker AV400 NMR spectrometer. ^{14}N NMR spectroscopy was performed on a 500 MHz Bruker DRX500 NMR spectrometer. ^{1}H and ^{31}P NMR samples were prepared by dissolving ~5 mg of rigorously purified nanocrystal samples in 0.5-0.6 mL of an appropriate deuterated solvent in which the sample is soluble. ^{14}N NMR required greater amounts of sample to observe signal, so ~60 mg of sample was required and dissolved in 0.5-0.6 mL of deuterated solvent. Deuterated solvents commonly employed included chloroform-d, toluene-d8, acetone-d6, and deuterated water.

Acquisition parameters for all NMR spectroscopy experiments were typically those found standard in the acquisition protocol in the NMR software (Bruker Topspin) in the small molecule NMR facility at Vanderbilt University. In some cases modifications were made to the number of scans (NS) in order to increase the intensity of the observed signal or to the spectral width (SW) and transmitter frequency offset (O1P) to ensure the region of interest for the appropriate functional group for the selected nucleus was being interrogated. Note that both SW and O1P are in units of ppm. For ^{1}H NMR nanocrystal samples, NS was sometimes increased to 64 or even 128 if there was little observed signal. For ^{31}P NMR nanocrystal samples, NS was set to 512, SW was set to 200.4, and O1P was set to 68.08. For ^{14}N NMR experiments on nanocrystal samples NS was set to 10000, SW was set to 401.1, and O1P was set to 0. Also note that for all ^{14}N NMR experiments, the receiver gain (RG) was left at the maximum value of 16384. When the ^{14}N NMR region of interest was expanded to search for resonance signal for P-CIS (see section 4.2.3), NS was set to 12288, SW was set to 801.8, and O1P was set to 600. All NMR spectra were processed and analyzed using Bruker Topspin 3.2 software.

2.4 Femtosecond Fluorescence Upconversion Spectroscopy

2.4.1 The Upconversion Technique

Fluorescence upconversion is a powerful, two-pulse technique that can yield sub-picosecond time resolution and is an excellent tool for studying the charge carrier dynamics of nanocrystals. This spectroscopic method observes the frequency mixing of incoherent fluorescence from the sample with another gate (probe) pulse in a nonlinear optical crystal.[47,48] Since the speed of light is effectively constant, time resolution is obtained by delaying one of the pulses relative to the other by means of a mechanical optical delay stage. At time t=0, the sample is excited by the wavelength-tunable excitation pulse. The resulting incoherent fluorescence is frequency-mixed with a gate laser pulse, arriving at time $t = \tau$ in a nonlinear mixing crystal. The frequency mixing of the fluorescence and probe beam generates light at the sum frequency (ω_{sum}) according to:

$$\omega_{sum} = \omega_{fluorescence} + \omega_{gate} \tag{2.4}$$

Frequency is inversely proportional to wavelength, and the upconverted wavelength ($\lambda_{\mathrm{upconverted}}$) is determined as follows:

$$\frac{1}{\lambda_{upconverted}} = \frac{1}{\lambda_{fluorescence}} + \frac{1}{\lambda_{gate}} \tag{2.5}$$

As stated above, the time interval (τ) between the excitation and gate pulse is regulated by changing the distance one of the pulses must travel. In our experimental setup, the excitation beam path includes the mechanical optical delay stage (fig. 2.1), thereby altering the path length of the excitation pulse while the gate pulse is constant in time. To obtain the fluorescence intensity versus time spectrum, the relative delay time (τ) is scanned and the intensity of the sum frequency is measured with a UV-sensitized photomultiplier tube at each delay time.[48] Because fluorescence upconversion observes radiative recombination, any nonradiative processes that occur in competition with a radiative process are measured indirectly and are realized as a depletion of radiative recombination, seen experimentally as a decrease in the observed fluorescence intensity.

2.4.2 Experimental Setup

Femtosecond fluorescence upconversion spectroscopy was performed with a laser system previously described,[8,9] with modifications.[49] A Coherent Verdi V18 (CW, 532nm, 18W) pumped a mode-locked Ti:Sapphire oscillator (Mira 900 Basic, Coherent) which then seeded a regenerative amplifier (RegA 9000, Coherent). The RegA powered an optical parameteric amplifier (OPA 9400, Coherent), from which the excitation (wavelength tunable, 450-700 nm) and gate (800 nm) pulses were extracted. The system operated at 250 kHz and produced pulses ~200 fs, leading to instrument response functions (IRFs) <250 fs. Samples were pumped at 50 nm higher in energy than band edge absorption to eliminate upconversion of scattered pump photons in the upconverted fluorescence spectra. Samples were of optical density ~0.9 (always <1) at pump energy and were stirred under UHP Ar in a 2 mm cuvette to avoid buildup of photo-charged dots. A rhodium coated elliptical reflector focused sample emission onto a nonlinear crystal (1 mm XC8-$LiIO_3$-Type-I SFM-800/500-1000//308-444 nm, Cleveland Crystals, Inc.). A UV-dispersing prism (STS#37261, CVI Laser Corp.) separated upconverted signal from any residual photons. The signal was directed into a UV-optimized monochromator (McPherson), detected by a photon-counting photomultiplier tube (R1527P, Hamamatsu) and digitized with a photon counter (SR400, Stanford Research Systems).

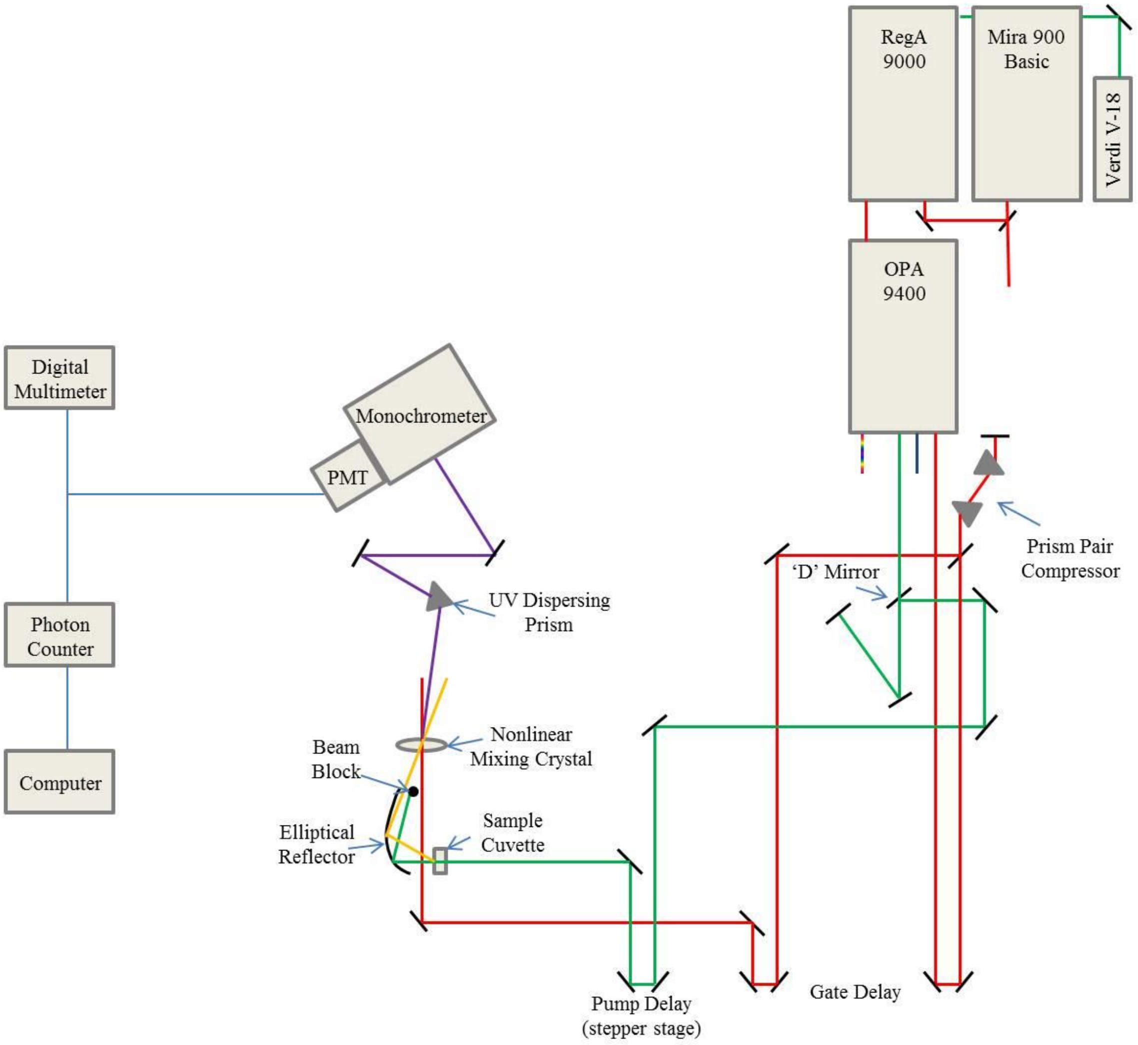

Figure 2.1. Schematic of ultrafast fluorescence upconversion experimental setup.

2.4.3 Data Analysis

The fitting function used to analyze the data was derived from the convolution of the Gaussian instrument response function ($f(W,t)$) centered at $t = 0$ with a full-width at half-maximum (FWHM) of W with a decaying exponential ($g(A,\tau,t)$) with decay lifetime τ and pre-exponential factor A:[50]

$$\mathrm{f}(\mathrm{W},\mathrm{t}) = \left(\frac{2\sqrt{\ln 2}}{W\sqrt{\pi}}\right)\exp\left[-4t^2\,\frac{\ln 2}{W^2}\right] \tag{2.6}$$

$$g(A,\tau,t) = A\exp\left(\frac{-t}{\tau}\right) \tag{2.7}$$

The convolved fit fuction (Fit) includes the addition of a time shift (t_0) to allow the Gaussian to float relative to the exponentials and an offset (y_0) so the exponentials decay to baseline instead of zero:

$$Fit = \sum_{i=0}^{n}\left[\frac{A_i}{2}\left(1 + erf\left[\left(\frac{1}{4}\right)\frac{8(t-t_0)(\ln 2) - {W^2}/{\tau_i}}{W\sqrt{\ln 2}}\right]\right)\exp\left[\frac{-\left({16(t-t_0)(\ln 2)}/{\tau_i}\right) - {W^2}/{\tau_i{}^2}}{16\ln 2}\right]\right] + y0 \tag{2.8}$$

where A_i is the i^{th} decay amplitude, W is FWHM of the Gaussian IRF, and τ_i is the i^{th} decay time. The fit function is the summation of as many convolved functions as observed decay processes.

The data were fitted *via* a custom procedure in Igor Pro, which utilizes the Levenberg-Marquardt algorithm (LMA) to search for the coefficient values that minimize chi-square and estimates the standard deviation of the fit coefficients. Each decay curve was fit with the minimum number of exponential decays that would accurately fit the data as determined *via* analysis of the curve fit residuals, minimum reduced chi-square values, and estimated standard deviation values in relation to the respective values of the fit parameters. For example, ultrafast fluorescence data for the 2 min aliquot pulled from the 1:1 S:Se anion injection ratio synthesis of graded alloy CdS_xSe_{1-x} nanocrystals (see Chapter V) were best fit with three exponential decays.

The value for the reduced chi-square for the fit function saw a significant reduction from 2.14 down to 1.18 when increasing the number of exponential decays from two to three. Therefore, addition of a third exponential decay in the data analysis improved the fit of the curve to the data. Conversely, ultrafast fluorescence data for the 120 min aliquot pulled from the same 1:1 S:Se anion injection ratio synthesis of CdS_xSe_{1-x} nanocrystals were best fit with two exponential decays. When increasing the number of exponential decays in the data fitting analysis to three, the reduced chi-square value was not changed from 1.07 indicating the introduction of an additional exponential decay did not improve the fit of the curve to the data. Additionally, when the third exponential decay was added, the estimated standard deviation for τ_1 became larger than the actual value of τ_1 ($\tau_1 = 6 \pm 18\, ps$). Thus, two exponential decays were determined to be the minimum number of exponential decays required to accurately fit the data.

The fitting was extended over positive and negative times with t_0 corresponding to arrival of the excitation pulse. Due to the nature of the pump source from the optical parametric amplifier (OPA), an instrument artifact – corresponding to upconversion of the monitored wavelength in the residual white light continuum from the OPA arriving in “negative” time – was observed as a deviation from and return to baseline before excitation, as seen in figure 2.2. This artifact was masked from the data (and plots) during analysis in order to retain a $y0$ value consistent with the baseline signal in negative time for the decay curves.

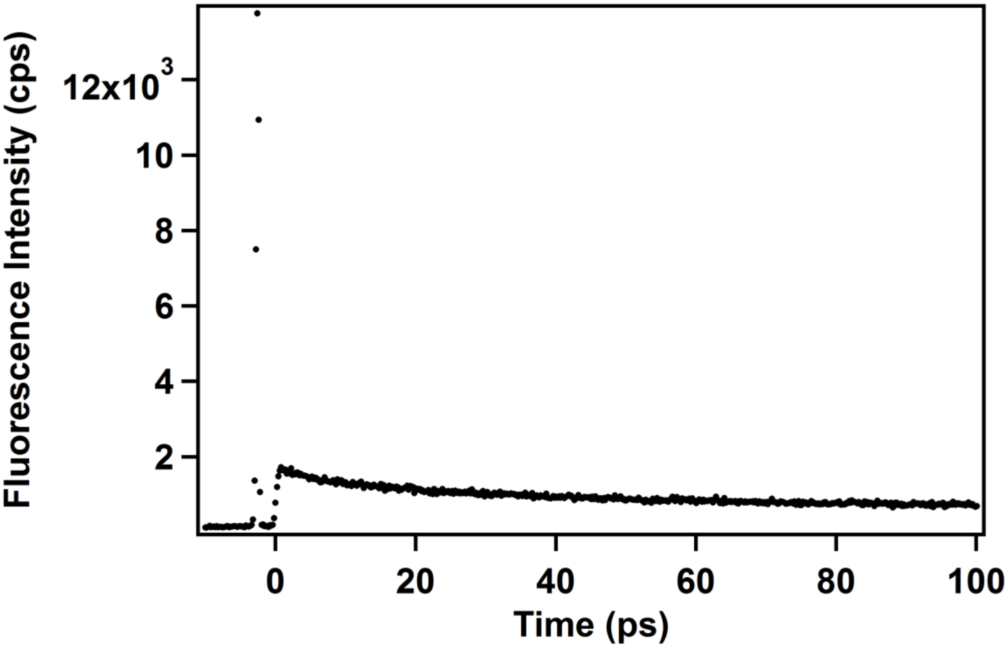

Figure 2.2. Raw fluorescence decay data for graded alloy $CdS_{0.25}Se_{0.75}$ nanocrystals[49] illustrating the instrument artifact in negative time that deviates from and returns to baseline (y_0) and, importantly, does not overlap with the sample fluorescence signal. Excitation was at 529 nm and detection was at 597 nm. Reprinted with permission from Keene, J. D.; McBride, J. R.; Orfield, N. J.; Rosenthal, S. J. Elimination of Hole-Surface Overlap in Graded CdS_xSe_{1-x} Nanocrystals Revealed By Ultrafast Fluorescence Upconversion Spectroscopy. *ACS Nano* **2014,** *8* (10), 10665-10673. Copyright 2014 American Chemical Society.

CHAPTER III

P3HT LIGATION TO CdSe NANOCRYSTALS

3.1 Introduction

Semiconductor nanocrystals, or quantum dots, have been heavily studied for their potential applications in photovoltaics, solid state lighting, and fluorescence imaging because of their unique size-dependent optoelectronic properties.[51-53] A powerful method to quantify nanocrystal properties is to probe the carrier dynamics through ultrafast fluorescence upconversion spectroscopy. Foundational studies on CdSe nanocrystals demonstrated the size and surface dependence of the carrier dynamics, wherein radiative emission was observed for band edge recombination and also for the mid-gap deep-trap state.[11] The short-lived component of the carrier dynamics was attributed to surface selenium dangling bond electrons annihilating the hole left in the valence band upon photo-excitation of the nanocrystal and was determined to be 2-6 ps, varying with nanocrystal size. The long-lived component of the carrier dynamics was attributed to the "dark exciton" effect, an optically forbidden transition from the triplet state on the order of a few nanoseconds.[22] Further studies demonstrated the strong dependence of the carrier dynamics on the surface composition of the nanocrystals by varying synthetic precursors, co-coordinating solvents, organic capping ligands, and inorganic shelling materials.[8,10]

These foundational studies illustrated the importance of nanocrystal surface on the behavior and dynamics of the charge carriers in semiconductor nanocrystals and have since led to many investigations wherein surface capping material was selected to exhibit control over charge carrier behavior. Many of these studies focused on creating nanocrystal surface interfaces that promote charge separation and/or transfer.[54,55] This behavior is desired as carrier recombination is currently a major contributor to low efficiencies in quantum dot photovoltaics (QDPVs). One of the most researched polymers for use in QDPVs is poly(3-hexylthiophene) (P3HT) due to its its high field effect hole mobilities and its type II band alignment with CdSe as shown in figure 3.2b, which promotes hole transfer to the polymer.[56] Studies have been reported that demonstrate charge transfer from CdSe to P3HT in films[57,58] and fluorescence quenching through ligation of P3HT to CdSe,[59,60] yet charge transfer between ligated P3HT/CdSe has not been demonstrated.

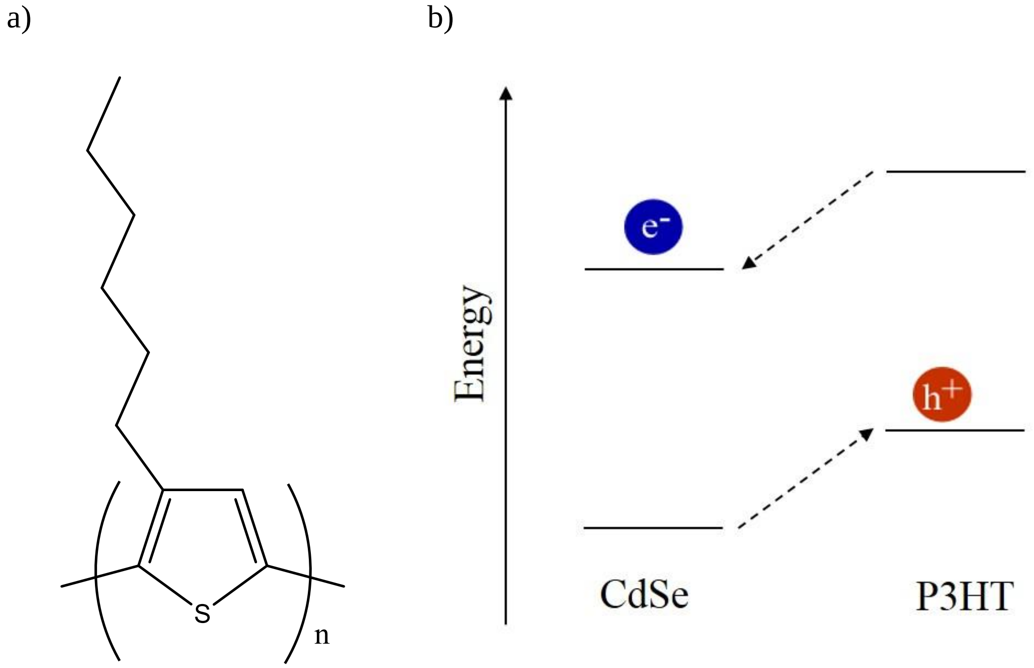

Figure 3.1. Structure of P3HT (a) and the schematic energy level diagram demonstrating the band offset characteristic of type II band alignment (b).[56]

In order to ligate P3HT to CdSe nanocrystals, the P3HT chains required a functional group that would bind to the surface of the nanocrystals. Collaborators S. Michael Kilbey, II, Ph.D., Deanna L. Pickel, Ph.D., and W. Michael Kochemba, Ph.D. of the University of Tennessee and Oak Ridge National Laboratory synthesized and provided two different pyridine-functionalized P3HT (pyridyl-P3HT) samples – 2-pyridyl-P3HT and 3-pyridyl-P3HT – *via* quenching of the Grignard metathesis polymerization.[61,62] The intent of the functionalization is to provide an anchor group to the P3HT polymer through which the polymer can ligate to the surface of CdSe nanocrystals.

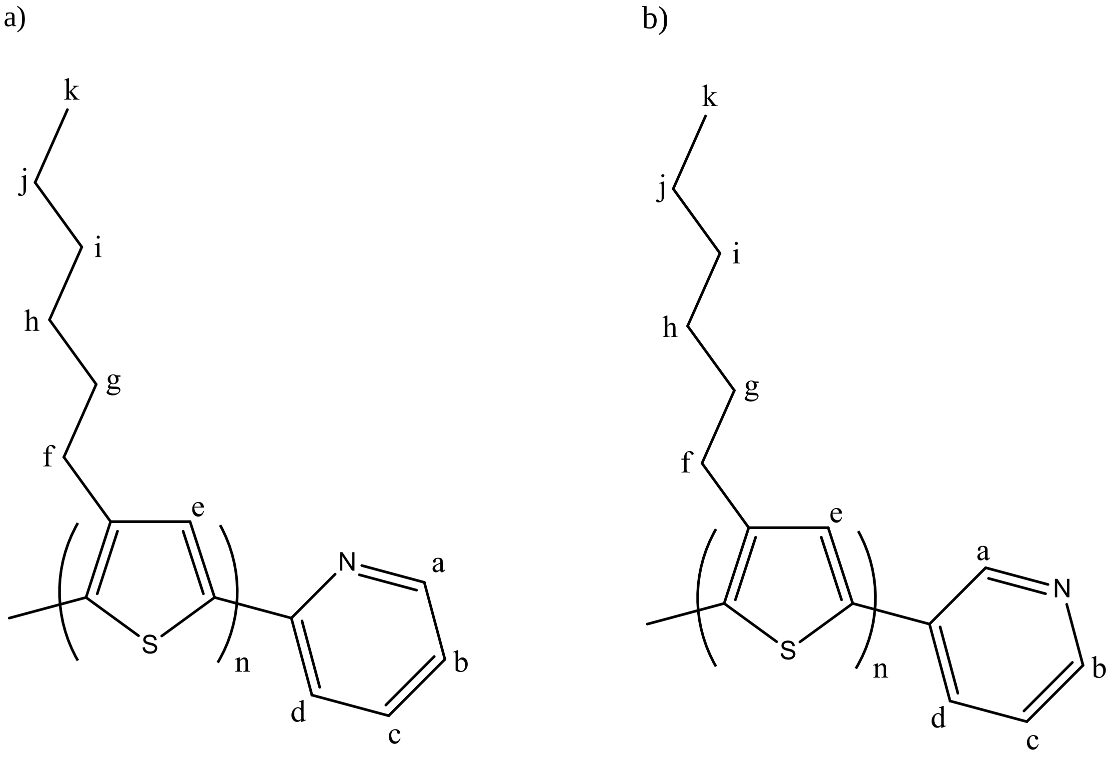

Figure 3.2. Structures of pyridyl-P3HT samples ligated to CdSe nanocrystals.[61,62] a) 2-pyridyl-P3HT and b) 3-pyridyl-P3HT, both with protons labeled to facilitate ^{1}H NMR peak assignment (see figures 3.9 and 3.10).

3.2 Results and Discussion

A two-step post-synthetic modification scheme was a successful route to polymer-ligated CdSe nanocrystals and was validated *via* analysis of the optical properties of the samples and ^{1}H NMR spectroscopy. This route involved first synthesizing CdSe with oleic acid (OA), next exchanging the OA with pyridine, and finally exchanging the pyridine for 3-pyridyl-P3HT or 2-pyridyl-P3HT. It should be noted that this procedure was attempted with various size CdSe nanocrystals but small nanocrystals aggregated upon pyridine exchange and were insoluble in all solvents, and further pursuit in the ligand exchange processes was prohibited; therefore, all data presented herein on successful ligand exchanges utilized 4.8 nm OA-CdSe. Few details regarding the synthesis of "small" oleic acid CdSe at low temperatures can be found in appendix A. Optical analysis (Fig. 3.3) of the pyridine exchange of the OA-CdSe nanocrystals yielded a slight blue shift in the absorbance while the fluorescence decreased in intensity and experienced some broadening. Since the ligand exchange process is known to have the potential to strip away some surface atoms from the nanocrystal when the ligands are removed from the nanocrystal surface,[21] the blue-shift observed after the exchange procedure supports that ligand exchange has occurred because atoms removed from the surface would decrease the diameter of the nanocrystal, resulting in a greater degree of quantum confinement as evident in the observed blue-shift in absorbance spectra. It should be noted, however, that this data is only suggestive of ligand exchange occurring and cannot provide information about the actual surface chemistry of the nanocrystals. Therefore, the optical data is complementary to a more detailed analysis of the surface chemistry of the ligand exchanged nanocrystals.

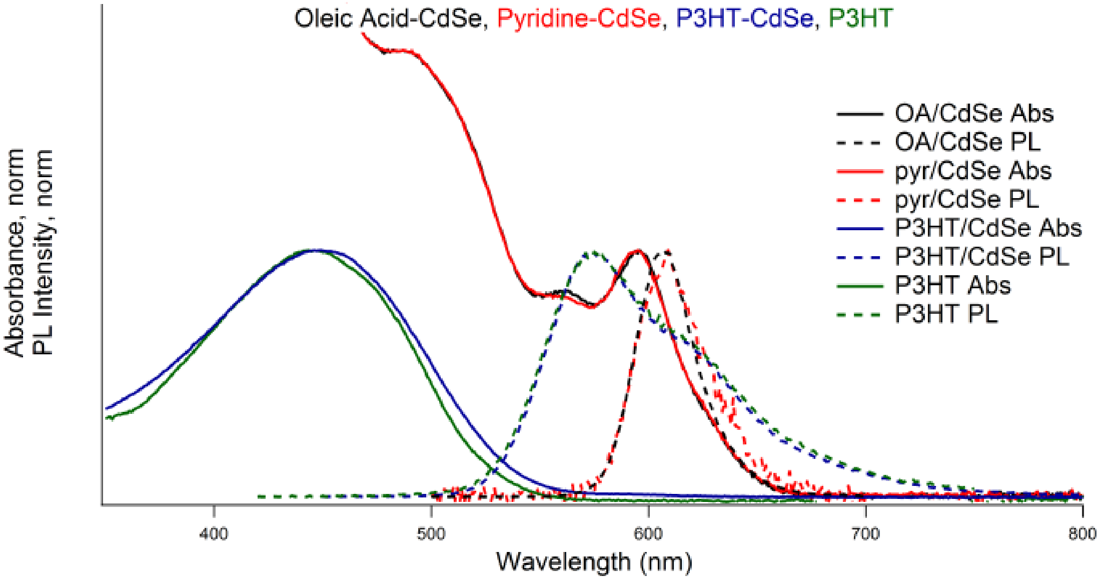

Figure 3.3. Optical analysis of OA-CdSe nanocrystals (black) exchanged with pyridine (red), then exchanged with 3-pyridyl-P3HT (blue). Also shown is the optical data for P3HT (green). Change in the absorbance/fluorescence with each step is indicative that ligand exchange is occurring.[21]

The first ligand exchange was further verified through ^{1}H NMR spectroscopy. ^{1}H NMR spectroscopy is an invaluable technique to probe the presence and binding of molecules that comprise the surface chemistry of semiconductor nanocrystals. The binding of ligands to the surface of nanocrystals is readily apparent the NMR spectra of the nanocrystals, in that the chemical environment is altered resulting in a difference of chemical shift, in addition to reduced molecular rotation and inhibited dipolar coupling, which leads to broadening of the signal and loss of the hyperfine splitting.[21,63,64] As seen in figures 3.7 and 3.8, the proton signals of free (neat) pyridine differ from those of pyridine-ligated CdSe. When the pyridine molecules are bound to the surface of the nanocrystals, each of the proton resonances exhibit a downfield shift and the splitting due to J-coupling of "neighboring" protons disappears.[63] Also apparent is the signal remaining from bound oleic acid on the CdSe nanocrystals, indicating incomplete exchange of the surface ligands.

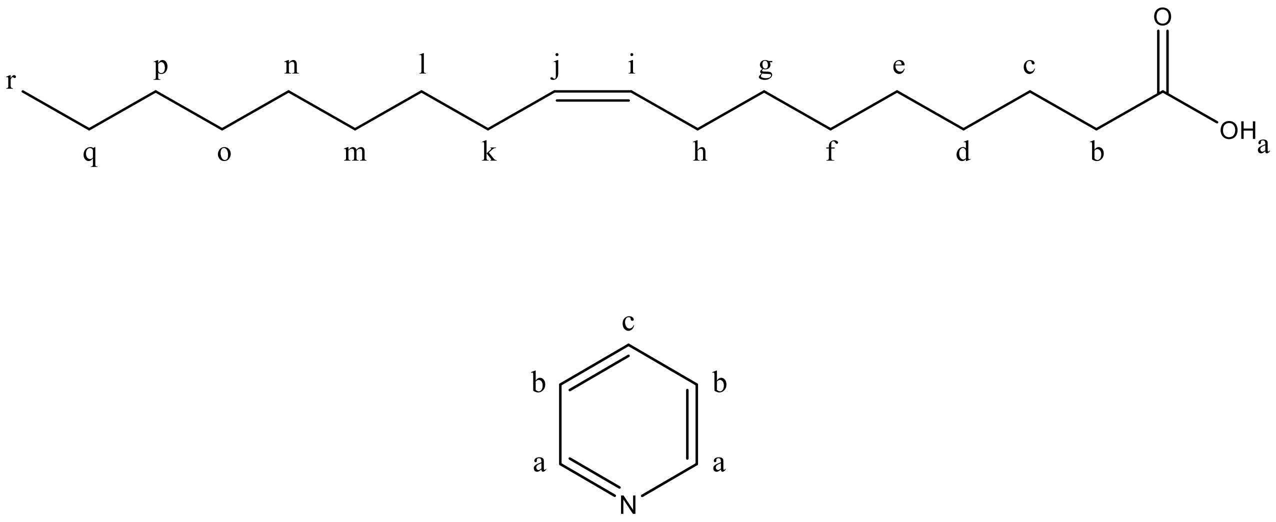

Figure 3.4. Molecular structures of oleic acid (top) and pyridine (bottom) with protons labeled as assigned in the ^{1}H NMR spectra following in figures 3.5 and 3.7.

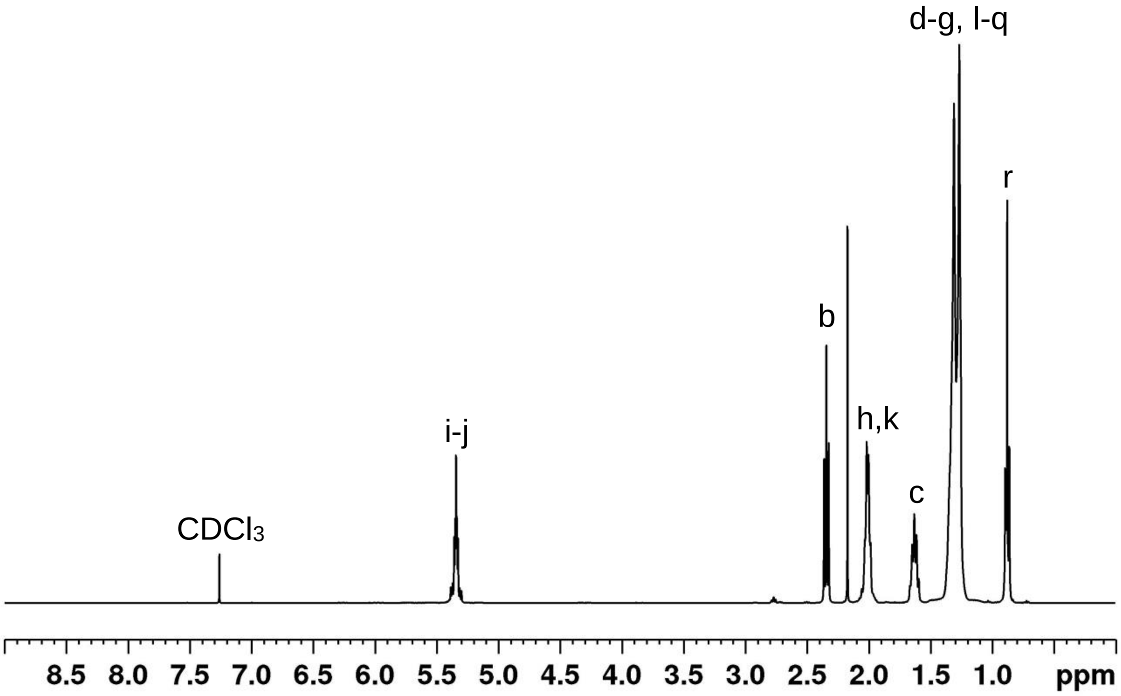

Figure 3.5. ^{1}H NMR spectrum of free oleic acid with proton signals assigned according to the labels presented in figure 3.4.

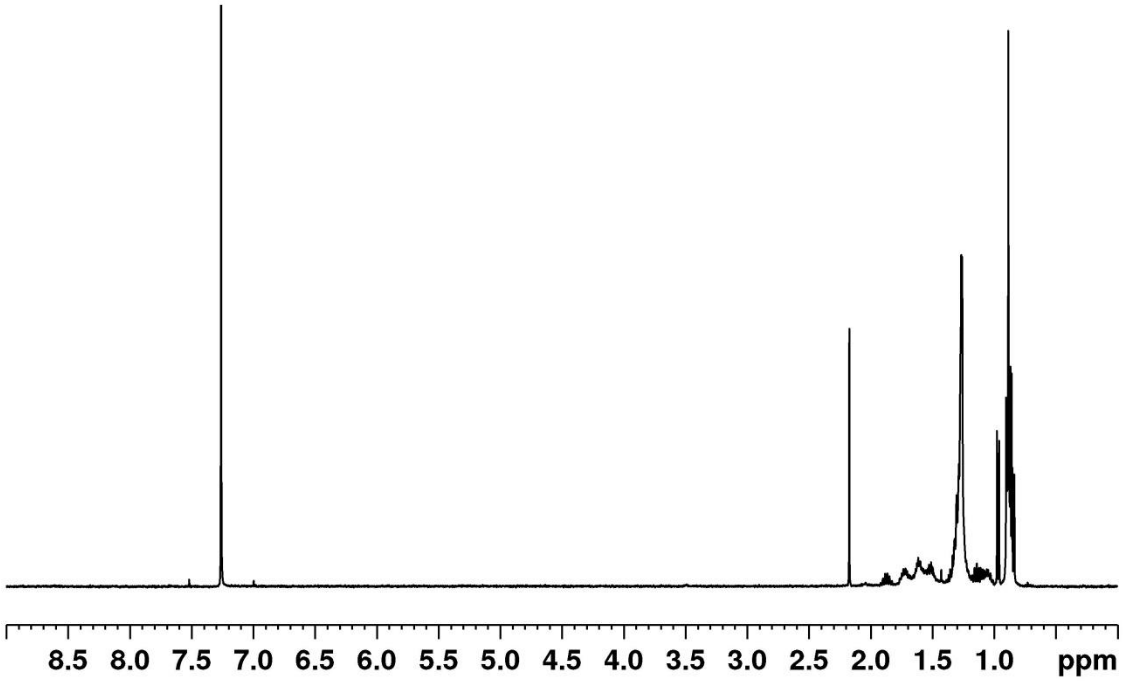

Figure 3.6. ^{1}H NMR spectrum of CdSe nanocrystals synthesized with oleic acid as the surfactant dissolved in $CDCl_3$. Bound oleic acid exhibits some broadening and chemical shift of the proton resonance signals observed while the vinyl protons' resonance signal at 5.34 ppm is not observed.

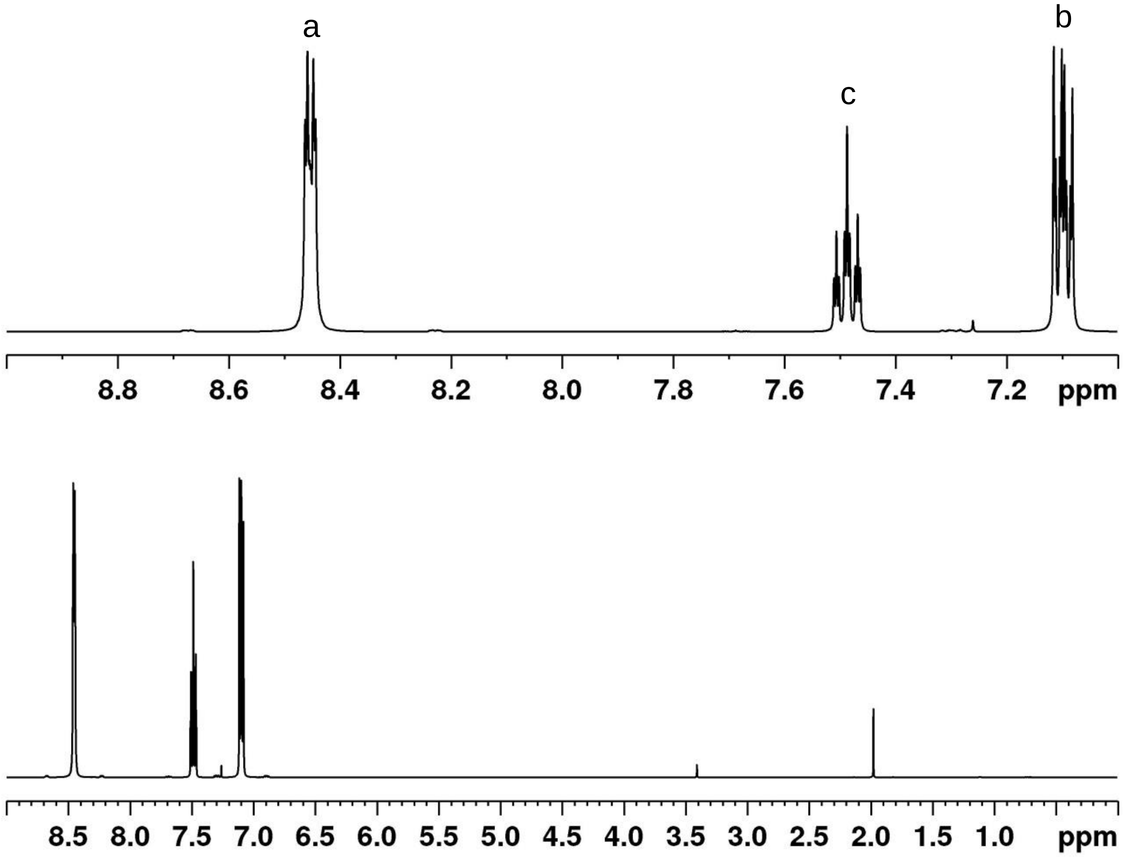

Figure 3.7. ^{1}H NMR spectrum of pyridine dissolved in $CDCl_3$. The top spectrum is an enhanced view of the proton signals in which the fine structure can be seen that results from spin-spin splitting.

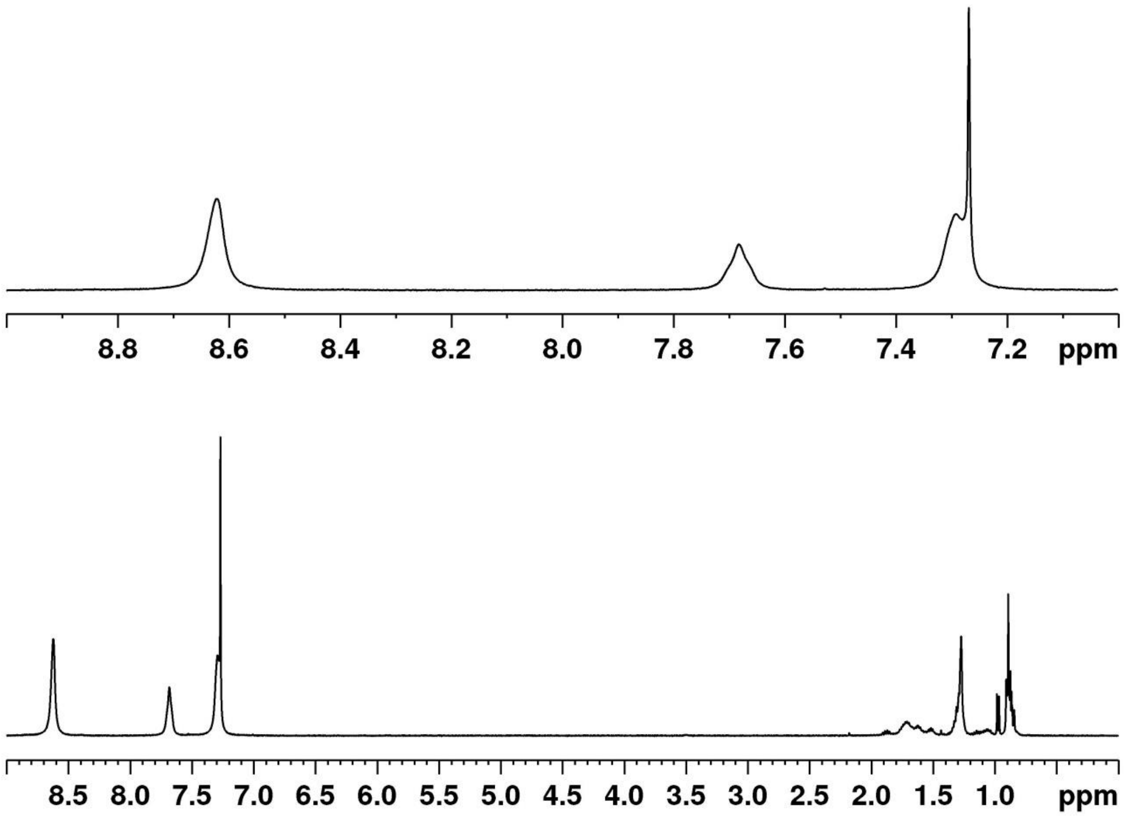

Figure 3.8. ^{1}H NMR spectrum of oleic acid CdSe nanocrystals after ligand exchange with pyridine, dissolved in $CDCl_3$. The bound pyridine proton resonances exhibit broadening as the J-coupling fine splitting disappears and shifts in ppm as the chemical environment is altered by the presence of the nanocrystal surface. Note that ligand exchange procedures are not always "complete," as evidenced in this spectrum by the presence of some bound oleic acid signal remaining on the nanocrystals.

In addition to optical analysis, ^{1}H NMR also indicated that pyridyl-P3HT was ligated to the CdSe nanocrystals after the exchange procedures. ^{1}H NMR analysis of the pyridyl-P3HT molecules allowed for identification of the proton resonance signals located on the pyridine functional group as seen in figure 3.9. A broadening and/or shift of NMR signal would indicate that pyridyl-P3HT ligands were directly attached to CdSe nanocrystals.[21,63,64] The ^{1}H NMR analysis of the 3-pyridyl-P3HT ligation to CdSe revealed an upfield shift of 0.02 ppm (8 Hz) for both proton resonances adjacent to the nitrogen of pyridine as seen in figure 3.11. Similarly, 2-pyridyl-P3HT ligation to CdSe also exhibited an upfield shift of 0.02 ppm (8 Hz) for the single proton resonance adjacent to the nitrogen of pyridine, as seen in figure 3.10.

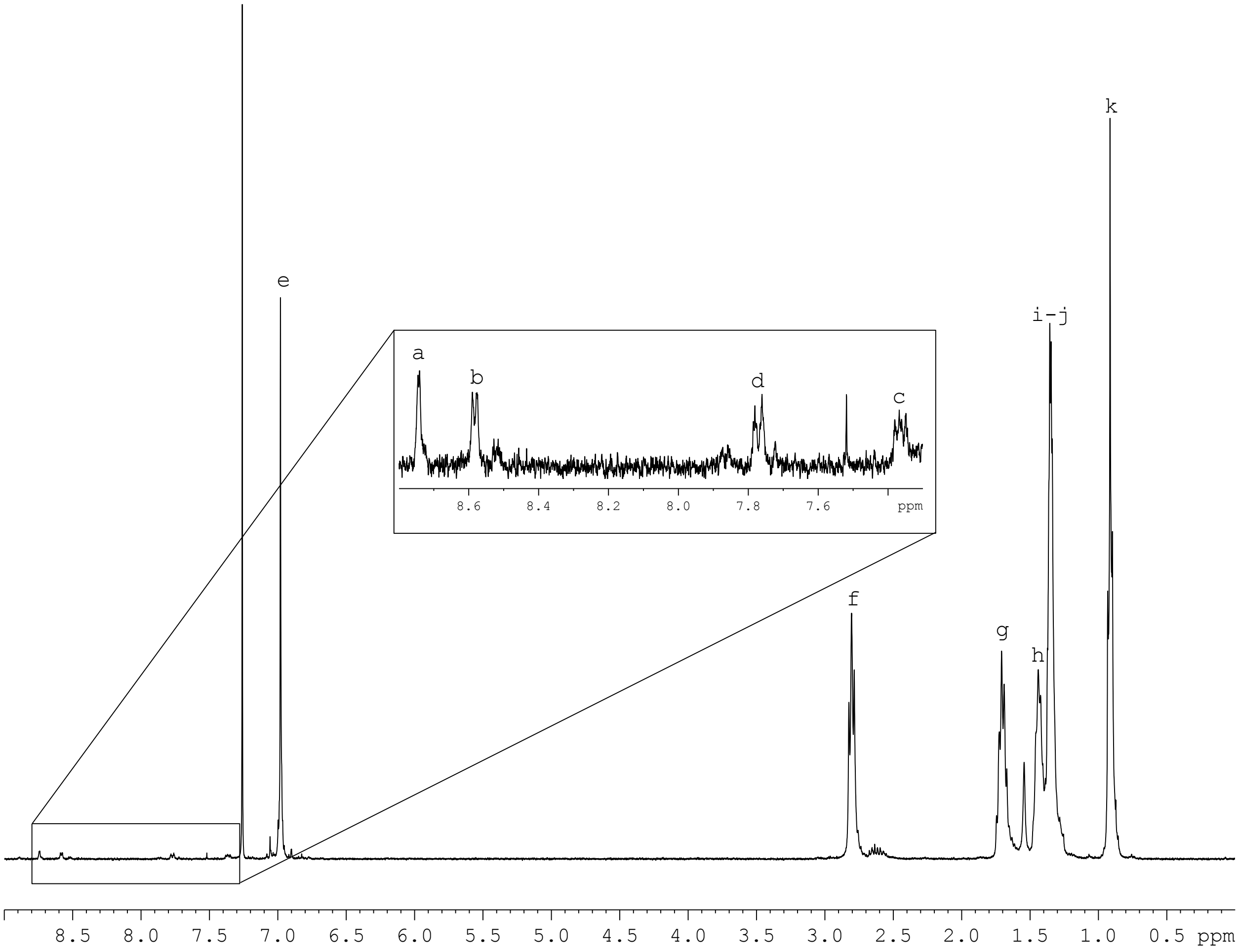

Figure 3.9. ^{1}H NMR spectrum of 3-pyridyl-P3HT. Proton signals are labeled in accord with the scheme presented in Figure 3.2b. Inset: Expanded region of interest wherein ^{1}H signals for the pyridine functional groups are located.

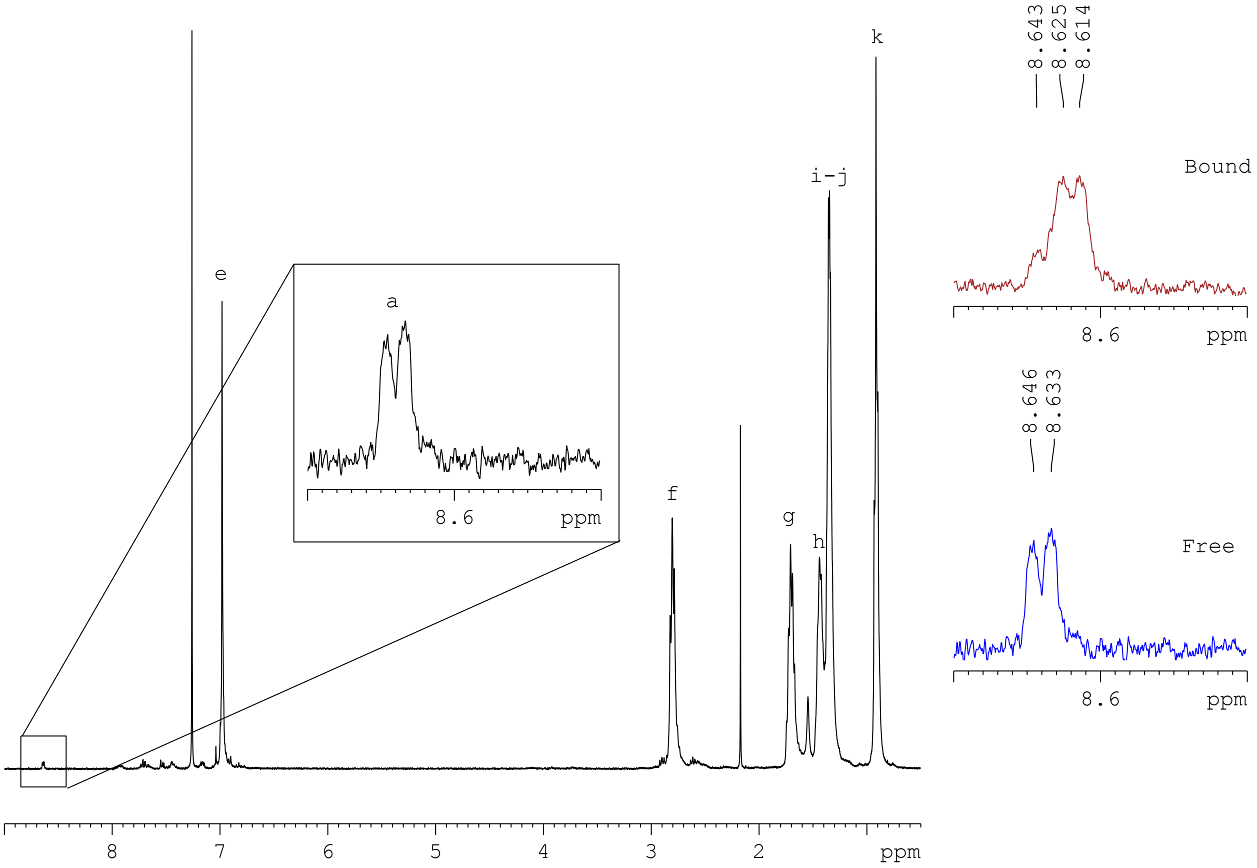

Figure 3.10. Left: ^{1}H NMR spectrum of 2-pyridyl-P3HT. Proton signals are labeled in accord with the scheme presented in Figure 3.2a. Inset: Expanded region of interest to highlight the doublet ^{1}H signal for ^{1}H$_a$, the ^{1}H adjacent to nitrogen on the pyridine functional group. Right: Comparison of the doublet ^{1}H signal for ^{1}H$_a$, for the bound (top, red) and free (bottom, blue) 2-pyridyl-P3HT. Note the 0.02 ppm upfield shift of the bound polymer indicating successful ligation and the residual free polymer remaining in the solution.

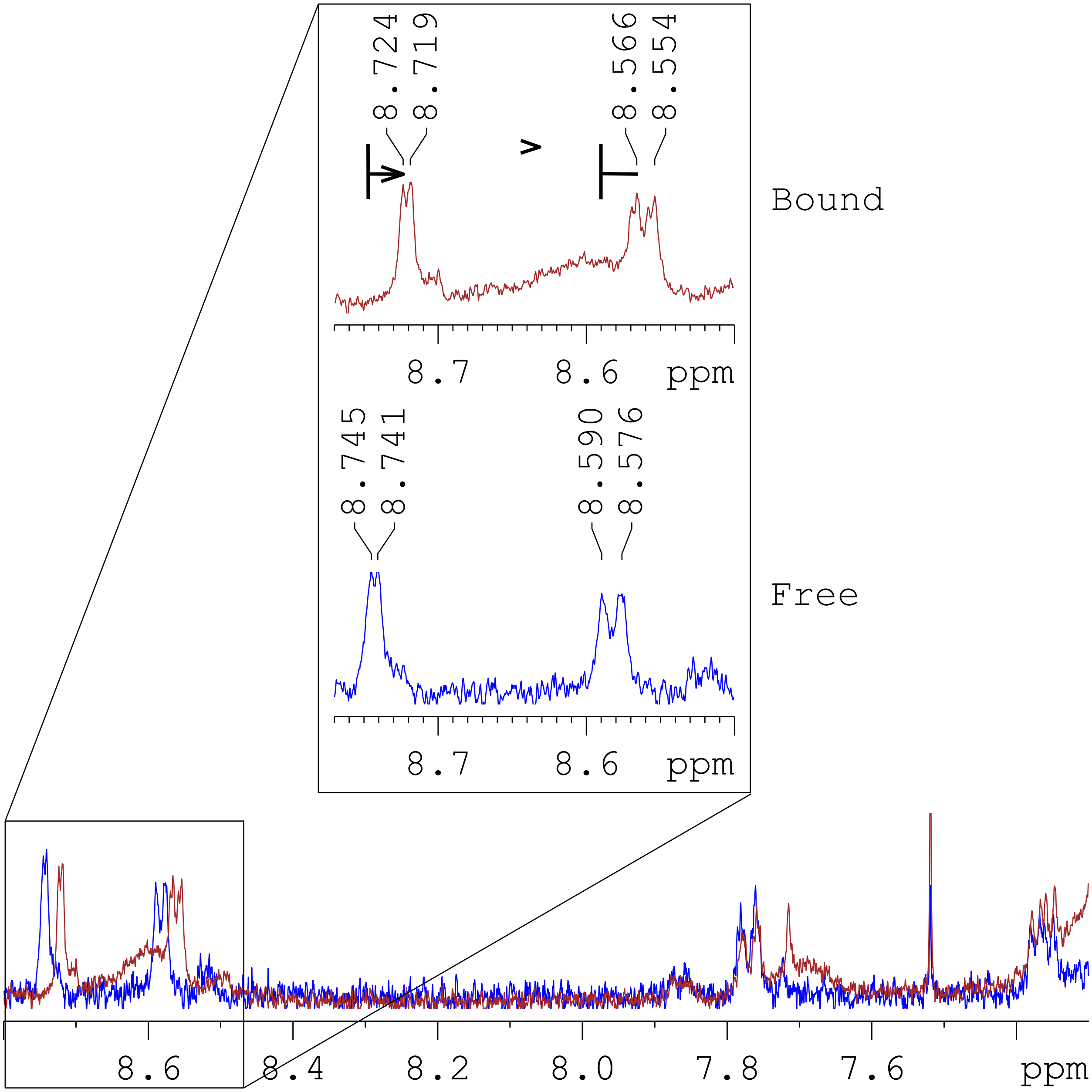

Figure 3.11. Comparison of ^{1}H NMR spectra of unbound (blue) and ligated (red) 2-pyridyl-P3HT samples, focused on the proton resonances neighboring the nitrogen of the pyridine functional group. The upfield signal shift by 0.02 ppm (8 Hz) indicates ligation.

Interestingly, the protons that exhibited a chemical shift from that of the unbound polymer ligands were only those that were located on the carbon directly adjacent to the nitrogen of pyridine, namely, proton “a” in 2-pyridyl-P3HT and protons “a” and “b” in 3-pyridyl-P3HT (see figure 3.2 for labeling of protons). This observation not only provided verification of ligation of the functionalized P3HT polymers to the surface of the CdSe nanocrystals, but also provided insight into the binding mechanism of the ligands. Theoretical simulations and experiments have shown that pyridine ligates to the surface of CdSe nanocrystals, not in a perpendicular alignment through the nitrogen, but the molecule actually binds in a parallel interaction through the conjugated π-orbital ring of the pyridine structure.[41,61,62] This is evident in ^{1}H NMR as a broadening and downfield shift of *all three* proton signals observed for pyridine after ligation to CdSe nanocrystals as shown in figure 3.8. Because only the protons adjacent to the nitrogen of pyridine exhibit a chemical shift, we are able to conclude that 2-pyridyl-P3HT and 3-pyridyl-P3HT bind through the nitrogen of the pyridine functional group. Given the large sterics of P3HT, this conclusion is feasible.

Kochemba *et al.* further investigated these pyridyl-P3HT ligated CdSe nanocrystals and dispersed them in films of P3HT at 20 weight percent, analyzing film morphology *via* high resolution transmission electron microscopy.[61,62] It was found that after annealing, the pyridyl-P3HT ligated CdSe nanocrystals maintained dispersity throughout the P3HT films and did not aggregate in comparison to native ligand CdSe nanocrystals and pyridine-ligated CdSe nanocrystals. This finding further reinforced the favorable interaction between pyridyl-P3HT and CdSe nanocrystals and demonstrated one of the primary benefits of utilizing functionalized P3HT-CdSe nano-composites in nanocrystal-polymer blend QDPVs. As shown by Kochemba *et al.*, the directly ligated polymer nanocrystal blends allow for control of final film composition and architecture and produce films of superior quality than native ligand CdSe nanocrystals, which could lead to improved performance of QDPVs.

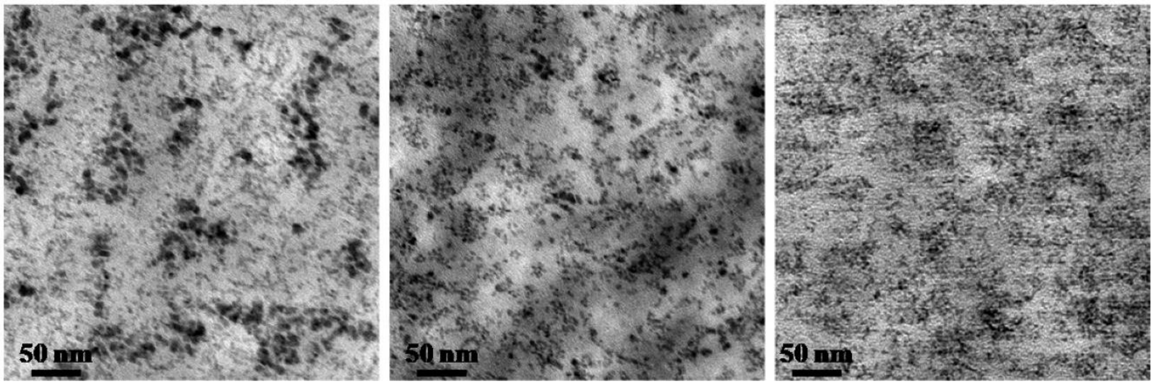

Figure 3.12. Annealed films of CdSe nanocrystals of differing ligands dispersed in P3HT. a) native ligand CdSe and b) pyridine-ligated CdSe aggregate upon annealing, whereas c) pyridyl-P3HT-ligated CdSe nanocrystals maintain good disbursement throughout the film. Adapted with permission from Kochemba, W. M.; Pickel, D. L.; Keene, J. D., Rosenthal, S. J.; Sumpter, B. G.; Chen, J.; Kilbey, S. M., II, In Situ Formation of Pyridyl-Functionalized Poly(3-hexylthiophene)s *via* Quenching of the Grignard Metathesis Polymerization: Toward Ligands for Semiconductor Quantum Dots. *Chemistry of Materials* **2012,** *24* (22), 4459-4467. Copyright 2012 American Chemical Society.

3.3 Conclusion

Ligation of 2-pyridyl-P3HT and 3-pyridyl-P3HT to CdSe nanocrystals was performed *via* a two-step post-synthetic ligand modification scheme. CdSe nanocrystals were first synthesized with oleic acid as the native ligands which were then (partially) exchanged with pyridine. Finally, pyridine-ligated CdSe nanocrystals were exchanged for 2-pyridyl-P3HT or 3-pyridyl-P3HT ligands in small scale, with limited success in purifying the P3HT-ligated CdSe nanocrystals from free P3HT. Ligation was monitored and verified using optical analysis techniques including static UV-vis absorption and fluorescence spectroscopies as well as ^{1}H

NMR spectroscopy. Blue-shifts in optical spectra indicated stripping of some atoms from the surface of the nanocrystals during the ligand exchange procedures with corresponding shifts in photoluminescence spectra coupled with decreased quantum yields. The aforementioned changes in the optical data were suggestive of ligand exchange occurring. ^{1}H NMR spectroscopy showed broadening and/or chemical shifts for the proton resonance signals adjacent to the point of ligation for pyridine, 2-pyridyl-P3HT, and 3-pyridyl-P3HT, verifying ligation of the polymers to the CdSe nanocrystal surface. Pyridyl-P3HT-ligated CdSe nanocrystals annealed in P3HT films were found to exhibit less aggregation than native ligand CdSe samples annealed in P3HT films, indicating favorable interaction between the pyridyl-P3HT CdSe nanocrystals which facilitated enhanced disbursement in the P3HT films.

3.4 Future Work

Although 2-pyridyl-P3HT and 3-pyridyl-P3HT were successfully ligated to CdSe nanocrystals through a two-step post-synthetic modification, the low affinity of pyridine for the CdSe nanocrystal surface meant that the ligands were weakly bound to the nanocrystals. This led to difficulties in purification of the P3HT-ligated nanocrystals from the excess P3HT in the exchange solution in large quantities needed for analysis of their fluorescence on the femtosecond and picosecond time scales, as is evident in the optical properties shown in figure 3.3. This, coupled with the large sample size requirements of the fluorescence upconversion experimental setup before conversion to the commercial cuvette (see Appendix B.2), which was in use during the period of these investigations, prevented direct observation of the charge transfer dynamics for the P3HT-functionalized CdSe nanocrystals, which was a major goal of this work.

These issues can be alleviated in future studies by altering the functional group on P3HT from pyridine to something that has a stronger affinity to the CdSe surface, such as carboxylic acid or phosphonic acid. Stalder *et al.* has demonstrated the strong affinity of phosphonic acid-functionalized P3HT (PA-P3HT) for CdSe nanocrystals with oleic acid as the native ligands.[60] Ligation of the PA-P3HT was verified and monitored *via* fluorescence quenching. As PA-P3HT was added to a solution of oleic acid-CdSe, charge transfer from the nanocrystal to ligand (or *vice versa*, depending on excitation and observation wavelengths) prevented carrier recombination and resultant emission of photons. Thus, the degree to which the fluorescence was quenched for the PA-P3HT-CdSe indicated the degree to which the CdSe nanocrystals were ligated with PA-P3HT.

Utilizing a higher-affinity functional group on the P3HT, as was demonstrated for PA-P3HT, should allow for sample preparation and purification to enable investigation of the fluorescence on the ultrafast time scale to probe the charge transfer dynamics. As it was in this study, the inability to purify the samples from excess unbound P3HT resulted in the CdSe nanocrystal signal being overwhelmed by the P3HT signal in the optical spectra (figure 3.3). Additionally, with the transition from the flow cell to the commercial cuvette in the fluorescence upconversion experimental setup, sample size requirements are now 0.6 mL in place of the ~20 mL needed to fill the reservoir and pump head in the old flow cell apparatus. Therefore, the scale of the sample needed is now plausible given the amount of functionalized P3HT needed to perform the ligand exchange procedures and prepare the P3HT-ligated CdSe nanocrystals.

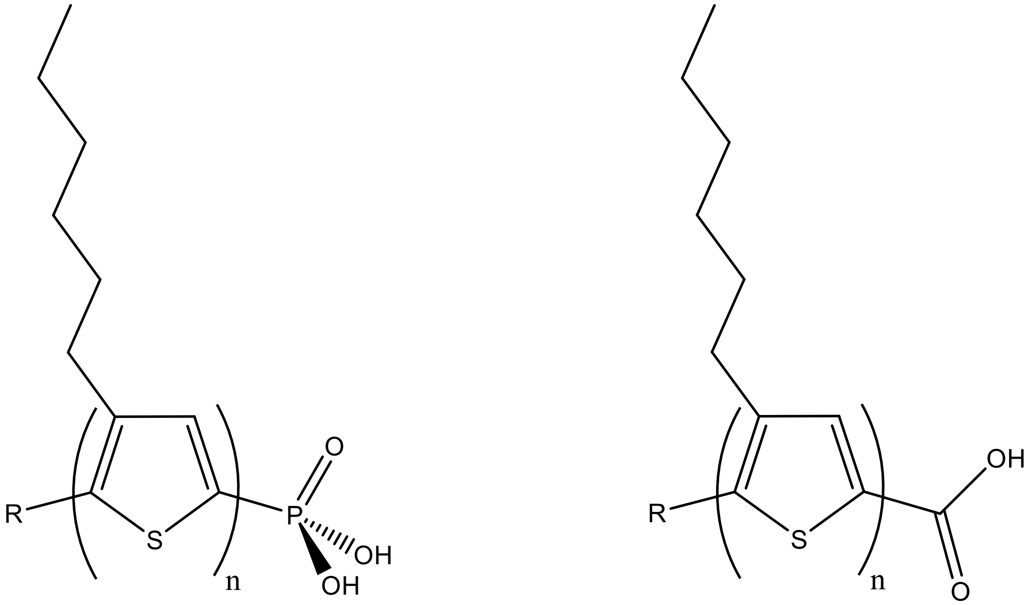

Figure 3.13. Molecular structures of a) phosphonic acid functionalized P3HT and b) carboxylic acid functionalized P3HT. These functional groups are known and have been demonstrated (in the case of phosphonic acid P3HT) to have a stronger binding affinity to CdSe nanocrystals,[60] and are therefore predicted to enable sample preparation for the fluorescence upconversion experiment to (in)directly observe the charge transfer dynamics for the type-II P3HT-CdSe system.

CHAPTER IV

NMR CHARACTERIZATION OF $Cu_xIn_yS_2$ NANOCRYSTAL SURFACE CHEMISTRY

Adapted with permission from Niezgoda, J. S.; Yap, E.; Keene, J. D.; McBride, J. R.; Rosenthal, S. J. Plasmonic $Cu_xIn_yS_2$ Quantum Dots Make Better Photovoltaics Than Their non-Plasmonic Counterparts. *Nano Letters* **2014,** *14* (6), 3262-3269. Copyright 2014 American Chemical Society.

4.1 Introduction

As semiconductor nanocrystals have increasingly been incorporated in quantum dot photovoltaics as individual photoreaction centers, taking advantage of their size-tunable absorption to maximize harvesting of the solar spectrum,[51] there have been recent efforts to develop alternative and more environmentally-friendly quantum dot materials.[65] The most-studied systems to date are CdSe and PbS, but with cadmium and lead being used, there is an inherent irony in using environmentally-toxic metals in the quest to create renewable energy sources to save the environment. One such system using environmentally-benign materials is copper indium sulfide ($Cu_xIn_yS_2$, CIS) semiconductor nanocrystals. Seminal work conducted by the Klimov research group at Los Alamos National Laboratory presented the now-widely-employed solvothermal synthesis of colloidal CIS nanocrystals.[66] However, these quantum dots contain thiols as the surfactant. Thiols as surface ligands for semiconductor nanocrystals bind strongly to the nanocrystals surface and have even been shown to be crystal-bound rather than surface-bound, further reinforcing their high binding strength.[67] Due to this high affinity for the quantum dots, the thiols have proven to be difficult to exchange for other ligands. When considering their application in photovoltaic devices, the nanocrystals must not only be able to effectively generate and separate charge carriers, but they must also be able to transfer the excited charge carriers to the device electrodes to promote charge carrier extraction to increase the efficiencies of the photovoltaic devices. The long carbon chain ligands typically employed in the synthesis of semiconductor nanocrystals are insulating to the charge carriers and inhibit the charge transfer from the nanocrystals; thus, device efficiencies have been limited.[68]

For these reasons, Niezgoda *et al.* was investigating alternative syntheses of CIS quantum dots utilizing exchangeable ligands employed in other quantum dot systems such as hexadexylamine.[69] Interestingly, some of the CIS nanocrystals that were synthesized exhibited localized surface plasmon resonances (LSPRs) in the near-infrared. The plasmonic and non-plasmonic CIS nanocrystals were found to have slightly different stoichiometries of the cationic ratios in the final quantum dot systems. However, the syntheses also involved different cation precursors that could potentially lead to differing surface chemistries. Therefore, in order to thoroughly determine the cause of the LSPR modes in the CIS nanocrystals, the surface ligands had to be investigated.

As discussed in section 3.2, ^{1}H NMR spectroscopy is an invaluable technique to probe the presence and binding of molecules that comprise the surface chemistry of semiconductor nanocrystals because bound ligands are identified through broadened and/or shifted proton resonance signals.[21,63,64] In addition to ^{1}H NMR spectroscopy, other nuclei of interest – relevant to this study – that can be probed include ^{31}P and ^{14}N. ^{31}P, like ^{1}H, is a spin-one-half ($I = 1/2$) nucleus and therefore the spin-spin splitting resulting from the J-coupling to neighboring protons is easily interpreted according to $n + 1$, yielding information on the number of chemically-equivalent neighboring protons.[70] The resonance frequency of ^{31}P is different from that of ^{1}H (300.000 MHz at 7.0463 T) and is observed at 121.442 MHz (7.0463 T).[70] By tuning the probe on the NMR spectrometer to monitor the appropriate frequency (correcting for the field strength of the spectrometer), ^{31}P NMR signal can be observed. Just as in ^{1}H NMR spectroscopy, ^{31}P NMR spectra can determine the presence and binding of phosphorous-containing molecules to the surface of nanocrystals. Specifically for the CIS syntheses studies investigated herein, phenylphosphonic acid was utilized as a precursor and was probed for its presence and binding in the CIS nanocrystals.

^{14}N, however, is often less explored in NMR spectroscopy because it is a quadrupolar, $I = 1$ nucleus and therefore does not exhibit the readily-interpreted fine structure of the spin-spin splitting according to $n + 1$ for $I = 1/2$ nuclei.[70] ^{15}N, on the other hand, is a $I = 1/2$ nucleus and therefore its fine structure spin-spin splitting spectra are much more easily interpreted to yield structural information about the molecule. However, ^{15}N has a low natural abundance of 0.365% and a low relative sensitivity for equal numbers of nuclei at constant field of only 1.04 x 10^{-3} (normalized to ^{1}H) and therefore must be significantly enriched in samples in which it is to be probed.[70] On the other hand, ^{14}N is 99.635% naturally abundant to counter a low relative sensitivity of 1.01 x 10^{-3} so its NMR signal is readily observed under natural, non-enriched conditions.[70] Additionally, ^{14}N NMR signals are very sensitive to chemical environment and exhibit very large chemical shifts. For the purpose of determining whether or not hexadecylamine is ligated to the nanocrystal, as is its purpose for these studies, a difference in chemical shift for the nitrogen signal is sufficient to indicate a difference in chemical environment that results for the near proximity of the nanocrystal surface as a result of ligation.

4.2 Results and Discussion

NMR spectroscopy was utilized to characterize the surface chemistry of the CIS nanocrystals in order to determine what organic molecules were present and/or bound to the nanocrystal surface in both the nP-CIS and P-CIS samples. Specifically, ^{1}H, ^{31}P, and ^{14}N NMR spectroscopy were utilized to probe the surface chemistry of the CIS quantum dots.

4.2.1 ^{1}H NMR Spectroscopy

^{1}H NMR spectroscopy was utilized to identify the organic molecules present and/or bound to the nanocrystals in the CIS samples.[71] As seen in figure 4.1, the bottom black trace is a spectrum of hexadexylamine taken as a point of reference for the nanocrystal samples. All proton resonance signals from the molecule are assigned according to the labels of the inset HDA structure. Of particular interest, proton resonance signals ‘a’ and ‘b’ correspond to the amine protons and the protons directly adjacent to the amine functional group, respectively. As can (not) be seen for both nP-CIS and P-CIS nanocrystals, these proton signals are not observed. This is explained by their close proximity to the quantum dot surface and is indicative of hexadecylamine being bound to the surface in both samples. Additionally, the proton resonance signals observed for the remaining ^{1}H nuclei are seen to exhibit a slight chemical shift, also indicative of direct ligation to the nanocrystal surface. If hexadecylamine was present but not bound to the nanocrystal surface, as would be the case due to insufficient purification of the nanocrystals, the ^{1}H NMR spectra would be identical to that of the free hexadecylamine spectrum (figure 4.1 bottom, black). The additional peaks that are present in the nanocrystal samples are attributed to trace amounts of residual 1-octadecene solvent (1.94 ppm), acetylacetonate precursor (1.65 ppm), and acetone from the purification procedure (1.60 ppm). Therefore, the ^{1}H NMR spectra provide evidence for ligation of hexadecylamine to the nP-CIS and P-CIS nanocrystals and do not show signal from other significant molecules being present to contribute to the surface chemistry of the quantum dots.

The synthesis of P-CIS nanocrystals involved the use of phenylphosphonic acid as a stabilizing agent to regulate the reactivity of the cation precursors.[69] Investigation of the ^1H NMR spectra yielded no observation of aromatic proton signal that would result from the presence of phenylphosphonic acid. Thus, only bound hexadecylamine was found in the ^1H NMR analysis.

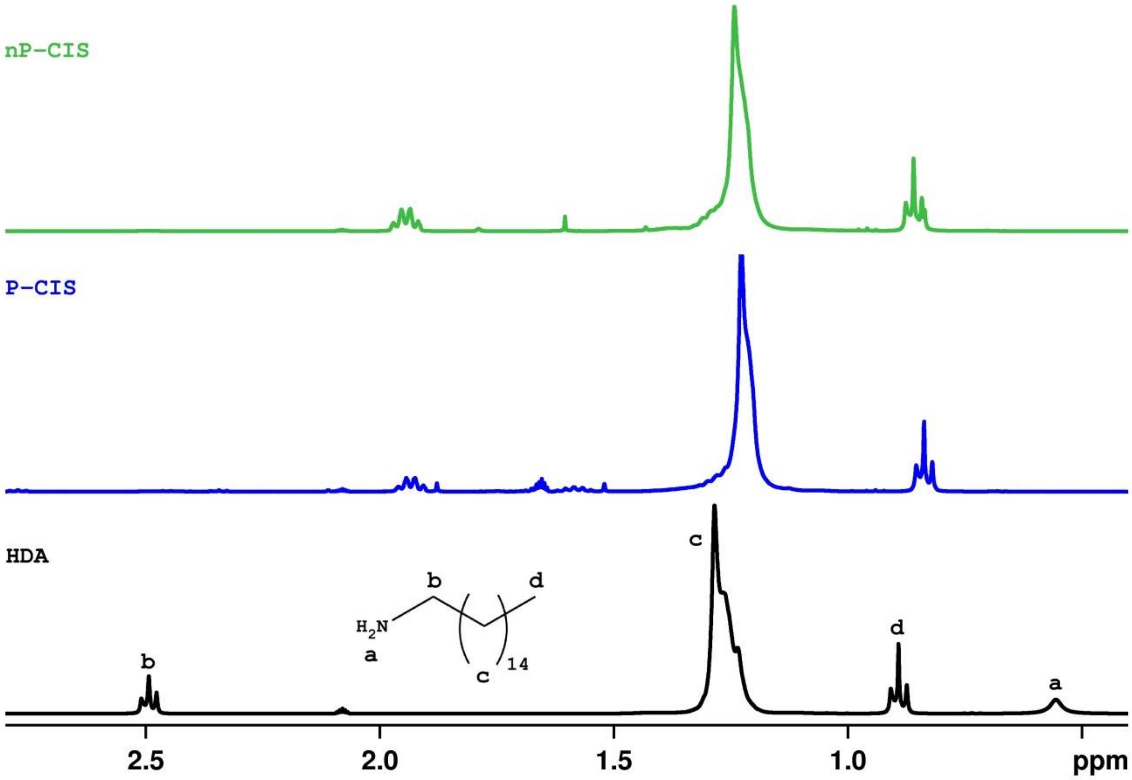

Figure 4.1. ^1H NMR spectra of nP-CIS (top, green), P-CIS (middle, blue), and free hexadecylamine (bottom, black).[71] The disappearance of proton resonances in close proximity to the nanocrystal surface in the CIS samples and the chemical shift seen for the observed proton resonance signals indicate that hexadecylamine is ligated to the surface of both the nP-CIS and the P-CIS.

4.2.2 ^{31}P NMR Spectroscopy

^{31}P NMR spectroscopy was also performed on the P-CIS sample because phenylphosphic acid was utilized in the synthesis of the plasmonic nanocrystals only to act as a stabilizing agent that regulates the reactivity of the cationic precursors during the nucleation and growth of the quantum dots.[69,71] If phenylphosphonic acid was present in the nanocrystal sample, a ^{31}P resonance signal would be observed from the phosphorus in the molecule. However, as seen in figure 4.2, no observable ^{31}P resonance signal was found in the ^{31}P NMR spectrum. While this could possibly be attributed to extreme peak broadening resulting from highly partially charged P-CIS and the potential excess of $I = 1/2$ states due to the cation vacancy densities within the nanocrystal matrix, as is the case for the ^{14}N NMR analysis discussed in section 4.2.3, the lack of evidence for phenylphosphic acid peaks in the ^{1}H NMR spectra corroborates the conclusion that no phenylphosphonic acid was present in the P-CIS nanocrystal samples either in bound or un-bound form.

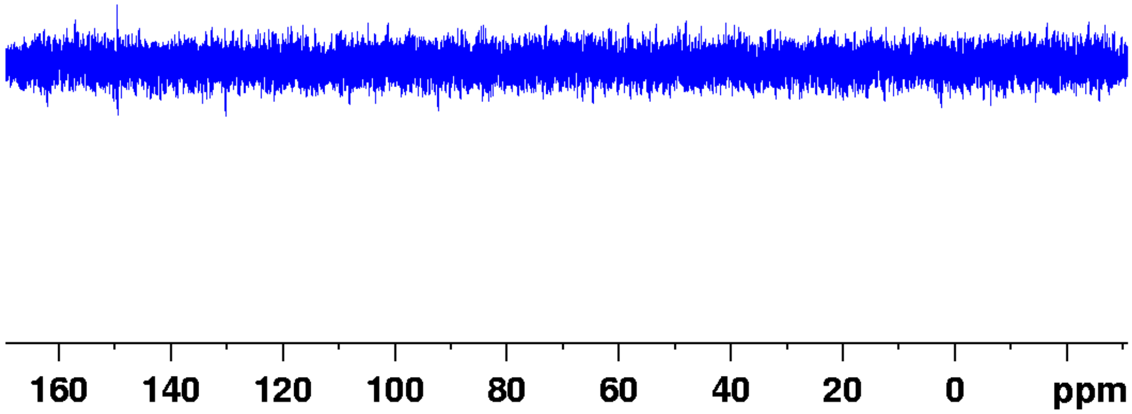

Figure 4.2. ^{31}P NMR spectrum of P-CIS nanocrystals.[71] The lack of any observable ^{31}P resonance signal demonstrates the absence of phenylphosphonic acid in the nanocrystal samples.

4.2.3 ^{14}N NMR Spectroscopy

^{14}N NMR spectroscopy was also utilized to probe the surface chemistry of the CIS quantum dots.[71] Specifically, ^{14}N NMR spectroscopy identifies the presence and potential binding of the amine in the hexadecylamine ligand which, from the ^{1}H NMR spectra, was expected to be bound to the surface of the nP-CIS and P-CIS nanocrystals. Figure 4.3 contains the ^{14}N NMR spectra of nP-CIS, P-CIS, and free hexadecylamine in toluene-d8. All three spectra contain a spurious peak at 266.4 ppm, which further investigation determined was also present in the pure toluene-d8 solvent. As such, this peak is independent and its presence has no bearing on the analysis of the quantum dot surface chemistries. Unbound hexadecylamine was found to have a broad peak at -20.82 ppm which corresponds to the amine nitrogen in hexadecylamine. The nP-CIS was found to have a broad peak at 208.47 ppm, exhibiting a large downfield chemical shift of 229.29 ppm in comparison to free un-bound hexadecylamine. This chemical shift is indicative of a change in the chemical environment for the nitrogen of hexadecylamine, which means that it is ligated through the nitrogen to the surface of the nP-CIS nanocrystals. Interestingly, no ^{14}N signal was observed for the P-CIS nanocrystals. However, the ^{1}H NMR spectra indicate that hexadecylamine is not only present but is also bound to the surface of the quantum dots. Given that the P-CIS quantum dots are partially positively charged[69] it could be expected that the chemical shift could be greater for these quantum dots. However, spectra with larger scan width windows out to 1000 ppm, well beyond the range for typical amine resonances in ^{14}N NMR spectroscopy, still yielded no observable ^{14}N resonance signal.[71] This lack of signal can be attributed to extreme peak broadening resulting from highly partially charged P-CIS and possible excess of $I = 1/2$ states due to the high cation vacancy densities within the nanocrystal matrix, which causes the peak to be broadened by such a large amount that it ‘disappears’ into and is lost in the baseline.

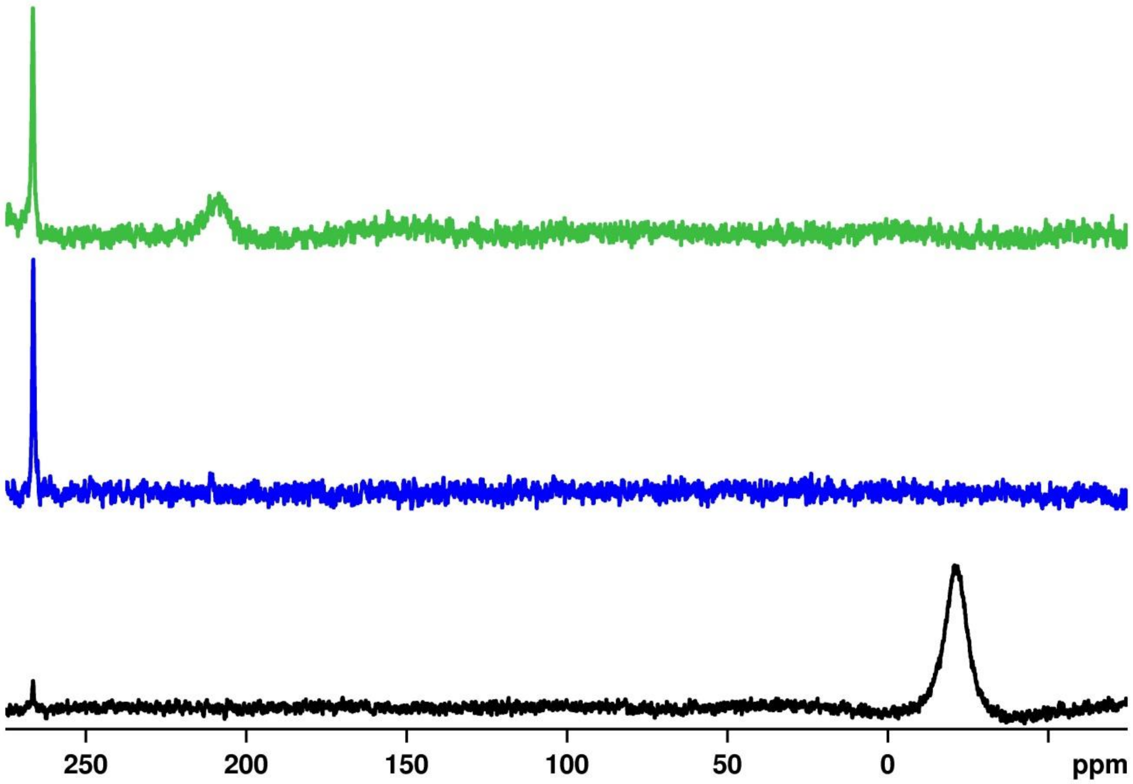

Figure 4.3. ^{14}N NMR spectra of nP-CIS (top, green), P-CIS (middle, blue) and free hexadecylamine (bottom, black).[71] The 229.29 ppm chemical shift in the nitrogen signal in the nP-CIS in comparison to the free hexadecylamine indicates that the molecule is bound to the surface of the quantum dots.[21] The lack of any observable ^{14}N signal in the P-CIS is explained by extreme peak broadening as a result of the highly partially charged P-CIS nanocrystals as well as the potential for excess of $I = 1/2$ states due to the large number of vacancy sites in the nanocrystal matrix.

4.3 Conclusion

Both non-plasmonic CIS and CIS nanocrystals that exhibit localized surface plasmon resonances were found to have the same surface chemistry.[71] ^{1}H, ^{31}P, and ^{14}N NMR spectroscopies were all utilized to verify that hexadecylamine was the only ligated surfactant bound to the surface of the CIS nanocrystals. Specifically, ^{1}H NMR indicated that hexadecylamine was present in both samples and ligated to the surface of the nanocrystals. ^{31}P NMR indicated that the phenylphosphonic acid precursor utilized in the synthesis of P-CIS was not observed to be present in the final purified samples, either in ligated or non-ligated form. Finally, ^{14}N NMR demonstrated that HDA was in fact ligated to the surface of the nP-CIS nanocrystals due to the nitrogen resonance chemical shift from that of free unbound HDA. Even though the ^{14}N signal was not observed for the P-CIS nanocrystal samples, due to the charged nature of the nanocrystal, this is not surprising. This verification of the surface chemistry of both nP-CIS and P-CIS allowed Niezgoda *et al.*[71] to conclude that the differing optical properties of the CIS nanocrystals were unrelated to the surface chemistry and therefore must be a result of the different cation stoichiometries between the nanocrystals. Specifically, the LSPR modes of P-CIS were attributed to the cation deficiency which result from cation vacancies in the nanocrystal matrix due to the fast rate of formation and growth of the P-CIS nanocrystals. These samples were later utilized to demonstrate that plasmonic nanoparticles lead to enhanced performance in quantum dot photovoltaic devices than their non-plasmonic counterparts.[71]

CHAPTER V

ELIMINATION OF HOLE-SURFACE OVERLAP IN GRADED CdS_xSe_{1-x} NANOCRYSTALS REVEALED BY ULTRAFAST FLUORESCENCE UPCONVERSION SPECTROSCOPY

Reprinted with permission from Keene, J. D.; McBride, J. R.; Orfield, N. J.; Rosenthal, S. J. Elimination of Hole-Surface Overlap in Graded CdS_xSe_{1-x} Nanocrystals Revealed By Ultrafast Fluorescence Upconversion Spectroscopy. *ACS Nano* **2014,** *8* (10), 10665-10673. Copyright 2014 American Chemical Society.

5.1 Introduction

Semiconductor nanocrystals, or quantum dots, are expansively utilized as photon sources in a wide array of applications such as light emitting diodes, biological probes, and low threshold lasers due to their (potentially) high photoluminescence quantum yields (PLQYs) and their size-dependent optoelectronic properties arising from quantum confinement.[53,72-75] As discussed in Chpater I, however, the nanocrystal surface has long been implicated as a source of trap states that localize excited charge carriers and inhibit radiative recombination of the electron and hole. Early studies yielded efforts to promote passivation of the nanocrystal surface with various organic ligands, such as hexadecylamine and trioctylphosphoine oxide, as co-surfactants to reduce the number of trap sites and moderate carrier trapping.[8,10,11] More recent work suggests that nanocrystal surface atoms are in a state of dynamic flux under excitation, resulting in an ever-changing population of surface and subsurface states available to localize charge carriers.[12,13] This revelation of a fluxional surface suggests that decoupling the exciton from the nanocrystal surface, as opposed to the long-held notion of passivating the nanocrystal surface, is essential for optimal enhancement of the photophysical properties of semiconductor nanocrystals. The obvious response to this discovery comes in the form of type-I or quasi-type-II core/shell nanocrystal heterostructures wherein a nanocrystal is encapsulated in a semiconductor shell of wider band gap to confine either both (type-I, Fig. 5.1a) or a single (quasi-type-II, Fig. 5.1b) charge carrier to the core and minimize their surface overlap.[76] Aberration-corrected atomic number scanning transmission electron microscopy (Z-STEM) was performed on CdSe/ZnS and CdSe/CdS core/shell nanocrystals and showed that complete shell coverage is necessary to achieving PLQYs near unity; however, current shell growth techniques such as successive ion layer adsorption and reaction (SILAR) yield preferential growth on anion-terminated facets.[77] Due to non-uniform faceted shell growth, upwards of 18 monolayers of material are needed for complete shell coverage, yielding large and bulky nanocrystals often exceeding 20 nm in diameter that can require days to synthesize and are not ideal in some biological imaging applications.[78] Additionally, the abrupt boundary between core and shell materials can induce strain due to lattice mismatch and introduce new trap states at the interface.[79] McBride *et al.* ultimately concluded that a graded shell is necessary for complete coverage of the semiconductor nanocrystal core.[77] The full surface coverage and passivation afforded by the graded shell, as opposed to “patchy” shells often obtained with a hard interface, is predicted to more effectively confine charge carriers away from the surface of the nanocrystal and provide optimal enhancement of the fluorescence properties.[77]

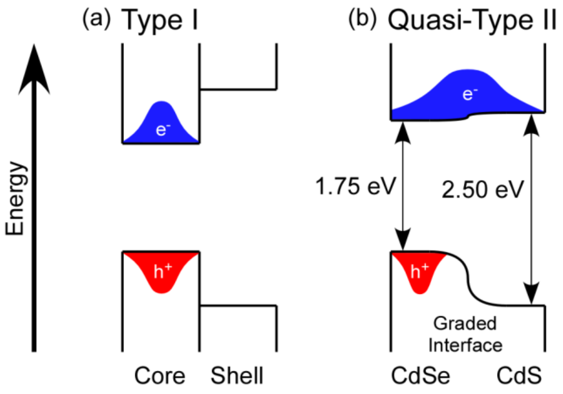

Figure 5.1. Type-I (a) and quasi-type-II (b) electronic band alignments illustrating that both carriers are confined to a single material in type-I and only a single carrier is confined in quasi-type-II.[49] Shown in (b) is the electronic band alignment between zinc blende CdSe and CdS[80] and the relaxed confinement potential afforded by a graded alloy interface between the materials.

In addition to maximum coverage with a graded shell, the gradual transition from the core to the shell materials also relaxes the confinement potential at the interface by providing an intermediate area of chemical composition which, as illustrated in Figure 5.1b, is correspondingly reflected in the band structure of the nanocrystal.[80] Investigations of graded type-I and quasi-type-II core/shell nanocrystals have established improvement over non-graded core/shell quantum dots. The relaxed confinement potential afforded by the graded shell structure and the accompanying suppression of Auger processes inhibit single nanocrystal fluorescence intermittency and improve the multiexciton performance of quantum dots.[81,82] Theory and experiment have shown the rate of nonradiative Auger recombination governs biexciton decay and is driven by the interfacial properties of the quantum dot.[80,83,84] However, the effect of the confinement potential gradient in the context of charge carrier interaction with the nanocrystal surface has been largely unexplored. Extensive ultrafast dynamics studies detailing charge carrier overlap with the nanocrystal surface of binary semiconductor nanocrystals have revealed that charge trapping at the surface is very sensitive to nanocrystal size and can be readily tuned *via* modification of the nanocrystal surface chemistry.[8,10,11,24,25,27,85] Furthermore, homogeneous CdS_xSe_{1-x} alloys were found to have trapping kinetics that were also dependent on chemical composition with charge trapping dominating the exciton decay processes as sulfur content increased.[9] Here femtosecond fluorescence upconversion spectroscopy is utilized to investigate the ultrafast dynamics of graded alloy CdS_xSe_{1-x} semiconductor nanocrystals to probe the chemical composition dependence of charge carrier trapping at the nanocrystal surface of graded alloy CdS_xSe_{1-x} nano-heterostructures.[49] We observe complete isolation of the excited hole from the nanocrystal surface and trapping kinetics that are dictated by the surface chemistry of the quantum dots.

5.2 Results and Discussion

5.2.1 Characterization

Compositionally graded alloy CdS_xSe_{1-x} nanocrystals were synthesized according to procedure developed by Harrison *et al.* based on differing reactivities of the anionic precursors.[39] These nanocrystals were thoroughly characterized in accord with techniques reported in previous literature for these particles. Optical absorption of the structural evolution of a representative compositionally graded CdS_xSe_{1-x} sample (Fig. 5.2a) reveals an initial spectrum consistent with that of CdSe nanocrystals, displays a slight red shift as the sample evolves during the synthesis, and eventually stagnates before the synthesis is terminated. Additionally, the final graded alloy CdS_xSe_{1-x} structures (Fig. 5.2b) exhibit a blue shift with an increase in sulfur composition, indicating a higher degree of quantum confinement. The size and morphology of the nanocrystals were determined *via* high resolution transmission electron microscopy (HRTEM) and, in accord with the previous reported synthesis of these nanoparticles,[39] the nanocrystals exhibit slight growth throughout the synthesis after initial core formation (Fig. 5.2c) even while S/(S+Se) ratios are observed to change. The optical and electron microscopy results can be explained by partial anion exchange of surface or near-surface selenium with the excess sulfur in the reaction mixture after growth has stopped.[38] Additionally, the final structures are similar in size for all chemical compositions (Fig. 5.2d); because the ultrafast dynamics of semiconductor nanocrystal carriers are very sensitive to size,[11] similar nanocrystal diameters permit direct comparison analyses of the carrier trapping kinetics.

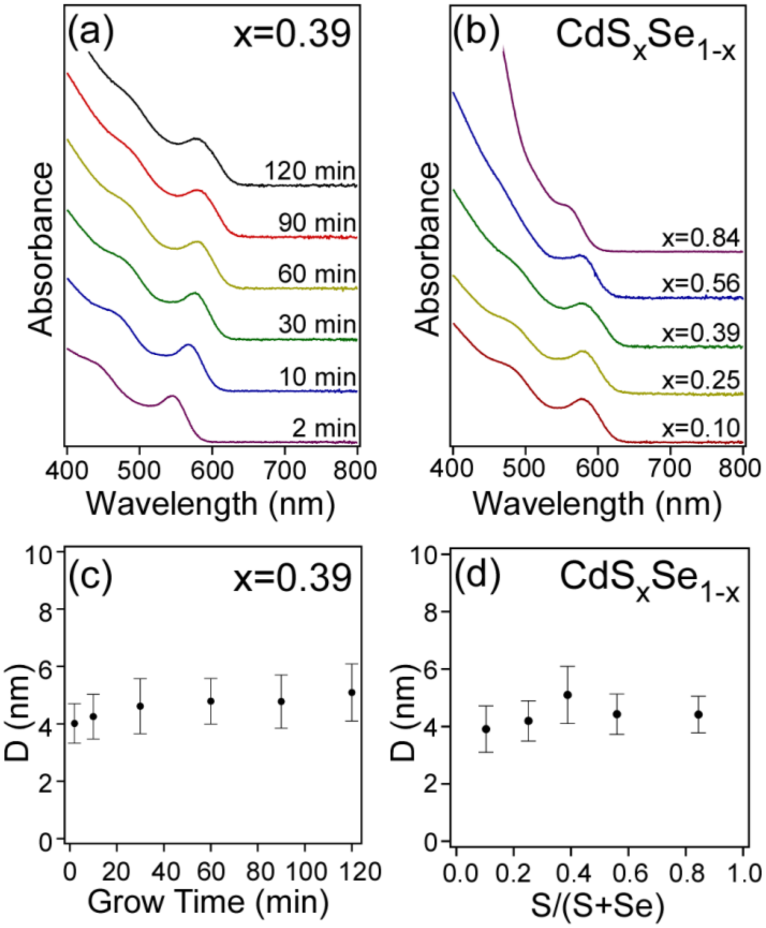

Figure 5.2. Optical absorption (a) and diameters (c) of aliquots taken during the structural evolution of $CdS_{0.39}Se_{0.61}$ (1:1 S:Se anion injection ratio).[49] Optical absorption (b) and diameters (d) of the final graded CdS_xSe_{1-x} structures (120 min aliquots). The graded alloy diameters are comparable for all samples while the blue shift in absorbance for higher sulfur compositions (b) indicates greater confinement of the charge carrier(s).

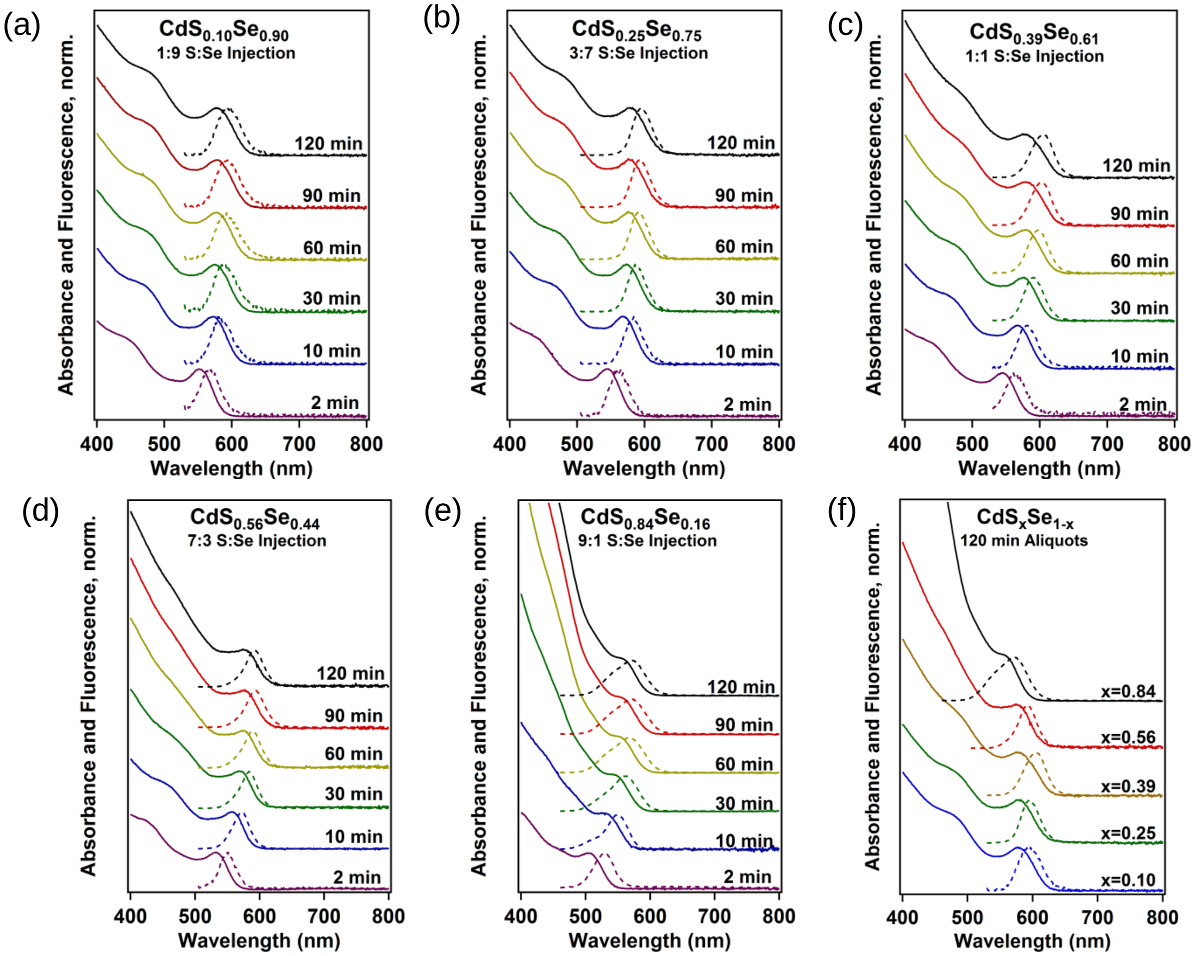

Figure 5.3. Normalized static optical absorption (solid lines) and fluorescence (dashed lines) spectra for S:Se anion injection ratios of 1:9 (a), 3:7 (b), 1:1 (c), 7:3 (d), 9:1 (e) and the final graded alloy CdS_xSe_{1-x} nanocrystals (f).

In order to determine the chemical composition of the nanocrystals, energy dispersive X-ray spectroscopy (EDS) was performed on each aliquot after rigorous purification. Figure 5.4a displays the chemical composition for a representative graded alloy synthesis and shows a nonlinear increase in sulfur composition with growth time which confirms the graded inhomogeneity of the nanocrystal structure. This is in direct contrast to homogeneous alloys which maintain constant chemical composition with growth time.[40] Additionally, the sulfur composition of the final graded structures corresponds to the initial anion injection ratios (Fig.

5.4b). The PLQY of the graded alloy nanocrystals increase with sulfur composition both as the nanocrystal structure evolves during each synthesis (Fig. 5.4c) and for the final graded alloy nanocrystals (Fig. 5.4d). PLQY values up to 65% are reported here for $CdS_{0.84}Se_{0.16}$ graded alloy nanocrystals. Finally, STEM-EDS was performed on $CdS_{0.84}Se_{0.16}$ nanocrystals for further verification of the graded alloy structure. As seen in Figure 5.7, cadmium is evenly distributed throughout the nanocrystals while the sulfur-rich shell extends beyond the selenium-rich core.

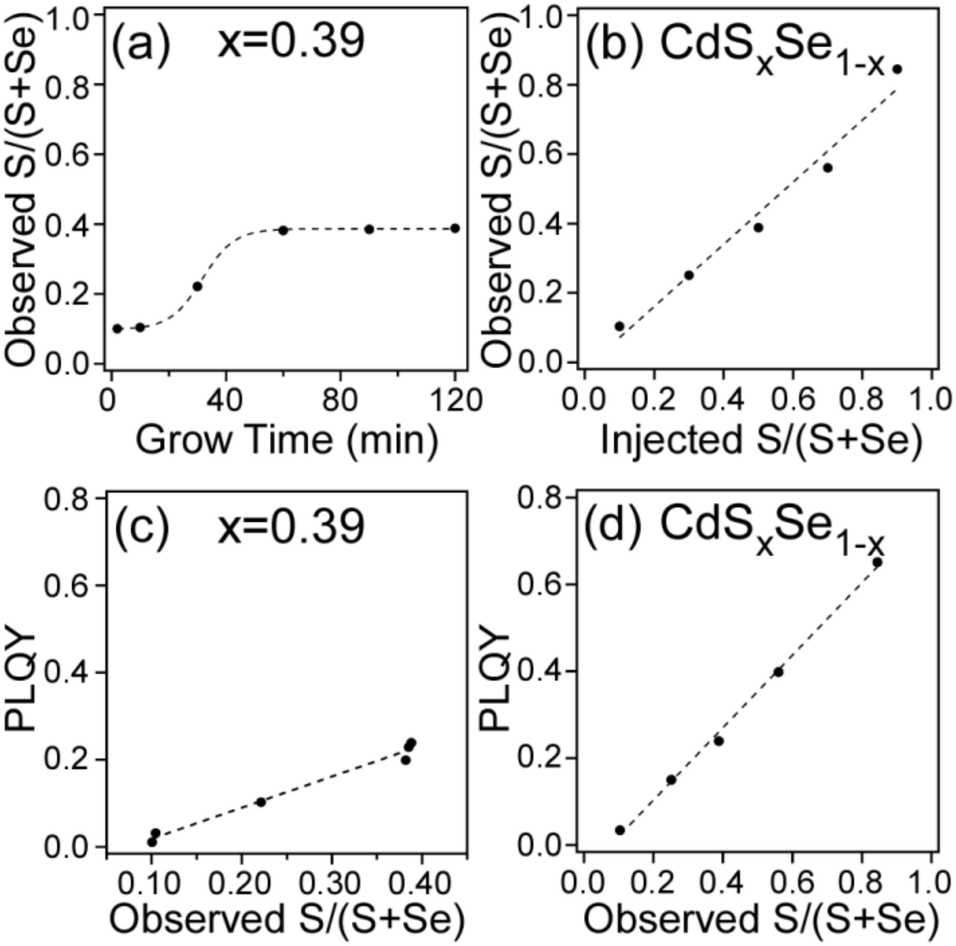

Figure 5.4. Chemical composition (a) and PLQY (c) of aliquots taken from the 1:1 S:Se anion injection synthesis. Observed *versus* injected sulfur compositions (b). The PLQY of the final graded CdS_xSe_{1-x} structures as a function of chemical composition (d).[49] The nonlinear increase in chemical composition with growth time (a) demonstrates the inhomogeneity of the sulfur incorporation into the nanocrystals. The PLQY is directly related to the chemical composition of the graded alloys (c, d).

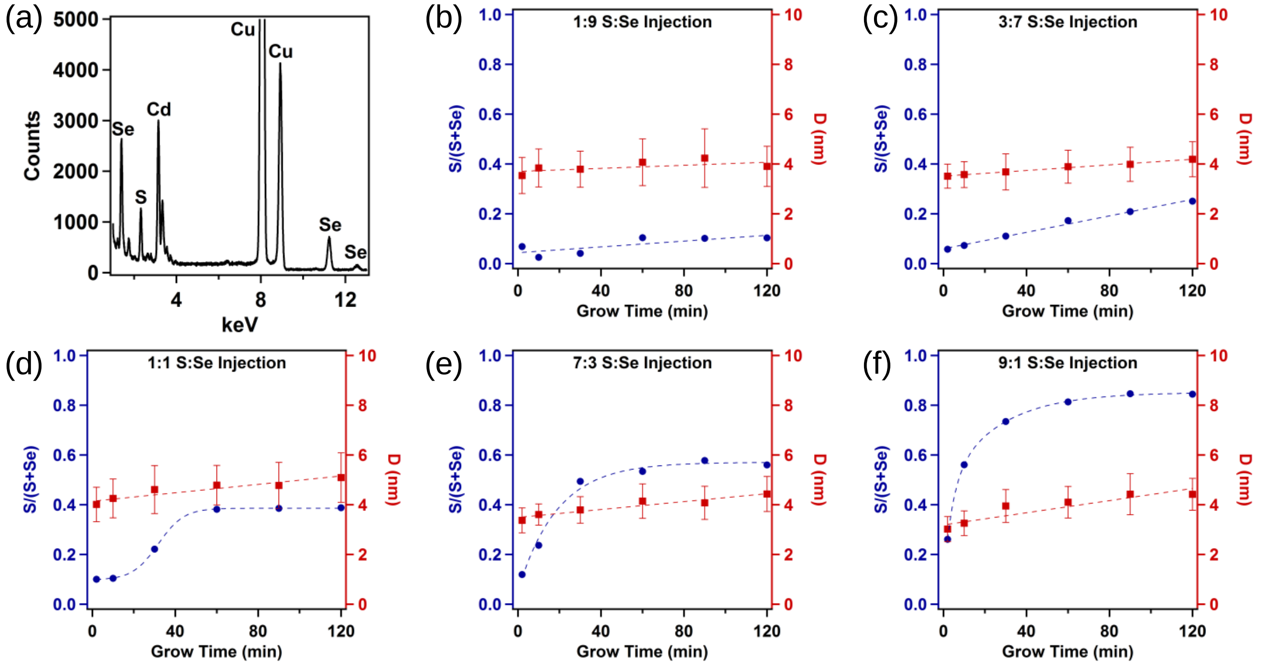

Figure 5.5. A representative EDS spectrum for $CdS_{0.39}Se_{0.61}$ (a); the Cu is background signal from the TEM grids. Measured sulfur composition (left axes, blue circles) and diameter determined by HRTEM (right axes, red squares) *versus* grow time for S:Se anion injections of 1:9 (b), 3:7 (c), 1:1 (d), 7:3 (e), and 9:1 (f).[49]

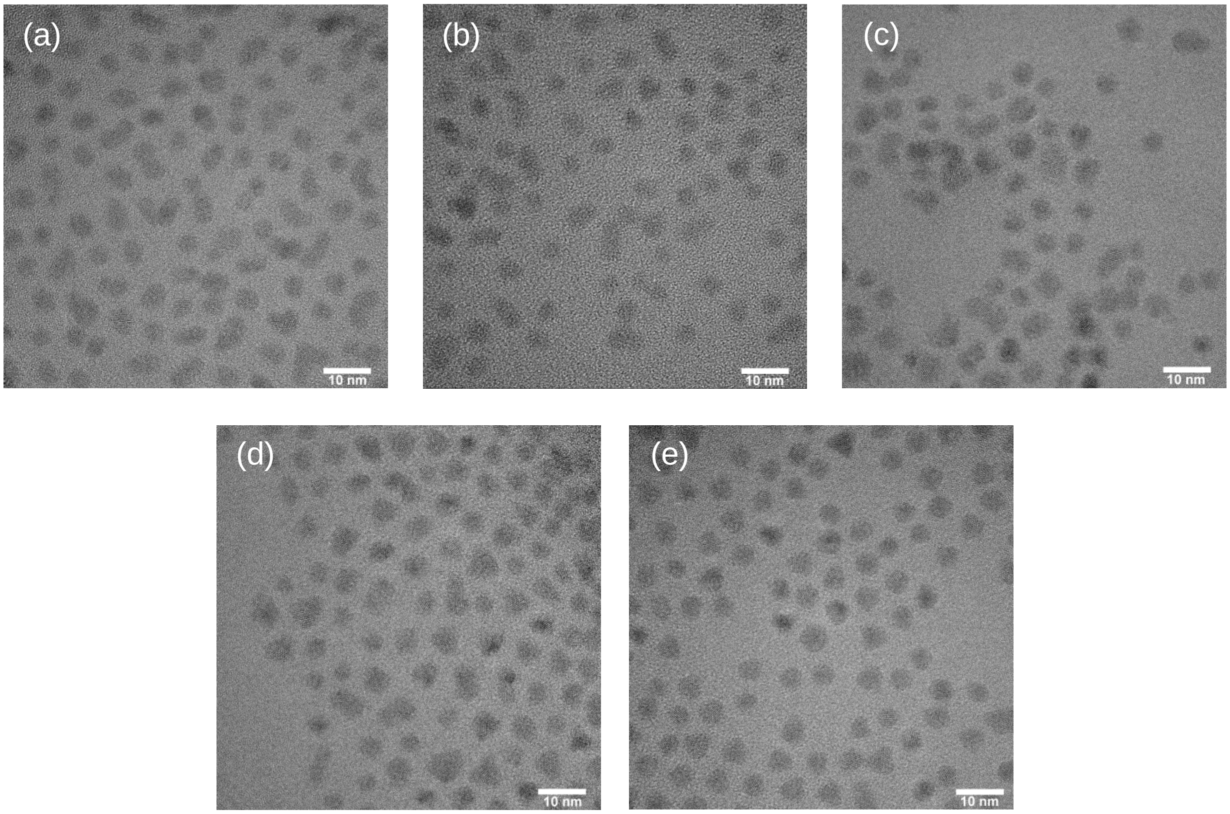

Figure 5.6. High resolution transmission electron micrographs for the final graded alloy CdS_xSe_{1-x} nanocrystal structures of $CdS_{0.10}Se_{0.90}$ (a), $CdS_{0.25}Se_{0.75}$ (b), $CdS_{0.39}Se_{0.61}$ (c), $CdS_{0.56}Se_{0.44}$ (d), $CdS_{0.84}Se_{0.16}$ (e).[49]

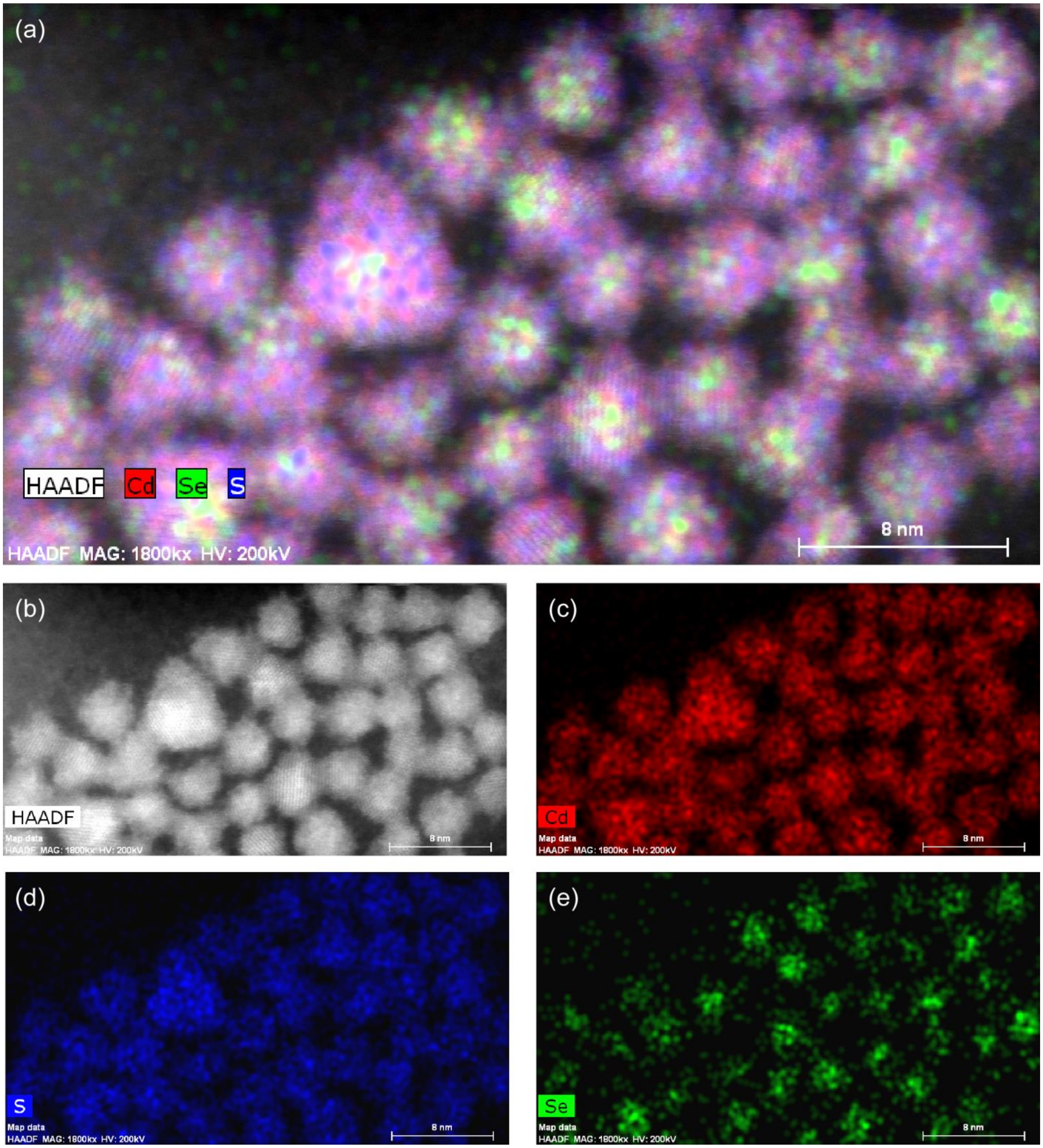

Figure 5.7. Superposition (a) of the high angle annular dark field image (b) and EDS maps of cadmium (c), sulfur (d), and selenium (e) for graded alloy $CdS_{0.84}Se_{0.16}$ nanocrystals.[49] Scale bars are 8 nm. The cadmium is evenly distributed throughout the nanocrystals while the sulfur-rich shell extends beyond the selenium-rich core.

5.2.2 Carrier Dynamics

The carrier dynamics of the graded alloy CdS_xSe_{1-x} nanocrystals were probed with femtosecond fluorescence upconversion spectroscopy. The laser system utilized in this study is described in detail in section 2.4.2. Since this technique only monitors radiative recombination of the exciton, any carrier trapping at the nanocrystal surface is realized as a decrease in the fluorescence intensity. The ultrafast fluorescence upconversion spectra for the CdS_xSe_{1-x} nanocrystals are displayed in Figure 5.8. The same trend was observed for the evolution of CdS_xSe_{1-x} nanocrystals for each S:Se anion injection ratio as for the final graded alloy CdS_xSe_{1-x} nanocrystals: an increase in sulfur composition yields a decrease in charge carrier trapping as evidenced by a less pronounced decay of the fluorescence intensity as a function of time (Fig. 5.8). Due to the similar behavior, the analysis and discussion presented in this dissertation are in regards to the final graded alloy structures (120 minute aliquots, Fig. 5.9) and the results are analogous for the structural evolution of each sample as sulfur is incorporated into the nanocrystals (Fig. 5.10). Interestingly, graded alloy CdS_xSe_{1-x} nanocrystals of low sulfur content ($S/(S+Se) < 0.34$) display triple exponential decay behavior whereas nanocrystals with higher sulfur composition exhibit double exponential decay behavior. Historically, unpassivated and under-coordinated surface anions have been implicated as mid-gap states that are available as "dangling bonds" to trap holes in CdSe nanocrystals within the first few picoseconds after excitation.[24,85] Previous work on CdS nanocrystals attribute a fast 2-3 ps decay to hole trapping at the surface based on a higher density of hole trapping states near the valence band (VB) due to its larger effective mass.[17,86] However, taking into account the recent proposal of a dynamic nanocrystal surface under excitation,[12,13] under-coordinated and unpassivated anions exist within ~1 nm of the surface of the nanocrystal due to the fluxionality of those atoms; *i.e.* instead of a crystalline, faceted lattice at the surface, the atoms are in motion and thus are not fully passivated at any given moment, increasing the likelihood of their availability to act as a hole trap. We report decay constants for the first exponential decay (τ_1) of ~3 ps (Fig 5.9a), in good agreement with the literature for hole trapping in CdSe and CdS nanocrystals. The τ_1 decay constant is consistent for all CdS_xSe_{1-x} nanocrystals; however, the first decay becomes less prevalent up to a sulfur composition of ~34%, as indicated by a decrease in τ_1 amplitude (A_1, Fig. 5.9d) at which point the decay completely disappears from the ultrafast fluorescence upconversion data. This is direct evidence for the quasi-type-II band structure alignment created by the CdS-rich shell encapsulating the CdSe-rich core which, based on the VB offset between the materials, functions as a "hole well" in which the hole is confined to the core of the nanocrystal heterostructure. Elimination of the fast hole-trapping process from the carrier dynamics demonstrates successful separation of the hole from within ~1 nm of the nanocrystal surface and confirms the proposed graded alloy structure. A schematic illustrating the gradient in chemical composition, overlay of the corresponding energy level diagram, the resulting electron and hole probability densities, and the elimination of hole trapping is provided in figure 5.11.

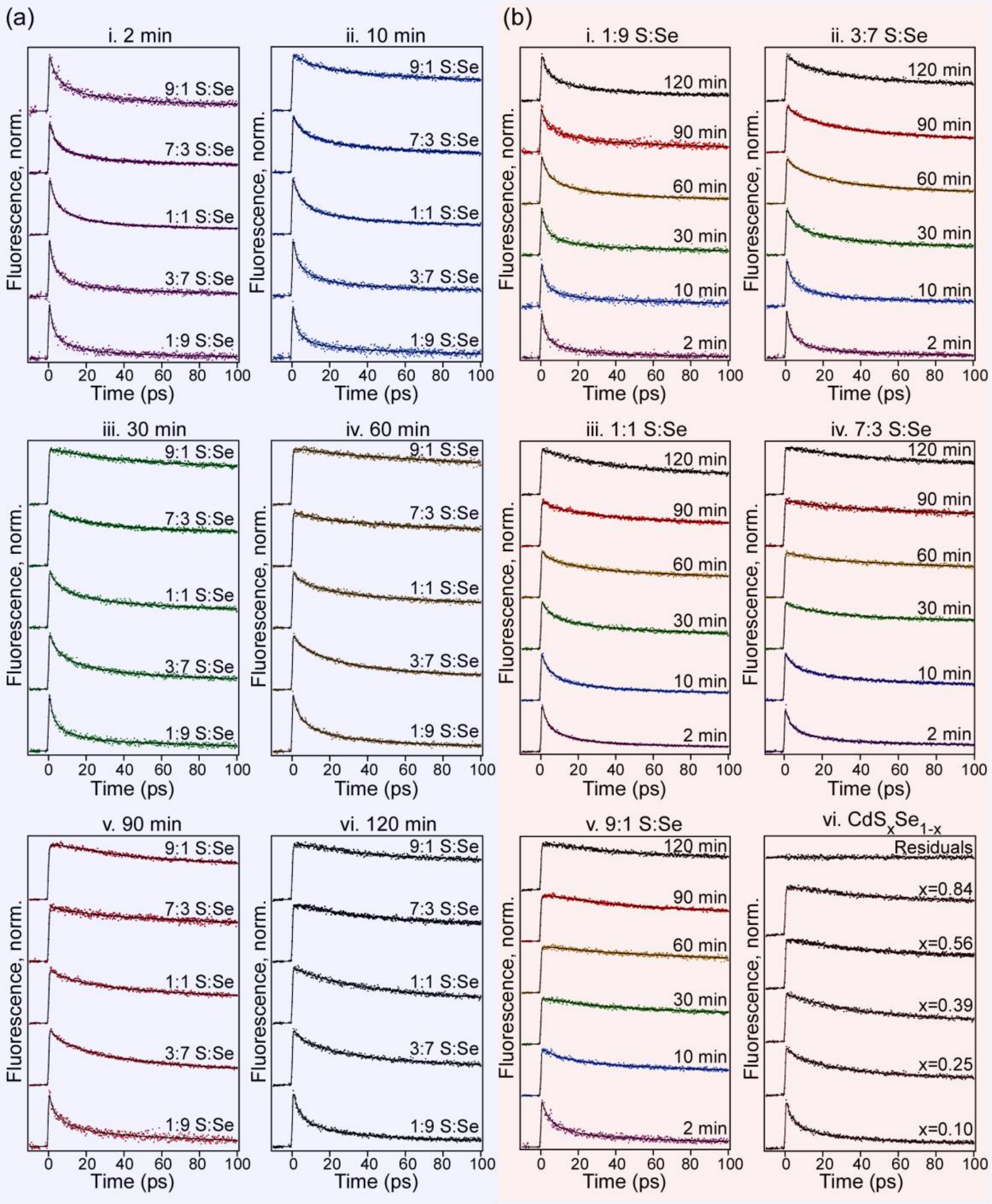

Figure 5.8. Ultrafast fluorescence upconversion spectra of graded alloy CdS$_x$Se$_{1-x}$ nanocrystals.[49] Carrier trapping is observed indirectly as a fast decay of the fluorescence intensity. The spectra are plotted according to (a) reaction time points and (b) S:Se injection ratios to show the reduced trapping as sulfur is more quickly incorporated into the alloys with higher S:Se injection ratios and as the graded alloy nanocrystal structures evolve during each S:Se injection ratio synthesis, respectively. The top trace in (b-vi) is the plotted residuals for graded CdS$_{0.25}$Se$_{0.75}$ nanocrystals (x=0.25) and is representative of all fits. All samples were excited at 50 nm above band gap and observed at the wavelength corresponding to maximum fluorescence intensity.

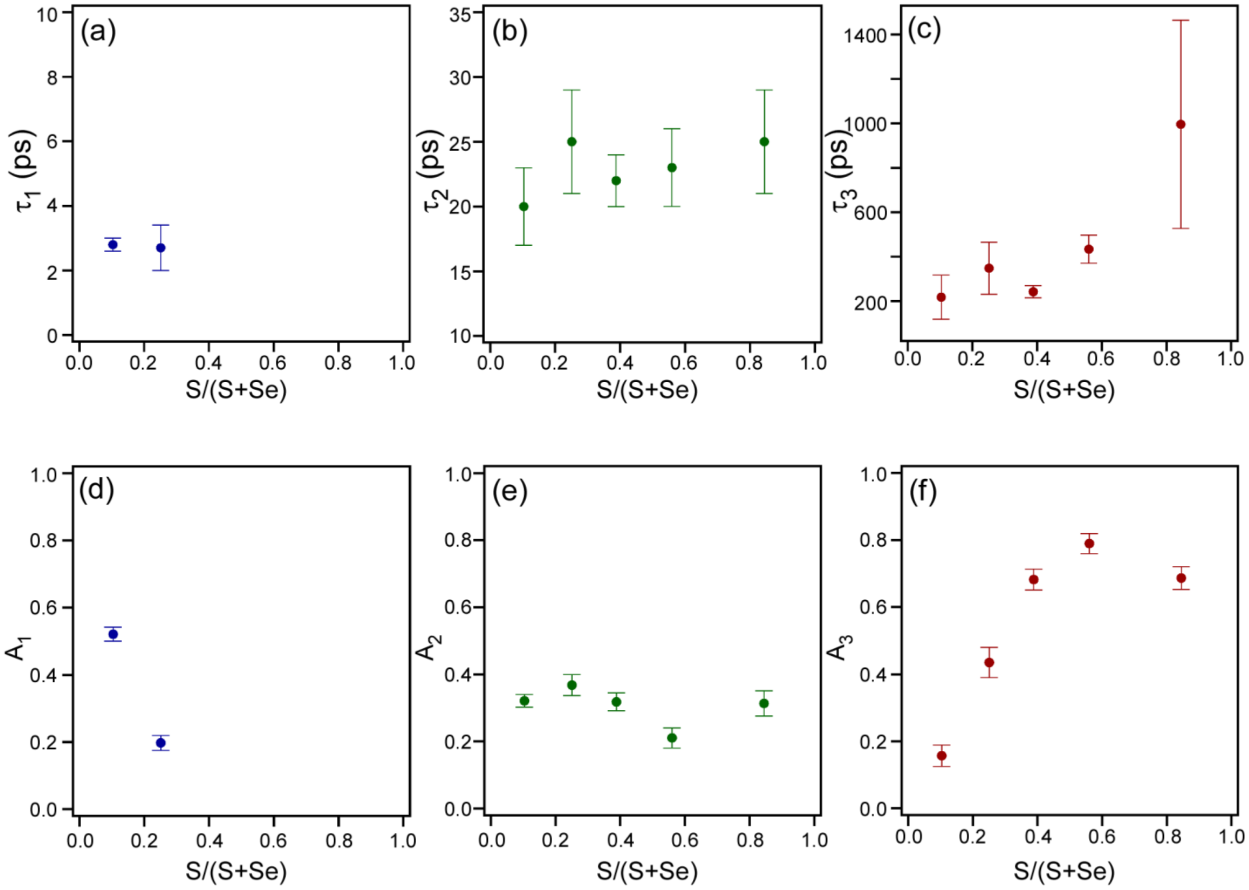

Figure 5.9. Exponential decay constants τ_1 (a), τ_2 (b), and τ_3 (c) and the corresponding amplitudes A_1 (d), A_2 (e), and A_3 (f) for the final graded CdS_xSe_{1-x} nanocrystals as a function of sulfur composition.[49] As sulfur composition increases: hole trapping (τ_1) is eliminated, the electron trapping decay constant (τ_2) increases, and exciton lifetime decay constant (τ_3) increases, all indicative of reduced carrier interaction (trapping) with (at) the nanocrystal surface.

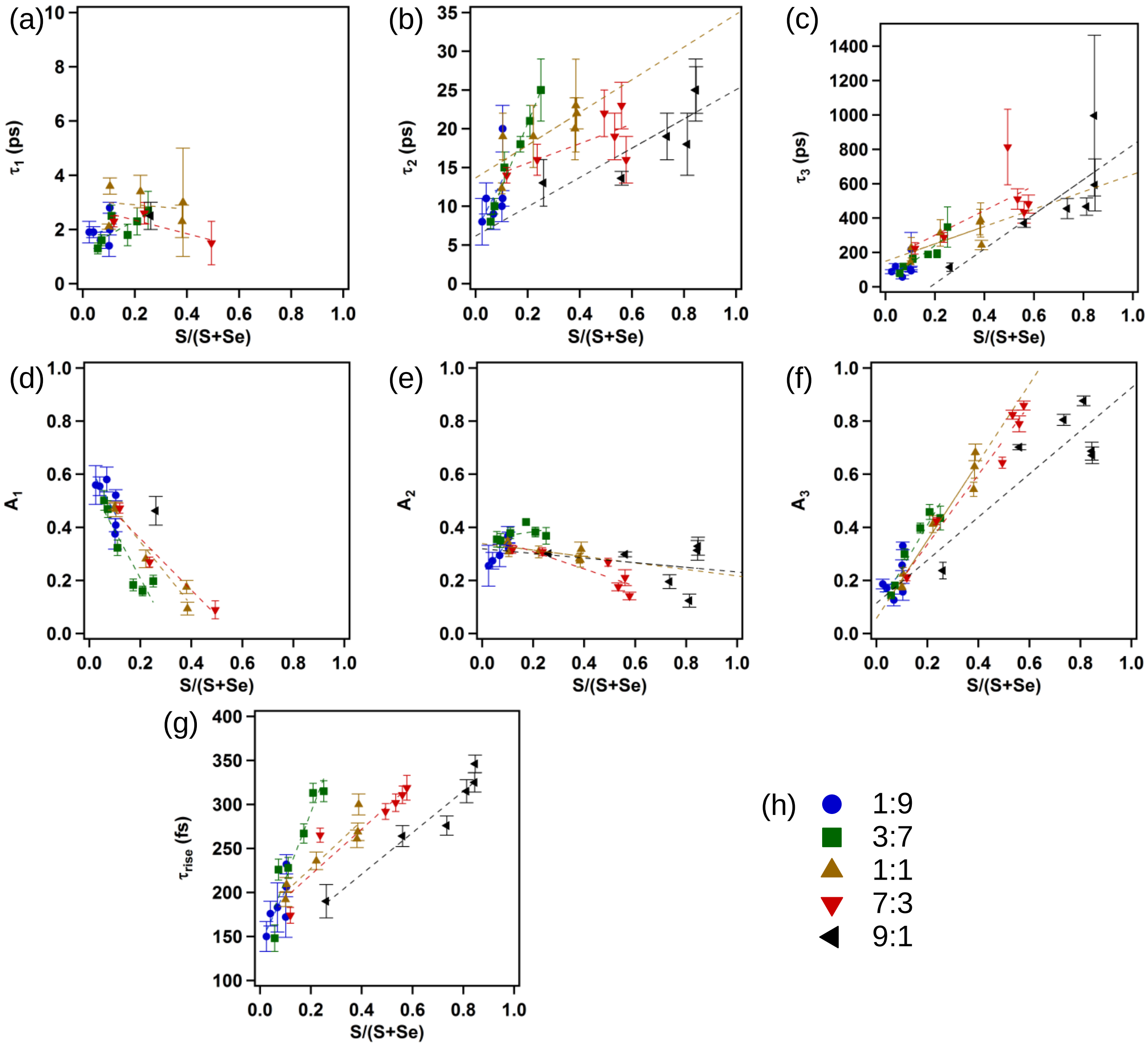

Figure 5.10. Plots of τ_1 (a), τ_2 (b), τ_3 (c) decay constants and the corresponding amplitudes A_1 (d), A_2 (e), A_3 (f) for the structural evolution of each S:Se injection ratio as indicated by (h). Plot of rise time (g) determined by fitting the fluorescence upconversion spectra with an addition decay of negative amplitude. Lines are added to illustrate the observed trends. Legend of S:Se anion injection ratios (h).[49]

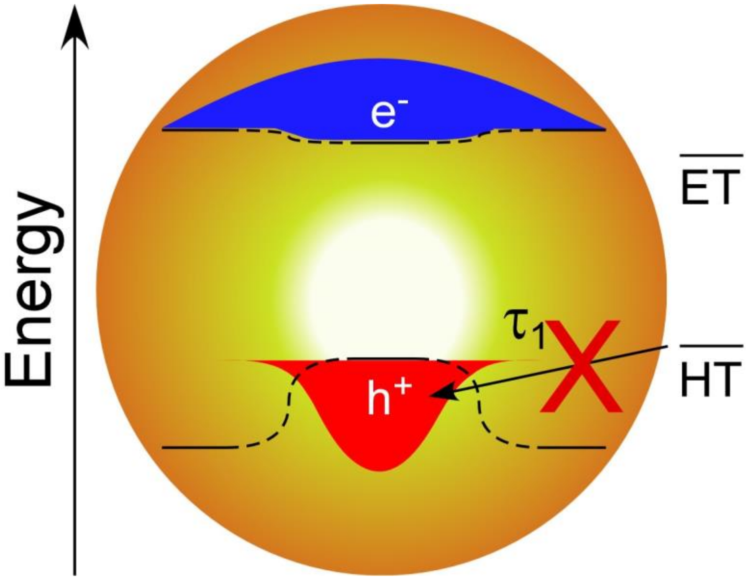

Figure 5.11. Graphic illustrating the gradient in chemical composition, overlay of the corresponding energy level diagram, and the resulting electron and hole probability densities. The confinement of the hole away from the surface is validated by the disappearance of the short 1-3 ps time decay (τ_1) in the ultrafast fluorescence decay spectra.

The second exponential decay process in the graded alloy CdS_xSe_{1-x} nanocrystals was found to have a decay constant of 20-25 ps, increasing with sulfur composition (τ_2, Fig. 5.9b). Electron trapping in CdSe nanocrystals is a process that occurs 10's to 100's of picoseconds after excitation[24,85] and has been reported as a 20-30 ps decay in CdS nanocrystals.[17,86] Our results for τ_2 are in good agreement with the reported literature values for electron trapping in CdSe and CdS nanocrystals. This supports the quasi-type-II band structure of the graded alloy CdS_xSe_{1-x} nanocrystals in which the excess electron energy in the conduction band (CB) is greater than the confinement potential of the CB offset of only ~0-0.1 eV between the CdSe-rich core and the CdS-rich shell.[80,87] Therefore, the electron is delocalized throughout both the core and shell materials and maintains access to the nanocrystal surface for all sulfur compositions, as illustrated in figure 5.12. Indeed, the 20-25 ps electron trapping is present in all CdS_xSe_{1-x}

nanocrystals regardless of sulfur composition. Traditionally, the surface of nanocrystals has been envisioned as a static crystalline interface that may contain cadmium ad-atoms and/or cadmium atoms that are not fully coordinated or passivated and therefore are available to trap electrons. However, once again taking into account the recent proposal of a fluxional nanocrystal surface under excitation, the atoms within ~1 nm of the surface are physically in motion at any given moment as part of a dynamic non-crystalline "lattice" at the nanocrystal-surface interface; thus, there exists an ever-changing population of cadmium atoms that, similar to what has been proposed for the static surface, are potentially under-coordinated and therefore are available as electron trap states.

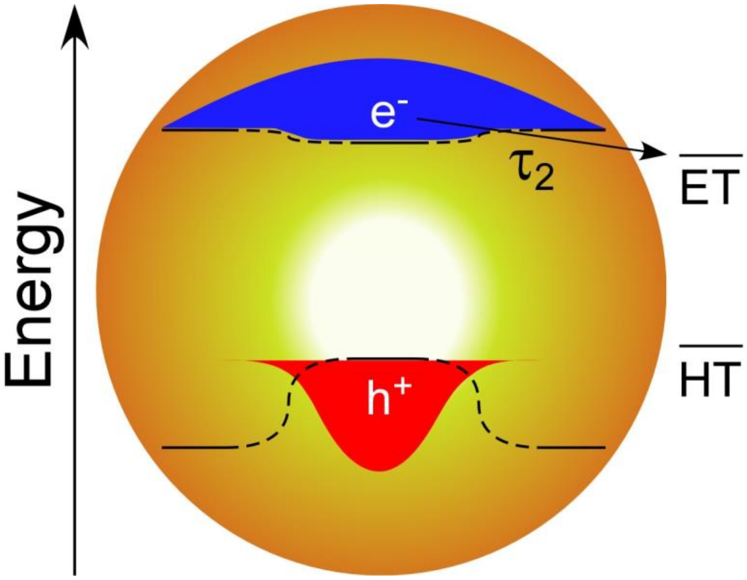

Figure 5.12. Graphic illustrating the gradient in chemical composition, overlay of the corresponding energy level diagram, and the resulting electron and hole probability densities. The negligible conduction band offset between the core and shell materials is validated by the constant medium 20-30 ps time decay (τ_2) in the ultrafast fluorescence decay spectra for all chemical compositions.

In addition to surface considerations, the mobility of the charge carriers in the different core and shell dielectric media must also be taken into account because the electrons must delocalize through the core and shell materials in order to access the nanocrystal surface. In the graded alloy CdS_xSe_{1-x} nanocrystals there is a radial variation in electron mobility directly related to the chemical composition. For inorganic semiconductors, the electron mobility (μ_n) is inversely proportional to the effective mass of the electron (m_n^*) and varies as ${m_n^*}^{-5/2}$.[88] Therefore, the ratio of the electron mobility of CdS to CdSe can be determined according to:

$$\frac{\mu_{n\,[CdS]}}{\mu_{n\,[CdSe]}} \propto \left(\frac{m^*_{n\,[CdSe]}}{m^*_{n\,[CdS]}}\right)^{5/2} \tag{5.1}$$

For electron effective mass values of $0.17m_0$ in CdS and $0.13m_0$ in CdSe,[89] where m_0 is the free electron rest mass, we calculate the ratio of the electron mobility of CdS to CdSe to have a value of 0.51. Thus, the electron mobility gradually decreases by about half as the shell increases in sulfur composition, delaying charge carrier access to the nanocrystal surface and extending τ_2 lifetimes. While the differences in carrier mobility between the CdSe-rich core and CdS-rich shell materials are not expected to be the rate-limited factor at these diameters (<5 nm) and time scales (fs-ps), it cannot be ignored and must be acknowledged as a potential contributing factor.

Finally, the third exponential decay process corresponds to radiative relaxation of the exciton. Excited electron-hole pair recombination in semiconductor nanocrystals is a nanosecond process[24,85] and extends beyond the capabilities of our upconversion experiment (100 ps). Therefore, the τ_3 time constants reported from our analysis of the ultrafast fluorescence decay curves do not represent actual measured lifetime values for the radiative relaxation of the exciton; however, they allow our model to decay to baseline as determined by y_0 before the excitation pulse arrives.[90,91] Nevertheless, a clear trend of an increase in τ_3 is observed as sulfur content increases (Fig. 5.9c), indicating longer lifetimes. Notably, the first and third decay amplitudes are inversely related; as the first decay disappears, the third decay increases and begins to dominate the exciton decay processes (Figs. 5.9d and 5.9f). This is exactly the opposite behavior than is reported for the charge carrier dynamics of homogeneous alloy CdS_xSe_{1-x} nanocrystals where the first decay amplitude increases and carrier trapping begins to dominate with an increase in sulfur composition.[9] These findings afford further validation of the inhomogeneous chemical composition of the graded alloy CdS_xSe_{1-x} nanocrystals.

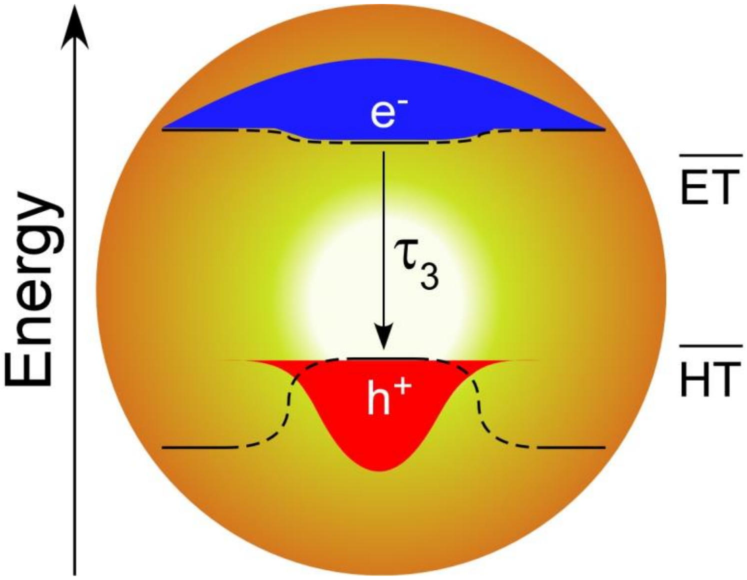

Figure 5.13. Graphic illustrating the gradient in chemical composition, overlay of the corresponding energy level diagram, and the resulting electron and hole probability densities. The third decay corresponds to radiative relaxation of the exciton and extends beyond the instrument capability.

By focusing on the first few picoseconds after the arrival of the excitation pulse we also investigated the initial population of the band edge radiative states, $1S_{3/2}$ and $1S_e$ for the VB and

CB, respectively.[92] Figure 5.14a displays a representative fluorescence upconversion spectrum of a CdS_xSe_{1-x} sample as the pulse arrives and an electron is promoted from the VB to the CB. The data were fit with an additional exponential decay, albeit with a negative amplitude, in order to determine if a rise time (τ_{rise}) is present. Since only the band edge radiative recombination is observed in these experiments, a rise time represents the temporal delay between excitation of the charge carriers and the onset of emission by the nanocrystal. Since we excited the samples 50 nm above the band gap, the $1S_e$ state in the CB was initially populated with an electron from the $2S_{3/2}$ state in the VB.[2,93] Therefore, the hole in the $2S_{3/2}$ state must undergo intraband cooling/relaxation to the $1S_{3/2}$ state before band edge radiative recombination can occur; this delay is realized as a rise time in the temporal fluorescence upconversion spectra. As seen in Figure 5.14b the observed rise times are at or slightly longer than the pulse width, which defines the temporal resolution of the experiment, and are consistent with values reported for intraband hole cooling in CdSe nanocrystals.[11,94] There is a slight additional rise of 8-10 ps for the highest sulfur compositions ($S/(S+Se)>0.5$) and additional studies are recommended to probe the excitation- and emission-dependent dynamics of the graded alloy $CdS_{0.84}Se_{0.16}$ nanocrystals. These studies on the graded structure with the highest sulfur content that most prominently exhibits quasi-type-II behavior are expected to provide additional insight into the relationship between the core/shell interface and the surface interaction of excited charge carriers.

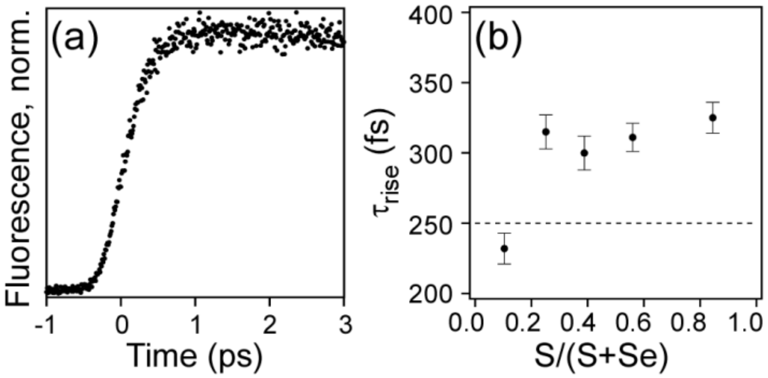

Figure 5.14. Ultrafast fluorescence upconversion spectrum of $CdS_{0.39}Se_{0.61}$ (a) and observed rise times (τ_{rise}) as a function of sulfur composition (b).[49] Sub-picosecond rise times exhibit a slight increase with sulfur composition and correspond to hot hole cooling in the valence band. The sample was excited at 50 nm above band gap (530 nm) and observed at the maximum fluorescence intensity (604 nm). Note: The dotted line in (b) indicates the instrument resolution.

These results and analyses of the ultrafast dynamics of graded alloy CdS_xSe_{1-x} nanocrystals highlight the importance of charge carrier interaction with the surface of semiconductor nanocrystals. However, the carrier dynamics also show a clear structural chemical composition dependence that affects the *magnitude* of trapping and can even eliminate carrier (hole) overlap with the nanocrystal surface through proper electronic band gap engineering of the core and shell materials. This is evidenced by the disappearance of hole trapping in graded alloy CdS_xSe_{1-x} as sulfur is incorporated into the structure and the VB offset becomes great enough to confine the hole to the core of the nanocrystal and eliminate the interaction of the hole with the surface. However, for any charge carriers that do overlap with the nanocrystal surface it is clear that the chemical composition of the nanocrystal surface, as opposed to the internal nanocrystal architecture, is what determines the *behavior* of the charge carrier trapping. Even though the graded alloy CdS_xSe_{1-x} nanocrystals have predominantly CdSe-rich cores, the ultrafast carrier trapping processes most closely resemble those of charge carriers in CdS nanocrystals which exhibit fast 2-3 ps hole trapping and longer 20-30 ps electron trapping kinetics, because the surface composition of the nanocrystals most closely resembles CdS. Notably, it is this interplay between the internal structure and the chemical composition of the surface that ultimately determines the fate of the exciton in quantum confined nanostructures.

5.3 Conclusion

Graded alloy CdS_xSe_{1-x} nanocrystal were synthesized by tuning precursor reactivity. The graded alloy structure was characterized and verified using UV-vis absorption and fluorescence spectroscopy, PLQYs, HRTEM, Z-STEM, EDS, and STEM-EDS. Direct time-resolved spectroscopic evidence was presented for quasi-type-II band alignment in graded alloy CdS_xSe_{1-x} nanocrystals through analysis of the ultrafast charge carrier dynamics as a function of chemical composition. The fast ~3 ps hole trapping process disappears as sulfur composition increases to form a graded CdS-rich shell with VB offset such that excited holes are confined to the CdSe-rich core. These results demonstrate that charge (hole) carrier interaction with the surface can be completely eliminated in nanocrystal structures with dimensions less than 5 nm, a phenomenon that typically requires a “giant” core/shell heterostructure. The 20-25 ps electron trapping is consistent in amplitude throughout all sulfur compositions in the graded alloy CdS_xSe_{1-x} nanocrystals, with a slight increase in τ_2 decay constant with sulfur composition. Our findings demonstrate progress towards highly efficient nanocrystal fluorophores that are independent of their surface chemistry to enable their incorporation into a diverse range of applications without experiencing adverse effects arising from dissimilar environments.

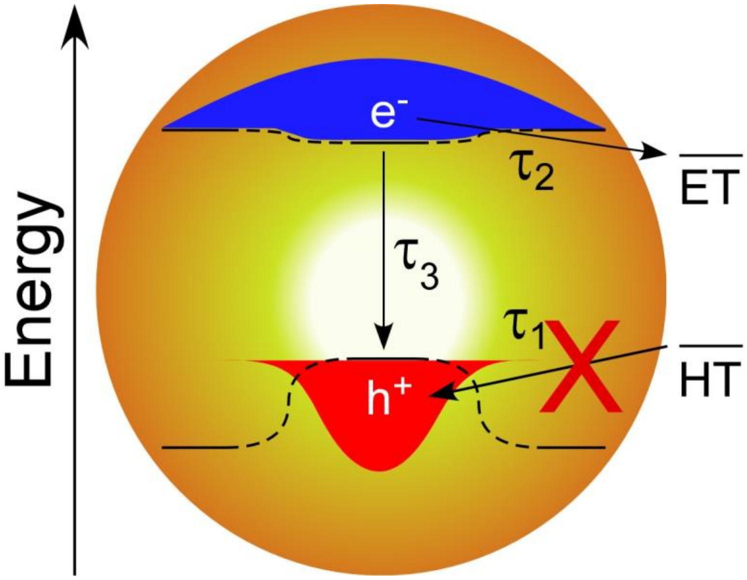

Figure 5.15. Graphic illustrating the gradient in chemical composition, overlay of the corresponding energy level diagram, and the resulting electron and hole probability densities.[49] The 1-3 ps hole trapping decay (τ_1) disappears with an increase in sulfur composition and exaggerated valence band offset. The negligible conduction band offset is validated as the 20-30 ps electron trapping decay (τ_2) retains a relatively constant amplitude (A_2) for all chemical compositions. The third decay(τ_3) corresponds to radiative relaxation of the exciton and extends beyond the instrument capability.

CHAPTER VI

CONCLUSIONS AND FUTURE DIRECTIONS

6.1 Overall Conclusions

^{1}H, ^{31}P, and ^{14}N nuclear magnetic resonance spectroscopy (1-D) were demonstrated to be simple yet effective characterization techniques for investigation of the surface chemistry and ligands of semiconductor nanocrystal quantum dots. The development of protocol to ligate pyridyl-P3HT ligands to the surface of CdSe nanocrystals and the subsequent investigations into the binding motif of the functionalized semiconductor polymer to the nanocrystals demonstrated that pyridyl-P3HT ligates to the nanocrystals through the nitrogen of the pyridine end-functional group; this differs from the binding scheme of free pyridine molecules to CdSe nanocrystals. The ligation of P3HT to CdSe nanocrystals allowed for demonstration by Kochemba *et al.* that pyridyl-P3HT-CdSe nanocrystals exhibited superior dispersion in annealed P3HT/CdSe blend films than non-polymer-ligated CdSe nanocrystals.[61,62] This provides a new route to modify and control the morphology of the active layer of nanocrystal/polymer QDPVs in the quest enhance QDPV performance.

Analysis of the surface ligands of plasmonic and non-plasmonic $Cu_xIn_yS_2$ semiconductor nanocrystals revealed the presence and binding of only hexadecylamine to the surface of the nanocrystals. This allowed for the conclusion that the LSPR modes in the $Cu_xIn_yS_2$ nanocrystals arise from the cation deficiency in the plasmonic particles. Also, the verification of the "twin" $Cu_xIn_yS_2$ particles that differed only in cation stoichiometry (and LSPR modes) allowed for a direct comparison of QDPV devices by Niezgoda *et al.* which demonstrated that the overlap between the band gap and plasmonic absorption is advantageous in that it increases efficiencies of QDPVs.[71]

Finally, comprehensive structural characterization of graded alloy CdS_xSe_{1-x} nanocrystals verified their inhomogeneous, radial variation in chemical composition. Analysis of the femtosecond charge carrier dynamics of the graded alloy CdS_xSe_{1-x} nanocrystals verified the quasi-type-II band alignment of the nano-heterostructures through the elimination of hole trapping at the nanocrystal surface driven by the VB offset between the CdSe-rich core and the CdS-rich shell. It was demonstrated that excited charge carrier interaction with the surface can be completely eliminated in nanocrystal structures with dimensions less than 5 nm, a phenomenon that typically requires a "giant" core/shell heterostructure. It was demonstrated that chemical composition dependence dictates the *magnitude* of carrier-surface overlap whereas the surface chemistry drives the *behavior* of the carrier-surface interaction. These results demonstrate progress towards highly efficient nanocrystal fluorophores that are independent of their surface chemistry. Such nanostructures would ultimately enable their incorporation into a diverse range of applications without experiencing adverse effects arising from dissimilar environments.

6.2 Future Directions

A more complete understanding of the excited state of semiconductor nanocrystal quantum dots and the methods by which we can exhibit control of the behavior of the charge carriers will promote rational design of these materials to exhibit the desired properties for a wide array of applications such as solid state lighting, solar concentrators, lasers, biological probes, and photovoltaic devices. Achieving ligated P3HT-CdSe nanocrystal heterostructures in significant purified quantities will allow for study of the ultrafast charge carrier dynamics and observation of the hole transfer from CdSe nanocrystals to the polymer ligand and/or electron transfer from polymer ligand to CdSe nanocrystal. This direct interrogation of the charge transfer process that is already widely utilized in CdSe-P3HT polymer blend devices could be achieved in an extension of the efforts presented in this work through choice of P3HT functional groups that have a higher affinity for CdSe. Two ideal candidates would be phosphonic acid and carboxylic acid functionalized P3HT because it has been shown that both of these groups more strongly associate with the CdSe nanocrystal surface than pyridine.[60,95] A potential mitigating factor for this approach, however, is that this charge transfer process effectively quenches the fluorescence of the polymer-ligated nanocrystals.[60] Since fluorescence upconversion spectroscopy observes a sample's fluorescence, if the fluorescence is completely quenched by the charge transfer driven by the type-II band offset between the nanocrystal and ligand, other spectroscopic techniques such as transient absorption spectroscopy may be necessary to probe the carrier dynamics of the system.

Control over the excited state of the graded alloy CdS_xSe_{1-x} nanocrystals in this work was limited to one charge carrier; namely, the hole was confined to the core and away from the surface due to the valence band offset between the CdSe-rich core and the CdS-rich shell of the nano-heterostructure. Enhancement of the optical properties, however, was still impressive with photoluminescence quantum yields up to 65.1% reported for $CdS_{0.74}Se_{0.16}$ graded alloy nanocrystals with diameters less than 5 nm. Typically, enhancement of this magnitude requires large shell materials with diameters approaching or exceeding 20 nm. Bawendi and coworkers have recently reported very high photoluminescence quantum yields of >90% with core/shell structures with total diameters of ~10 nm by utilizing a carefully controlled shelling procedure on high quality nanocrystal core seeds.[96] An approach to further enhance the optical properties of graded alloy nanocrystals while still maintaining small <5 nm particle diameters would be to modify the alloy materials to form a type-I core/shell graded alloy structure that would confine both charge carriers away from the surface. This can be accomplished by addition of a low-reactivity zinc precursor to the current graded alloy CdS_xSe_{1-x} nanocrystal synthesis in order to form a $Cd_xZn_{1-x}S_ySe_{1-y}$ structure with a CdSe-rich core that gradually transitions to a ZnS shell material. This type-I structure has been demonstrated to effectively confine both charge carriers to the core of CdSe nanocrystals in structures with large ZnS shells.[79] The confinement efficacy of both charge carriers will again be apparent in the optical properties with enhanced photoluminescence quantum yields potentially approaching unity. Analysis of the carrier dynamics observed by femtosecond fluorescence upconversion spectroscopy would yield the degree to which the charge carriers are isolated from the nanocrystal surface in the relative contribution of the decays to the overall relaxation as indicated by the amplitudes of the electron and hole decays. Ultimate success will be verified by complete elimination of electron and hole trapping at the nanocrystal surface as indicated by a single-exponential decay corresponding only to the radiative recombination of the excited charge carriers.

APPENDIX A

LOW-TEMPERATURE SYNTHESIS OF CdSe NANOCRYSTALS

In an effort to establish direct growth of P3HT-functionalized CdSe nanocrystals, low-temperature synthesis of CdSe nanocrystals was investigated. Low temperatures were needed in order to prevent decomposition of the P3HT polymer during the synthesis.[97] Oleylamine, a fatty amine, was used as the representative surfactant in the syntheses because it binds to CdSe through nitrogen, similar to what was found for the pyridine-functionalized polymers. Several different precursor combinations were used to synthesize CdSe nanocrystals at low temperatures: cadmium precursors included cadmium acetate dihydrate ($Cd(Ac)_2 \cdot 2H_2O$) and Cd-dodecylphosphonate; selenium precursors included various concentrations of Se:tributylphosphine (Se:TBP) and Se:1-octadecene (Se:ODE).

Magic-size CdSe nanocrystals, or CdSe nanoclusters, were readily formed at 80°C with all precursor combinations. However, there was some difficulty in growing the nanocrystals larger than clusters at low temperature. $Cd(Ac)_2 \cdot 2H_2O$ and Se:TBP was the only combination of precursors that yielded larger CdSe beyond magic-size at 80°C. The maximum size attainable at 80°C had an absorption maximum at 476 nm, corresponding to a diameter of 2.1 nm (Fig. A.1a). Increasing the temperature to 130°C yielded nanocrystals with an absorption maximum at 540 nm, with a diameter 2.8 nm (Fig. A.1b).

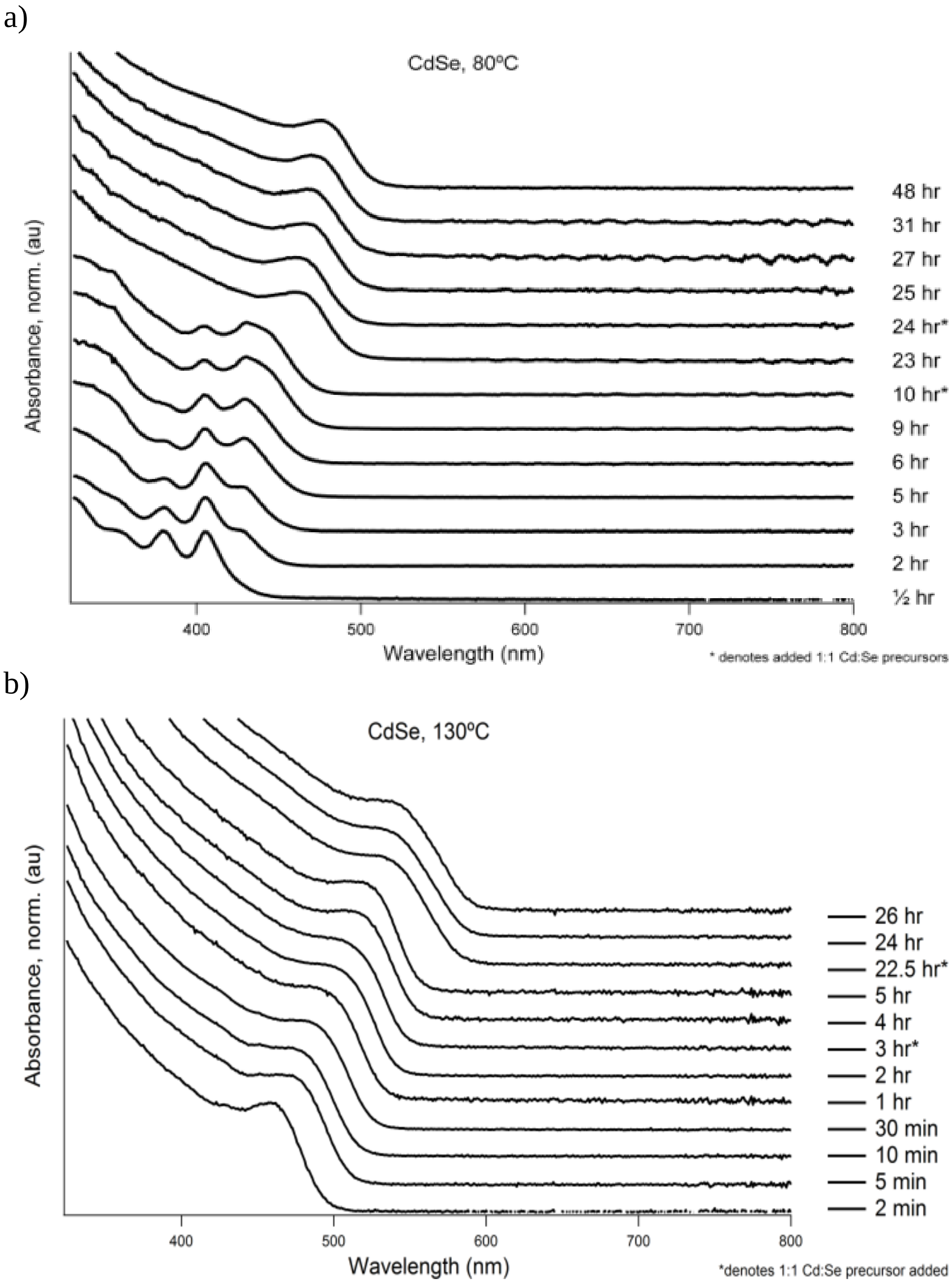

Figure A.1. Absorbance spectra of CdSe growth at 80°C (a) and 130°C (b) using $Cd(Ac)_2{\cdot}2H_2O$ and 0.2 M Se:TBP precursors.

APPENDIX B

MODIFICATIONS TO THE ULTRAFAST FLUORESCENCE UPCONVERSION SETUP

B.1 Addition of a Prism Pair Compressor to the Gate Pulse

Group Velocity Dispersion (GVD) dictates that in all normal (termed +GVD) materials the index of refraction, and hence the speed of light, is not identical for all wavelengths.[98] The shorter, higher-energy wavelengths move slower through the +GVD medium which results in a temporally broadened pulse of light. This variation of phase with respect to wavelength is known as a chirped pulse. To correct this positive GVD, a prism pair compressor can be used to induce a negative GVD to the pulse to counter the positive GVD and recompress all wavelengths to the same point in time. While longer wavelengths travel faster in a normal (+GVD) medium, they are also refracted less. By introducing a second prism, the longer wavelengths are forced to travel through more prism material which allows the shorter wavelengths to "catch up". Optimizing the amount of prism the beam traverses will yield a pulse with a net zero GVD, *i.e.* the wavelengths within the pulse will be temporally re-compressed.

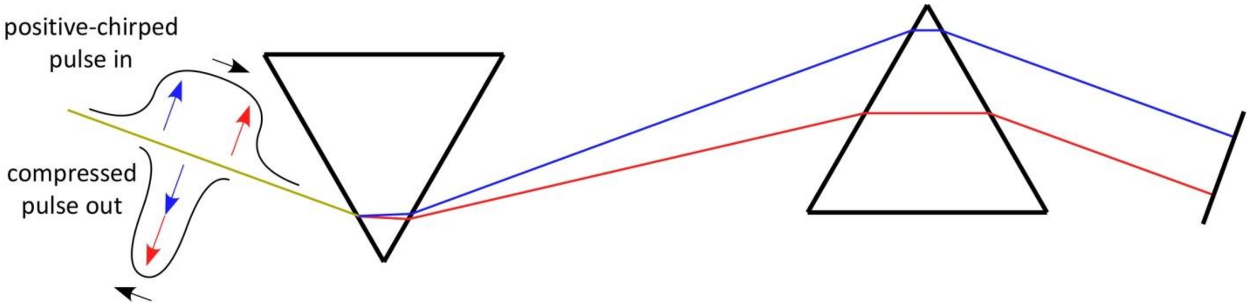

Figure B.1. Schematic of a prism pair compressor.

A Frequency Resolved Optical Grating[99] (FROG) was used to monitor the pulse width after the recompression optics in the RegA, and the pulse width was minimized to <250 fs FWHM. However, when the RegA pulse was minimized temporally, the gate pulse from the OPA was too long (>300 fs) to enable an adequate instrument response function in the upconversion experiment (needs to be <250 fs). This was due to the thick dichroic that was used to extract the gate beam from the OPA causing the pulse to become chirped. Therefore, a prism pair was added to the gate beam path in order to induce an equal but opposite negative GVD to recompress the gate pulse. The distance the prism pair compressor added to the beam path (~22.5 cm one-way) was compensated for by removing the same amount of path length from the gate beam slider in order to maintain both excitation and probe pulses arriving at the nonlinear upconversion crystal at the same time for $t = 0$. The prisms were mounted on a rotational stage for fine-tuning of the angles and allow for tabulation of the optimal settings for pulse recompression. After incorporation of the prism pair compressor, the gate pulse was routinely <220 fs FWHM and instrument response functions of <250 fs FWHM were readily attainable.

B.2 Sample Considerations: Conversion from a Custom Flow Cell to a Commercial Cuvette

Of great concern when studying the ensemble photo-physics of semiconductor nanocrystals, or of fluorescent colloidal suspensions in general, is the potential of altering the sample being investigated by the excitation beam. These potential effects include modifications to the sample such as photo-charging, photo-oxidation, or any other means of physically altering the sample itself during the course of the data collection due to the energy of the excitation source and/or the conditions under which the sample is kept during collection of the data. There is also the potential for sample build-up on the walls of the apparatus that contains the sample during data collection. Thus, there is a need to continually refresh the sample being probed during and in between the temporal scans of data acquisition. The ways in which this can be accomplished are very much dependent on the experimental setup and include (but by no means are limited to) raster scanning the sample, circulating the sample through a flow cell, and/or stirring the sample in a cuvette.

Previous studies with the laser system described in section 2.4.2 accomplished the required refreshing of the sample during data collection procedures by circulating the sample through a custom-built flow cell apparatus. The sample was loaded into a reservoir that was plumbed through an electric pump and connected to the custom flow cell using swage-lock fittings. The many years of use dictated many cycles of cleaning the flow cell which was accomplished by rinsing and/or disassembly and soaking in (separately) piranha and hydrofluoric acid, respectively. These many cleaning cycles eventually compromised the optical integrity of the 2 mm path length quartz portion of the flow cell in which the sample was exposed to the excitation beam and from which the sample fluorescence was collected. The degraded optical polishing of the flow cell induced substantial scattering of the pump beam by the flow cell which led to an exaggerated instrument artifact in negative time as is described in section 2.4.3. During the initial attempts to collect fluorescence upconversion data, the instrument artifact was so large that it overwhelmed the fluorescence from the sample. Attempts to attenuate the artifact in the data would, ultimately, completely block the sample fluorescence and prevent acquisition of upconverted fluorescence signal from the nanocrystal samples. This generated a need to replace the flow cell with either another custom-fabricated flow cell or with something else that would meet the needs of the experiment.

There were sufficient downsides to simple replacement of the flow cell with another custom-fabricated flow cell that were taken into consideration and ultimately required a different route to rectify the pump scatter. First, the fact that the flow cell was a custom-fabricated unit meant that individual parts had to be acquired from scratch and then acceptably assembled to be (almost) perfectly optically transparent. Initial attempts towards this end resulted in a flow cell that contained defects and ultimately induced even more pump scatter than the original, or else was too fragile to maintain structural integrity under experimental conditions. Furthermore, the amount of sample required to fill the reservoir, pump head, plumbing, and quartz flow cell was ~20 mL. On top of that, the sample was required to be at sufficient optical density at excitation wavelength. This often required an entire batch of nanocrystals from a single synthesis to be purified and very lightly diluted to ensure proper sample preparation. These large and intensive sample requirements for the flow cell apparatus were prohibitive in that they generated a lot of chemical and solvent waste and since entire samples were necessary, time-points from a single synthesis could not be analyzed. This meant that different syntheses of samples would be required to be quenched at the different time points and the entire sample purified to analyze structural evolution of any given nanocrystal structure.

For these reasons, an alternative solution was pursued that would alleviate the prohibitive sample requirements and would enable a commercially available alternative for future repair or replacement. A quartz cuvette was ordered from Starna Cells (Cat. No. 1-Q-2) that maintained the current 2 mm path length and had a nominal sample volume of 0.7 mL. Also acquired were 1.5 x 8 mm micro stir bars from Fisher Scientific (Cat. No. 14-513-64) that fit in the cuvette while still allowing ample room for movement and stirring. Stirring was accomplished by mounting an electric micro-stirrer repurposed from a PTI QuantaMaster 40 Spectrofluorometer to enable it to be retractable and its position adjustable to allow for smooth yet vigorous stirring of the colloidal samples in the cuvette. A custom mounting bracket was fabricated by the physics machine shop at Vanderbilt University that was attached to the previously employed xyz micrometer stage to allow for the sample to be translated in the x and y direction for initial alignment and in the z direction between scans to prevent scatter from sample build-up on the wall of the cuvette over many scans during the course of data collection. This new cuvette not only replaced the flow cell with a commercially available component that was sufficiently optically transparent to prevent pump scatter and was stir-able to continually refresh the sample, but it improved upon it by decreasing the necessary sample volume from ~20 mL with the flow cell down to less than 1 mL which allowed for analysis of the structural evolution of a single sample architecture from the same, single synthesis.

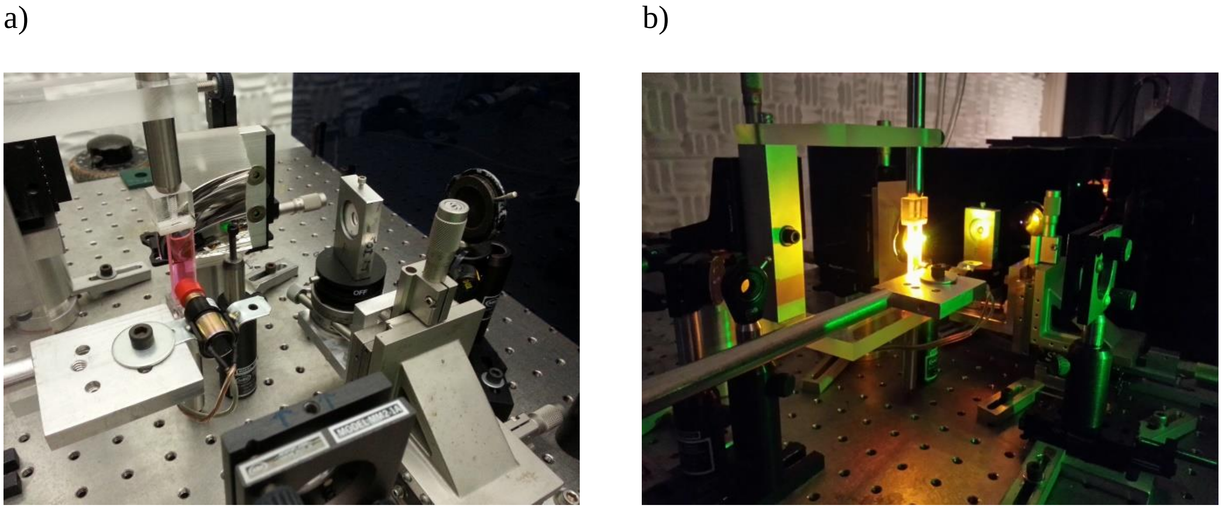

Figure B.2. Pictures of the new cuvette in the fluorescence upconversion experimental setup. Left is a picture under room lighting with Sulforhodamine B in ethanol loaded in the cuvette while stirring and right is the same sample under illumination by the excitation beam.

REFERENCES

1 Brus, L. E. Electron-Electron and Electron-Hole Interactions in Small Semiconductor Crystallites: The Size Dependence of the Lowest Excited Electronic State. *Journal of Chemical Physics* **80**, 4403-4409, doi:10.1063/1.447218 (1984).

2 Scholes, G. D. & Rumbles, G. Excitons in Nanoscale Systems. *Nature Materials* **5**, 683-696, doi:10.1038/nmat1710 (2006).

3 Efros, A. L. *et al.* Band-Edge Exciton in Quantum Dots of Semiconductors with a Degenerate Valence Band: Dark and Bright Exciton States. *Physical Review B* **54**, 4843-4856, doi:10.1103/PhysRevB.54.4843 (1996).

4 Rosenthal, S. J., McBride, J., Pennycook, S. J. & Feldman, L. C. Synthesis, Surface Studies, Composition and Structural Characterization of CdSe, Core/Shell and Biologically Active Nanocrystals. *Surface Science Reports* **62**, 111-157, doi:10.1016/j.surfrep.2007.02.001 (2007).

5 Bowers, M. J., McBride, J. R. & Rosenthal, S. J. White-Light Emission from Magic-sized Cadmium Selenide Nanocrystals. *Journal of the American Chemical Society* **127**, 15378-15379, doi:10.1021/ja055470d (2005).

6 Bowers, M. J. *et al.* Structure and Ultrafast Dynamics of White-Light-Emitting CdSe Nanocrystals. *Journal of the American Chemical Society* **131**, 5730-5731, doi:10.1021/ja900529h (2009).

7 Dukes, A. D., III *et al.* Single-Nanocrystal Spectroscopy of White-Light-Emitting CdSe Nanocrystals. *Journal of Physical Chemistry A* **115**, 4076-4081, doi:10.1021/jp1109509 (2011).

8 Garrett, M. D. *et al.* Band Edge Dynamics in CdSe Nanocrystals Observed by Ultrafast Fluorescence Upconversion. *Journal of Physical Chemistry C* **112**, 436-442, doi:10.1021/jp7099306 (2008).

9 Garrett, M. D. *et al.* Band Edge Recombination in CdSe, CdS and CdS_xSe_{1-x} Alloy Nanocrystals Observed by Ultrafast Fluorescence Upconversion: The Effect of Surface Trap States. *Journal of Physical Chemistry C* **112**, 12736-12746, doi:10.1021/jp803708r (2008).

10 Kippeny, T. C. *et al.* Effects of Surface Passivation on the Exciton Dynamics of CdSe Nanocrystals as Observed by Ultrafast Fluorescence Upconversion Spectroscopy. *Journal of Chemical Physics* **128**, 084713, doi:10.1063/1.2834692 (2008).

11 Underwood, D. F., Kippeny, T. & Rosenthal, S. J. Ultrafast Carrier Dynamics in CdSe Nanocrystals Determined by Femtosecond Fluorescence Upconversion Spectroscopy. *Journal of Physical Chemistry B* **105**, 436-443, doi:10.1021/jp003088b (2001).

12 Pennycook, T. J., McBride, J. R., Rosenthal, S. J., Pennycook, S. J. & Pantelides, S. T. Dynamic Fluctuations in Ultrasmall Nanocrystals Induce White Light Emission. *Nano Letters* **12**, 3038-3042, doi:10.1021/nl3008727 (2012).

13 McBride, J. R., Pennycook, T. J., Pennycook, S. J. & Rosenthal, S. J. The Possibility and Implications of Dynamic Nanoparticle Surfaces. *ACS Nano* **7**, 8358-8365, doi:10.1021/nn403478h (2013).

14 Burda, C. & El-Sayed, M. A. High-Density Femtosecond Transient Absorption Spectroscopy of Semiconductor Nanoparticles. A Tool to Investigate Surface Quality. *Pure and Applied Chemistry* **72**, 165-177, doi:10.1351/pac200072010165 (2000).

15 Klimov, V. I., McBranch, D. W., Leatherdale, C. A. & Bawendi, M. G. Electron and Hole Relaxation Pathways in Semiconductor Quantum Dots. *Physical Review B* **60**, 13740-13749, doi:10.1103/PhysRevB.60.13740 (1999).

16 Guyot-Sionnest, P., Wehrenberg, B. & Yu, D. Intraband Relaxation in CdSe Nanocrystals and the Strong Influence of the Surface Ligands. *Journal of Chemical Physics* **123**, 074709, doi:10.1063/1.2004818 (2005).

17 Logunov, S., Green, T., Marguet, S. & El-Sayed, M. A. Interfacial Carriers Dynamics of CdS Nanoparticles. *Journal of Physical Chemistry A* **102**, 5652-5658, doi:10.1021/jp980387g (1998).

18 Taylor, J., Kippeny, T. & Rosenthal, S. J. Surface Stoichiometry of CdSe Nanocrystals Determined by Rutherford Backscattering Spectroscopy. *Journal of Cluster Science* **12**, 571-582, doi:10.1023/A:1014246315331 (2001).

19 Pokrant, S. & Whaley, K. B. Tight-binding Studies of Surface Effects on Electronic Structure of CdSe Nanocrystals: The Role of Organic Ligands, Surface Reconstruction, and Inorganic Capping Shells. *European Physical Journal D* **6**, 255-267, doi:10.1007/s100530050307 (1999).

20 Leung, K. & Whaley, K. B. Surface Relaxation in CdSe Nanocrystals. *Journal of Chemical Physics* **110**, 11012-11022, doi:10.1063/1.479037 (1999).

21 Kuno, M., Lee, J. K., Dabbousi, B. O., Mikulec, F. V. & Bawendi, M. G. The Band Edge Luminescence of Surface Modified CdSe Nanocrystallites: Probing the Luminescing State. *Journal of Chemical Physics* **106**, 9869-9882, doi:10.1063/1.473875 (1997).

22 Nirmal, M. *et al.* Observation of the Dark Exciton in CdSe Quantum Dots. *Physical Review Letters* **75**, 3728-3731, doi:10.1103/PhysRevLett.75.3728 (1995).

23 McBride, J. R., Kippeny, T. C., Pennycook, S. J. & Rosenthal, S. J. Aberration-Corrected Z-Contrast Scanning Transmission Electron Microscopy of CdSe Nanocrystals. *Nano Letters* **4**, 1279-1283, doi:10.1021/nl04906q (2004).

24 Knowles, K. E., McArthur, E. A. & Weiss, E. A. A Multi-Timescale Map of Radiative and Nonradiative Decay Pathways for Excitons in CdSe Quantum Dots. *ACS Nano* **5**, 2026–2035, doi:10.1021/nn2002689 (2011).

25 Jones, M., Lo, S. S. & Scholes, G. D. Signatures of Exciton Dynamics and Carrier Trapping in the Time-Resolved Photoluminescence of Colloidal CdSe Nanocrystals. *Journal of Physical Chemistry C* **113**, 18632-18642, doi:10.1021/jp9078772 (2009).

26 Jones, M., Lo, S. S. & Scholes, G. D. Quantitative Modeling of the Role of Surface Traps in CdSe/CdS/ZnS Nanocrystal Photoluminescence Decay Dynamics. *Proceedings of the National Academy of Sciences of the United States of America* **106**, 3011-3016, doi:10.1073/pnas.0809316106 (2009).

27 Kern, S. J., Sahu, K. & Berg, M. A. Heterogeneity of the Electron-Trapping Kinetics in CdSe Nanoparticles. *Nano Letters* **11**, 3493-3498, doi:10.1021/nl202086b (2011).

28 Califano, M. & Gomez-Campos, F. M. Universal Trapping Mechanism in Semiconductor Nanocrystals. *Nano Letters* **13**, 2047-2052, doi:10.1021/nl4003014 (2013).

29 Zhu, H. *et al.* Auger-Assisted Electron Transfer from Photoexcited Semiconductor Quantum Dots. *Nano Letters* **14**, 1263-1269, doi:10.1021/nl4041687 (2014).

30 Gadd, S. E. *Excited State Carrier Dynamics in* CdS_xSe_{1-x} *Semiconductor Alloys as Studies by Ultrafast Fluorescence Spectroscopy*, University of California, (1995).

31 Hane, J. K. *et al.* Time-Resolved Luminescence of Electron-Hole Pairs in CdS_xSe_{1-x} Graded Semiconductors. *Journal of Physical Chemistry* **93**, 7975-7977, doi:10.1021/j100361a004 (1989).

32 Hane, J. K. *The Picosecond Dynamics of Electron-Hole Pairs in Graded and Homogeneous CdS_xSe_{1-x} Semiconductors*, (1995).

33 Zhang, F. J., Zhang, L. M. & Claus, R. O. Nonlinear Differential Ultrafast Laser Absorption Spectroscopy Observation of Charge Carrier Dynamics of CdS_xSe_{1-x} Nanocrystal Doped Glasses. *Smart Materials & Structures* **16**, 243-248, doi:10.1088/0964-1726/16/2/002 (2007).

34 Zhang, X. J. & Izutsu, M. Ultrafast Processes of Highly Excited Carriers in CdS_xSe_{1-x}-Doped Glass. *Japanese Journal of Applied Physics* **37**, 6025-6028, doi:10.1143/jjap.37.6025 (1998).

35 Shen, Q. *et al.* Ultrafast Dynamics of CdS_xSe_{1-x} Nanocrystals Doped in Glasses Studied by Ultrafast Transient Lensing Effect. *Analytical Sciences* **17**, S241-S244 (2001).

36 Toyoda, T. & Shen, Q. Effect of Size Confinement on Photoacoustic Spectra and Photothermal Response of CdS_xSe_{1-x} (0 <= x <= 1) Nanocrystals in a Glass Matrix. *Analytical Sciences* **17**, S259-S261 (2001).

37 Li, J. J. *et al.* Large-scale Synthesis of Nearly Monodisperse CdSe/CdS Core/Shell Nanocrystals Using Air-stable Reagents via Successive Ion Layer Adsorption and Reaction. *Journal of the American Chemical Society* **125**, 12567-12575, doi:10.1021/ja0363563 (2003).

38 Gupta, S., Kershaw, S. V. & Rogach, A. L. 25th Anniversary Article: Ion Exchange in Colloidal Nanocrystals. *Advanced Materials* **25**, 6923-6943, doi:10.1002/adma.201302400 (2013).

39 Harrison, M. A., Ng, A., Hmelo, A. B. & Rosenthal, S. J. CdSSe Nanocrystals with Induced Chemical Composition Gradients. *Israel Journal of Chemistry* **52**, 1063-1072, doi:10.1002/ijch.201200040 (2012).

40 Swafford, L. A. *et al.* Homogeneously Alloyed CdS_xSe_{1-x} Nanocrystals: Synthesis, Characterization, and Composition/Size-Dependent Band Gap. *Journal of the American Chemical Society* **128**, doi:10.1021/ja063939e (2006).

41 Lokteva, I. *et al.* Surface Treatment of CdSe Nanoparticles for Application in Hybrid Solar Cells: The Effect of Multiple Ligand Exchange with Pyridine. *Journal of Physical Chemistry C* **114**, doi:10.1021/jp103300v (2010).

42 Yu, W. W., Qu, L. H., Guo, W. Z. & Peng, X. G. Experimental Determination of the Extinction Coefficient of CdTe, CdSe, and CdS Nanocrystals. *Chemistry of Materials* **15**, 2854-2860, doi:10.1021/cm034081k (2003).

43 Allen, M. W. Measurement of Fluorescence Quantum Yields. (Thermo Fisher Scientific, Madison, WI, USA, 2010).

44 Jones, G. & Rahman, M. A. Fluorescence Properties of Coumarin Laser-Dyes in Aqueous Polymer Media - Chromophore Isolation in Poly(methacrylic acid) Hypercoils. *Journal of Physical Chemistry* **98**, 13028-13037, doi:10.1021/j100100a035 (1994).

45 Baumler, W. & Penzkofer, A. Fluorescence Spectroscopic Analysis of N and P Isomers of DODCI. *Chemical Physics* **140**, 75-97, doi:10.1016/0301-0104(90)89051-q (1990).

46 Beaumont, P. C., Johnson, D. G. & Parsons, B. J. Laser Flash Photolysis Studies of Some Rhodamine Dyes - Characterisation of the Lowest Excited Singlet State of Rhodamine 3B, Sulforhodamine B and Sulforhodamine 101. *Journal of the Chemical Society-Faraday Transactions* **94**, 195-199, doi:10.1039/a705692c (1998).

47 Fleming, G. R. *Chemical Applications of Ultrafast Spectroscopy*. (Oxford University Press, 1986).

48 Kahlow, M. A., Jarzeba, W., Dubruil, T. P. & Barbara, P. F. Ultrafast Emission-Spectroscopy in the Ultraviolet by Time-Gated Upconversion. *Review of Scientific Instruments* **59**, 1098-1109 (1988).

49 Keene, J. D., McBride, J. R., Orfield, N. J. & Rosenthal, S. J. Elimination of Hole-Surface Overlap in Graded CdS_xSe_{1-x} Nanocrystals Revealed by Ultrafast Fluorescence Upconversion Spectroscopy. *ACS Nano* **8**, 10665-10673, doi:10.1021/nn504235w (2014).

50 Bhasikuttan, A. C., Suzuki, M., Nakashima, S. & Okada, T. Ultrafast Fluorescence Detection in Tris(2,2 '-bipyridine)ruthenium(II) Complex in Solution: Relaxation Dynamics Involving Higher Excited States. *Journal of the American Chemical Society* **124**, 8398-8405, doi:10.1021/ja026135h (2002).

51 Underwood, D. F., Kippeny, T. & Rosenthal, S. J. Charge Carrier Dynamics in CdSe Nanocrystals: Implications for the Use of Quantum Dots in Novel Photovoltaics. *European Physical Journal D* **16**, 241-244, doi:10.1007/s100530170101 (2001).

52 Rosenthal, S. J. *et al.* Targeting Cell Surface Receptors with Ligand-Conjugated Nanocrystals. *Journal of the American Chemical Society* **124**, doi:10.1021/ja003486s (2002).

53 Schreuder, M. A. *et al.* Encapsulated White-Light CdSe Nanocrystals as Nanophosphors for Solid-State Lighting. *Journal of Materials Chemistry* **18**, 970-975, doi:10.1039/b716803a (2008).

54 Chuang, C.-H., Lo, S. S., Scholes, G. D. & Burda, C. Charge Separation and Recombination in CdTe/CdSe Core/Shell Nanocrystals as a Function of Shell Coverage: Probing the Onset of the Quasi Type-II Regime. *Journal of Physical Chemistry Letters* **1**, doi:10.1021/jz1008399 (2010).

55 Lo, S. S., Mirkovic, T., Chuang, C.-H., Burda, C. & Scholes, G. D. Emergent Properties Resulting from Type-II Band Alignment in Semiconductor Nanoheterostructures. *Advanced Materials* **23**, doi:10.1002/adma.201002290 (2011).

56 Huynh, W. U., Dittmer, J. J. & Alivisatos, A. P. Hybrid Nanorod-Polymer Solar Cells. *Science* **295**, 2425-2427, doi:10.1126/science.1069156 (2002).

57 Grancini, G. *et al.* Dynamic Microscopy Study of Ultrafast Charge Transfer in a Hybrid P3HT/Hyperbranched CdSe Nanoparticle Blend for Photovoltaics. *Journal of Physical Chemistry Letters* **3**, doi:10.1021/jz3000382 (2012).

58 Wang, C. H. *et al.* Direct Evidence of Type II Band Alignment in Nanoscale P3HT/CdSe Heterostructures. *Nanotechnology* **22**, doi:10.1088/0957-4484/22/6/065202 (2011).

59 Milliron, D. J., Alivisatos, A. P., Pitois, C., Edder, C. & Frechet, J. M. J. Electroactive Surfactant Designed to Mediate Electron Transfer Between CdSe Nanocrystals and Organic Semiconductors. *Advanced Materials* **15**, 58-61, doi:10.1002/adma.200390011 (2003).

60 Stalder, R. *et al.* Variable-Gap Conjugated Oligomers Grafted to CdSe Nanocrystals. *Chemistry of Materials* **24**, 3143-3152, doi:10.1021/cm301351j (2012).

61 Kochemba, W. M., Pickel, D. L., Sumpter, B. G., Chen, J. & Kilbey, S. M., II. In Situ Formation of Pyridyl-Functionalized Poly(3-hexylthiophene)s via Quenching of the Grignard Metathesis Polymerization: Toward Ligands for Semiconductor Quantum Dots. *Chemistry of Materials* **24**, 4459-4467, doi:10.1021/cm302915h (2012).

62 Kochemba, W. M. *et al.* Correction to In Situ Formation of Pyridyl-Functionalized Poly(3-hexylthiophene)s via Quenching of the Grignard Metathesis Polymerization: Toward Ligands for Semiconductor Quantum Dots. *Chemistry of Materials* **25**, 113-113, doi:10.1021/cm303907t (2013).

63 Morris-Cohen, A. J., Malicki, M., Peterson, M. D., Slavin, J. W. J. & Weiss, E. A. Chemical, Structural, and Quantitative Analysis of the Ligand Shells of Colloidal Quantum Dots. *Chemistry of Materials* **25**, 1155-1165, doi:10.1021/cm302108j (2013).

64 Dubois, F., Mahler, B., Dubertret, B., Doris, E. & Mioskowski, C. A Versatile Strategy for Quantum Dot Ligand Exchange. *Journal of the American Chemical Society* **129**, 482-483, doi:10.1021/ja067742y (2007).

65 Panthani, M. G. *et al.* Synthesis of $CuInS_2$, $CuInSe_2$, and $Cu(In_xGa_{1-x})Se_2$ (CIGS) Nanocrystal "Inks" for Printable Photovoltaics. *Journal of the American Chemical Society* **130**, 16770-16777, doi:10.1021/ja805845q (2008).

66 Li, L. *et al.* Efficient Synthesis of Highly Luminescent Copper Indium Sulfide-Based Core/Shell Nanocrystals with Surprisingly Long-Lived Emission. *Journal of the American Chemical Society* **133**, doi:10.1021/ja108261h (2011).

67 Turo, M. J. & Macdonald, J. E. Crystal-Bound vs Surface-Bound Thiols on Nano Crystals. *ACS Nano* **8**, 10205-10213, doi:10.1021/nn5032164 (2014).

68 Liu, I. S. *et al.* Enhancing Photoluminescence Quenching and Photoelectric Properties of CdSe Quantum Dots with Hole Accepting Ligands. *Journal of Materials Chemistry* **18**, 675-682, doi:10.1039/b715253a (2008).

69 Niezgoda, J. S., Harrison, M. A., McBride, J. R. & Rosenthal, S. J. Novel Synthesis of Chalcopyrite $Cu_xIn_yS_2$ Quantum Dots with Tunable Localized Surface Plasmon Resonances. *Chemistry of Materials* **24**, 3294-3298, doi:10.1021/cm3021462 (2012).

70 Drago, R. S. *Physical Methods for Chemists*. 2 edn, (Saunders College Publishing, 1992).

71 Niezgoda, J. S., Yap, E., Keene, J. D., McBride, J. R. & Rosenthal, S. J. Plasmonic $Cu_xIn_yS_2$ Quantum Dots Make Better Photovoltaics Than Their Nonplasmonic Counterparts. *Nano Letters* **14**, 3262-3269, doi:10.1021/nl500645k (2014).

72 Schreuder, M. A., Xiao, K., Ivanov, I. N., Weiss, S. M. & Rosenthal, S. J. White Light-Emitting Diodes Based on Ultrasmall CdSe Nanocrystal Electroluminescence. *Nano Letters* **10**, 573-576, doi:10.1021/nl903615g (2010).

73 Klimov, V. I. *et al.* Optical Gain and Stimulated Emission in Nanocrystal Quantum Dots. *Science* **290**, 314-317, doi:10.1126/science.290.5490.314 (2000).

74 Bruchez, M., Moronne, M., Gin, P., Weiss, S. & Alivisatos, A. P. Semiconductor Nanocrystals as Fluorescent Biological Labels. *Science* **281**, 2013-2016, doi:10.1126/science.281.5385.2013 (1998).

75 Rosenthal, S. J., Chang, J. C., Kovtun, O., McBride, J. R. & Tomlinson, I. D. Biocompatible Quantum Dots for Biological Applications. *Chemistry & Biology (Cambridge, MA, United States)* **18**, 10-24, doi:10.1016/j.chembiol.2010.11.013 (2011).

76 Kim, S., Fisher, B., Eisler, H. J. & Bawendi, M. Type-II Quantum Dots: CdTe/CdSe(Core/Shell) and CdSe/ZinTe(Core/Shell) Heterostructures. *Journal of the American Chemical Society* **125**, 11466-11467, doi:10.1021/ja0361749 (2003).

77 McBride, J., Treadway, J., Feldman, L. C., Pennycook, S. J. & Rosenthal, S. J. Structural Basis for Near Unity Quantum Yield Core/Shell Nanostructures. *Nano Letters* **6**, 1496-1501, doi:10.1021/nl060993k (2006).

78 Chen, Y. *et al.* "Giant" Multishell CdSe Nanocrystal Quantum Dots with Suppressed Blinking. *Journal of the American Chemical Society* **130**, 5026-5027, doi:10.1021/ja711379k (2008).

79 Dabbousi, B. O. *et al.* (CdSe)ZnS Core-Shell Quantum Dots: Synthesis and Characterization of a Size Series of Highly Luminescent Nanocrystallites. *Journal of Physical Chemistry B* **101**, 9463-9475, doi:10.1021/jp971091y (1997).

80 Garcia-Santamaria, F. *et al.* Breakdown of Volume Scaling in Auger Recombination in CdSe/CdS Heteronanocrystals: The Role of the Core-Shell Interface. *Nano Letters* **11**, 687-693, doi:10.1021/nl103801e (2011).

81 Garcia-Santamaria, F. *et al.* Suppressed Auger Recombination in "Giant" Nanocrystals Boosts Optical Gain Performance. *Nano Letters* **9**, 3482-3488, doi:10.1021/nl901681d (2009).

82 Wang, X. Y. *et al.* Non-blinking Semiconductor Nanocrystals. *Nature* **459**, 686-689, doi:10.1038/nature08072 (2009).

83 Park, Y.-S., Bae, W. K., Padilha, L. A., Pietryga, J. M. & Klimov, V. I. Effect of the Core/Shell Interface on Auger Recombination Evaluated by Single-Quantum-Dot Spectroscopy. *Nano Letters* **14**, 396-402, doi:10.1021/nl403289w (2014).

84 Cragg, G. E. & Efros, A. L. Suppression of Auger Processes in Confined Structures. *Nano Letters* **10**, 313-317, doi:10.1021/nl903592h (2010).

85 McArthur, E. A., Morris-Cohen, A. J., Knowles, K. E. & Weiss, E. A. Charge Carrier Resolved Relaxation of the First Excitonic State in CdSe Quantum Dots Probed with Near-Infrared Transient Absorption Spectroscopy. *Journal of Physical Chemistry B* **114**, 14514-14520, doi:10.1021/jp102101f (2010).

86 Klimov, V., Bolivar, P. H. & Kurz, H. Ultrafast Carrier Dynamics in Semiconductor Quantum Dots. *Physical Review B* **53**, 1463-1467, doi:10.1103/PhysRevB.53.1463 (1996).

87 Pandey, A. & Guyot-Sionnest, P. Intraband Spectroscopy and Band Offsets of Colloidal II-VI Core/Shell Structures. *Journal of Chemical Physics* **127**, 104710, doi:10.1063/1.2766957 (2007).

88 McKelvey, J. P. *Solid State and Semiconductor Physics*. 312 (Harper and Row, 1966).

89 Ray, B. *II-VI Compounds*. 1st edn, Vol. 2 83 (Pergamon Press, 1969).

90 Rosenthal, S. J., Jimenez, R., Fleming, G. R., Kumar, P. V. & Maroncelli, M. Solvation Dynamics in Methanol: Experimental and Molecular Dynamics Simulation Studies. *Journal of Molecular Liquids* **60**, 25-56, doi:10.1016/0167-7322(94)00738-1 (1994).

91 Rosenthal, S. J., Xie, X., Du, M. & Fleming, G. R. Femtosecond Solvation Dynamics in Acetonitrile: Observation of the Inertial Contribution to the Solvent Response. *Journal of Chemical Physics* **95**, 4715-4718, doi:10.1063/1.461742 (1991).

92 Ekimov, A. I. *et al.* Absorption and Intensity-Dependent Photoluminescence Measurements on CdSe Quantum Dots - Assignment of the 1st Electronic Transitions. *Journal of the Optical Society of America B-Optical Physics* **10**, 100-107 (1993).

93 Klimov, V. I. Spectral and Dynamical Properties of Multiexcitons in Semiconductor Nanocrystals. *Annual Review of Physical Chemistry* **58**, 635-673, doi:10.1146/annurev.physchem.58.032806.104537 (2007).

94 Kambhampati, P. Hot Exciton Relaxation Dynamics in Semiconductor Quantum Dots: Radiationless Transitions on the Nanoscale. *Journal of Physical Chemistry C* **115**, 22089-22109, doi:10.1021/jp2058673 (2011).

95 Rempel, J. Y., Trout, B. L., Bawendi, M. G. & Jensen, K. F. Density Functional Theory Study of Ligand Binding on CdSe (0001), (000(1)over-bar), and (11(2)over-bar-0) Single Crystal Relaxed and Reconstructed Surfaces: Implications for Nanocrystalline Growth. *Journal of Physical Chemistry B* **110**, doi:10.1021/jp064051f (2006).

96 Chen, O. *et al.* Compact High-Quality CdSe-CdS Core-Shell Nanocrystals with Narrow Emission Linewidths and Suppressed Blinking. *Nature Materials* **12**, 445-451, doi:10.1038/nmat3539 (2013).

97 Hintz, H. *et al.* Photodegradation of P3HT-A Systematic Study of Environmental Factors. *Chemistry of Materials* **23**, doi:10.1021/cm102373k (2011).

98 *Operator's Manual: The Coherent Mira Model 900-B Laser*. (Coherent Laser Group).

99 Kane, D. J. & Trebino, R. Characterization of Arbitrary Femtosecond Pulses Using Frequency-Resolved Optical Gating. *IEEE Journal of Quantum Electronics* **29**, 571-579, doi:10.1109/3.199311 (1993).